

Applications of Surface Vibrational Spectroscopic Techniques

E.C. Hargreaves

**A thesis submitted to the University of Nottingham in partial fulfilment of
the requirements for the degree of Doctor of Philosophy**

December 1997

**© This copy of the thesis has been supplied on condition that anyone who
consults it is understood to recognise that its copyright rests with the
author and that no quotation from the thesis, nor any information derived
therefrom, may be published without the author's prior written consent.**

Declaration

I declare that the work contained in this thesis, submitted by me for the degree of Doctor of Philosophy, is my own work, except where due reference is made to other authors, and has not been previously submitted by me for a degree at this or any other university.

‘Still round the corner there may wait
A new road or a secret gate;
And though I oft have passed them by,
A day will come at last when I
Shall take the hidden paths that run
West of the Moon, East of the Sun.’

‘The Road goes ever on and on
Out from the door where it began.
Now far ahead the road has gone,
Let others follow it who can!
Let them a journey new begin,
But I at last with weary feet
Will turn towards the lighted inn,
My evening-rest and sleep to meet.’

J.R.R. Tolkien
‘The Lord of the Rings’

Acknowledgements

I have been lucky to meet a great diversity of people throughout my PhD, all of whom have contributed in one form or another.

First, I would like to thank my supervisor Mike Chesters, whose head is always bulging full of ideas. Thanks also for your patience, practical skill and persistence. I certainly now know the meaning of the word 'challenging'. Thanks too for the many trips abroad. Thanks to Martin McCoustra for filling in here and there.

Cheers to Johnny 'Blah blah blah' Wenger, Darren 'Baa baa baa' Oakes and Dave Slater, the 'UEA' contingent. For valuable assistance Pete Parlett, and the rest of the research group for sorting out computer problems and general discussion, Stu Coomber, Frank Rutten and Kat Street.

The man with the original lucky white trousers, Peter Hollins-
Cheers for the pints!

Helen Turner, for the last seven years, Anne-Marie, for the hot meals, the girls from the hockey club, Stan, for the room, Mike's secretaries 'Is he in ?'- Margaret and Ruth, Quesne for the computer, Sarah 'Etch-a-Sketch' Bastow and Dave Townsend for the proof reading.

The man with the muscle, Neil Barnes. Neil, I am greatly indebted for all your hard work and ingenuity. Martin Dellar and the boys from the workshop, the glass blowers and Ralph and Dave for the electronic wizardry.

Thanks to Barbara Ruzicka and Anna-Rosa for their patience and for trying to understand the English sense of humour.

Last but not least there are two people who deserve a special mention.

Martin Pearson, thanks for the Daresbury run-I was sent to stop you from cracking up but it only took me two hours! We has some good times in the sunshine and the all-nighter! Thanks for the decent conversation-not including Leeds United F.C., all the help in the final stages of this thesis, analysis and diagrams, it certainly was appreciated.

Mark Ainsworth, thanks for everything, it all counts. You made me laugh when I probably shouldn't have! Thanks for the use of the beam machine and the time and effort you afforded me and the cinema trips!

Contents

Abstract

Chapter 1

Introduction

1.1 To Boldly Go	2
1.2 The Rôle of Surface Science	3
1.3 An Introduction to Surface Spectroscopic Techniques	4
1.4 Thesis Outline	6
1.5 References	8

Chapter 2

Experimental Techniques :

Principles and Instrumentation

2.1 Introduction	10
Part A Electron Energy Loss Spectroscopy (EELS)	
2.2 Experimental Details	11
2.2.1 Chamber	11
2.2.2 Pumps	12
2.2.3 Bake-out	12

2.2.4 Pressure Measurement	12
2.2.5 Gas Handling and Dosing	13
2.2.6 Sample Mounting, Manipulation and Temperature Control	14
2.2.7 Sample Cleaning	15
2.3 Principles of Electron Energy Loss Spectroscopy	15
2.3.1 Dipole Scattering	17
2.3.2 Impact Scattering	19
2.3.3 Practical Consequences	21
2.3.4 The Electron Energy Loss Spectrometer	21
Part B (I) Mid-Infrared Apparatus	
2.4 Basic FTIR Theory	24
2.4.1 The Michelson Interferometer	25
2.4.2 Resolution	28
2.4.3 Apodisation	29
2.4.4 Advantages of FTIR	30
2.5 Reflection Absorption Infrared Spectroscopy (RAIRS)	31
2.5.1 Physical Principles	31
2.6 The Ultra-high Vacuum System	35
2.6.1 Instrumentation	35
2.6.2 The Experimental Chamber	36
2.6.3 Crystal Mounting	37
2.6.4 Crystal Preparation	38

2.6.5 Gas Sample Preparation	39
2.6.6 Recording Spectra	39
Part B (ii) The Far-Infrared Apparatus	
2.7 Introduction: The Synchrotron Radiation Source	40
2.8. The Ultra-high Vacuum System	43
2.8.1 Beamline 13.3	43
2.8.2 Infrared Optics and Instrumentation	45
2.8.3 The Experimental Chamber	46
2.8.4 Sample Mounting and Preparation	47
2.9 References	48
Chapter 3	The Adsorption of
	3,3,3-trifluoropropene
	on Pt (111)
3.1 Introduction	51
3.2 Experimental	53
3.2.1 RAIRS	53
3.2.2 EELS	53
3.3 Results	
3.3.1 EELS - Clean Surface Spectra	54
3.3.2 EEL and RAIR Spectra of 3,3,3-trifluoropropene	55
3.4 Discussion	56

5.6 Conclusions

109

5.7 References

110

Abbreviations

General Abbreviations and Acronyms

IR = Infrared

FTIR = Fourier Transform Infrared

UHV = Ultra-high Vacuum

RAIRS = Reflection-Absorption Infrared Spectroscopy

EELS = Electron Energy Loss Spectroscopy

LEED = Low Energy Electron Diffraction

AES = Auger Electron Spectroscopy

NNCFC = Nearest Neighbour Central Force Constant

LAPW = Linearized Augmented Plane Wave

Vibrational Mode Abbreviations

ν = stretch

ρ = rock

δ = deformation

γ = wag

s = symmetric

as = asymmetric

Abstract

An advanced Electron Energy Loss Spectrometer has been used to study the formation of 3,3,3-trifluoropropylidyne on Pt (111). This has been compared to the results from the same system using the complementary vibrational spectroscopic technique of Reflection Absorption Infrared Spectroscopy (RAIRS). This study demonstrates the improved resolution of the new spectrometer. The thermal decomposition products, CF_3 and CF_2 have been detected in the Electron Energy Loss (EEL) spectra.

The RAIR spectra of carbon monoxide on Cu (111) have been recorded using synchrotron radiation. An optical accessory has been used to record the RAIR spectra at an incident angle of 20° . The results have been compared to an incident angle of 87° . At 20° no conventional absorption band at 339 cm^{-1} was observed and an anti-absorption band at 274 cm^{-1} of similar magnitude to that at 87° was seen. This has confirmed the involvement of the parallel electric field in the observation of anti-absorption bands.

The EEL spectra of hydrogen and deuterium adsorbed on Pt (111) at 160 K have been recorded. The data has been interpreted using the Nearest Neighbour Central Force Constant (NNCFC) model in terms of 3-fold and 2-fold bridging sites. It is the 2-fold site which offers the more complete assignment of the vibrational bands observed.

Chapter One

Introduction

1.1 To Boldly Go

1.2 The Rôle of Surface Science

**1.3 An Introduction to Surface Spectroscopic
Techniques**

1.4 Thesis Outline

1.5 References

1.1 To Boldly Go

“To boldly go where no man has gone before...”. On the 4th July 1997 the Mars mission probe, Pathfinder, successfully touched down. The first pictures transmitted back to Earth revealed a vast and varied landscape. Data transmitted from the Sojourner vehicle, roaming over the surface, has enabled scientists to discover a wealth of new information on the complexity, diversity and composition of the rock formations. After two decades of disappointment, this giant leap for mankind has been greeted ecstatically by the people who masterminded the mission. They could now “do some science” [1].

For many years, the process of gaining, examining and interpreting data on the behaviour and reactivity of surfaces has been termed ‘surface science’. In a similar manner to sending a probe to investigate another planet’s surface, scientists use spectroscopic probes such as electrons and photons to collect information about the structure and geometry of the microscopic surface environment [2].

In order to achieve this aim, a host of spectroscopic techniques have been developed specifically for the study of adsorbed species. The application of these techniques to a range of surfaces is not trivial but the resulting information obtained is valuable, especially for developing commercial catalytic processes.

Semiconductor devices represent another of the most important areas of ongoing research utilising surface science techniques [3]. The

ability to prepare ordered assemblies, for example crystalline arrays, films or layers of stable molecules on a surface, for use in integrated electronic circuits and the quality control of the production, both by surface science methods has contributed to the microcomputer revolution.

1.2 The Rôle of Surface Science

In surface science research a range of surfaces are used for specific studies. Single crystals with a small surface area (1 cm^2), thin films or polycrystalline foil are all samples that have been characterized on the atomic scale. This has been achieved by all the surface science techniques. Single crystals are prepared to expose different crystal faces and the subsequent reactions correlated with their surface structure and composition. Figure 1.1 shows a schematic diagram representing the possible adsorption sites of a small metal particle. Crystals are cut to expose a surface in which one type of surface site predominates on the atomic scale. By cutting crystals along planes of lower atomic density (high Miller index) [4], crystal faces that exhibit ordered steps and kinked structures can be prepared. Figure 1.2 shows a schematic representation of a heterogeneous surface on the atomic scale [5].

Surface Science studies on well-defined single crystal surfaces are normally carried out under conditions of Ultra-high Vacuum (UHV) involving the combined use of a number of surface-sensitive analytical techniques. Due to the rapid development of these techniques,

Figure 1.1 A Schematic Diagram Representing the Possible Adsorption Sites of a Small Metal Particle

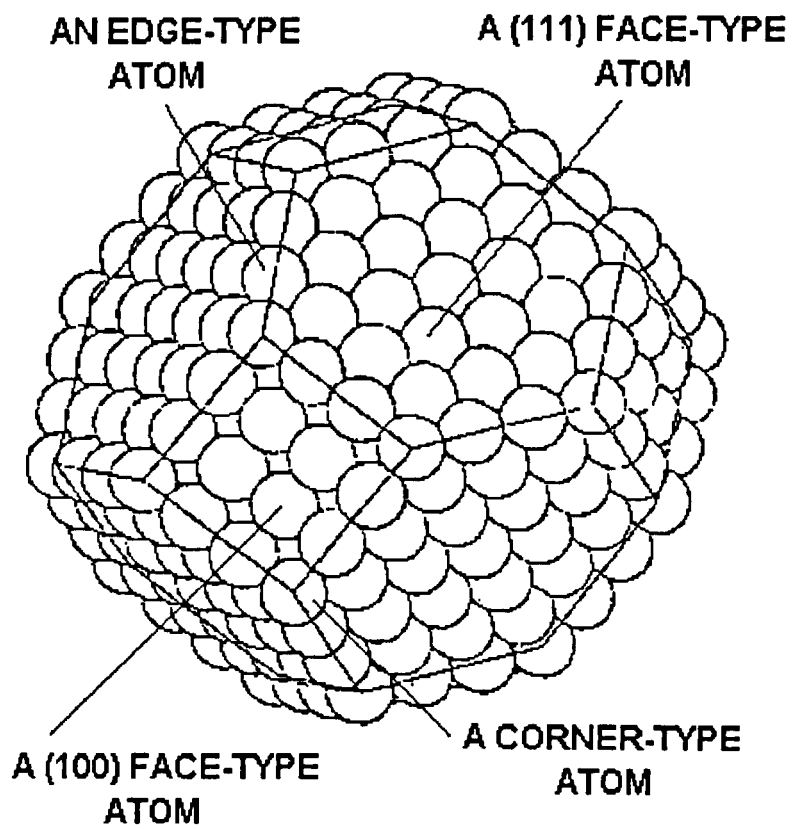
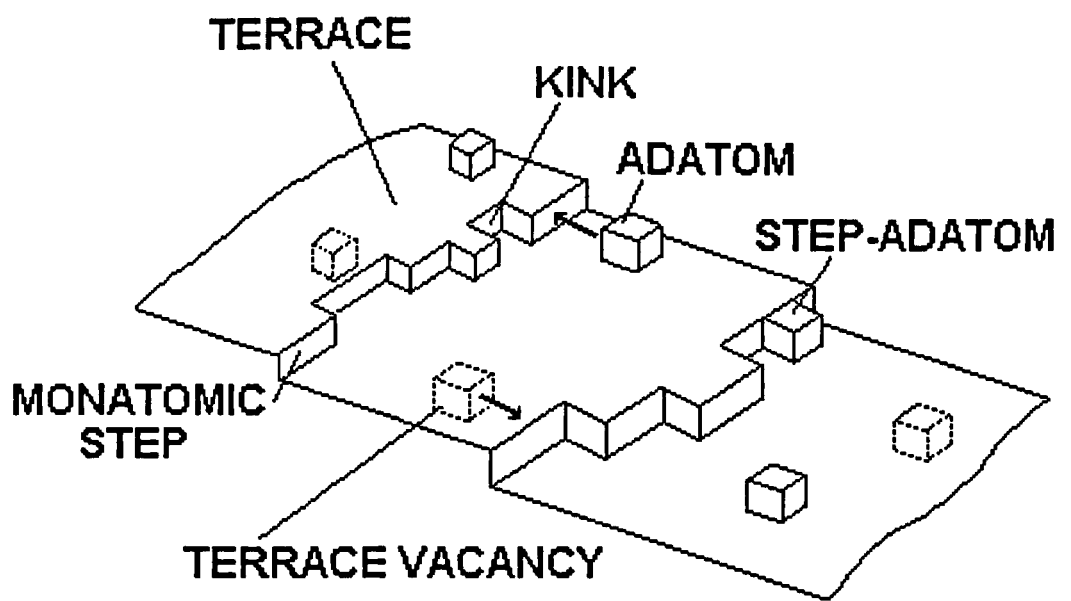


Figure 1.2 A Schematic Representation of the Heterogeneous Surface on the Atomic Scale



opportunities exist both for the reproducible preparation and analysis of surfaces. Characterising the relationship between a surface and an adsorbate, especially the nature of the bonding interaction, is the key to utilising surface science. One of the most important areas of application is in heterogeneous catalysis [6]. The challenge of interpreting fundamental processes at a molecular level can assist in our understanding of processes involved in catalysis, which normally work at higher pressures and temperatures.

The ultimate goal of the surface scientist is a complete understanding of processes such as adsorption, activation and transformation of complex surface species by a solid surface with a view to breaching the 'pressure gap' that exists between surface science and the real commercial world [7 - 9].

1.3 An Introduction to Surface Vibrational Spectroscopic Techniques

Surface vibrational spectroscopic techniques play a central rôle in the analysis of adsorbates on the crystal surface [10]. Analysing a spectrum containing characteristic vibrational frequencies reveals information on the binding geometry and local symmetry of the surface-adsorbate complex. Changes in the spectrum, due to the experimental conditions used, determine surface intermediate species and their subsequent reactions. A complete picture of the reaction pathway is thus established.

One of the most powerful and successfully used vibrational spectroscopic techniques is Electron Energy Loss Spectroscopy (EELS) [11]. The potential of this technique was realised in 1966 when Propst and Piper first detected localised vibrations of adsorbed atoms on a well defined surface [12]. Today EELS has the capability to access a large spectral range with high sensitivity, although compared with optical spectroscopic techniques the resolving power is low. The technique is also restricted to UHV pressures and homogeneous surfaces therefore this exacts a limit on catalytically relevant reactions.

The main optical spectroscopic technique of Reflection-Absorption Infrared Spectroscopy (RAIRS) was first proposed by Greenler [13] in 1966 and realised experimentally by Chesters, Sims and Pritchard on application to single crystal surfaces a few years later [14]. Today using Fourier-transform spectrometers (which have the advantage of a good signal-to-noise ratio over a large spectral range) the spectral resolution of RAIRS remains unsurpassed by any other surface technique. Transmission infrared spectroscopy of catalytically relevant reactions on supported catalysts at high pressures can be performed, although restrictions on the spectral accessibility due to absorption bands associated with the supports are common. Problems exist with the influence by the support on the nature of the adsorption site and the existence of surface irregularities (for example terraces, steps, edges and corners) of the metal surface, thus making alternative adsorption sites available and interpretation of the adsorption species complicated.

The complementary techniques to EELS and RAIRS include Raman spectroscopy, (in particular when applied to metal surfaces), Surface Enhanced Raman Spectroscopy, (SERS) [15], Inelastic Neutron Scattering (INS) [16] and inelastic helium scattering [4]. The combination of techniques provides additional information on modes that may give rise to weak absorptions in the infrared or modes which are not observed in the infrared or by other techniques. A detailed understanding of a particular adsorbate-substrate species is thus elucidated by the range of data obtained by several techniques.

1.4 Thesis Outline

EEL spectrometers have rapidly developed over the last few years to remain competitive to RAIRS in resolution capacity. The lowest resolution recorded of $< 8 \text{ cm}^{-1}$ is that of Ibach *et al* [17].

An advanced EEL spectrometer designed by Froitzheim [18] has been utilised in the studies presented in this thesis. The principles and design features of how the resolution has been enhanced and the performance of the spectrometer are included in Chapters 2 and 3.

During the period that advances in technology have reasserted EELS' position as a successful vibrational spectroscopic technique, a new source has been developed to extend the spectral range of RAIRS. The high brilliance of synchrotron radiation results in a significant intensity advantage over conventional blackbody sources in the region of the

spectrum extending from 1000 cm^{-1} in the mid-infrared region to 50 cm^{-1} in the far-infrared region [19]. This region is of particular interest since it contains the vibrational modes of the majority of direct bonds between the surface and the adsorbate [20]. Until now the observed vibrational modes have resulted from a dipole oriented perpendicular to the surface, a condition enforced by the strict 'metal surface selection rule' [21], based upon the response of the incident infrared light with the dipole moment of the molecule on a metal surface. Recently, parallel modes have been observed in the far infrared region. The apparent breakdown in the surface selection rule has been explained by a theoretical model in which the excitation mechanism is different from simple infrared absorption [22]. Chapter 4 deals with the explanation of this mechanism using the synchrotron source at the Daresbury CCLRC facility.

Hydrogen, both as a reactant or product molecule, is one of the most important adsorbates in the field of heterogeneous catalysis [23]. The synthesis of ammonia, of hydrocarbons or alcohols by means of the Fischer-Tropsch reaction, or solidification of unsaturated fatty acids are only a few examples.

The fact that hydrogen possesses a single valence electron would at first lead one to believe that it should be the simplest reacting adsorbate. However, the vast literature on hydrogen adsorption has demonstrated considerable complexity [23]. The reliability of any conclusions made on the structure and bonding of the adsorbed hydrogen, with regard to the symmetry of the adsorption site, lie with the correct assignment of the

various vibrational modes. The isotope deuterium facilitates the assignment of observed vibrational bands when compared with hydrogen due to the large isotopic shift resulting from the different mass involved. Chapter 5 demonstrates the application of EELS in exploring the nature of the adsorption site occupied by hydrogen on the platinum (111) surface.

1.5 References

- [1] Cohen, Philip, 'Against the odds it worked' in *New Scientist*, 12 July 1997, 4-5.
- [2] D.P. Woodruff and T.A. Delchar, *Modern Techniques of Surface Science*, Second Edition, (Cambridge University Press, 1994)
- [3] C.B. Duke, *J. Vac. Sci. and Technol. B*, 11 (4) 1993 1336-1346
- [4] G.A. Somorjai, *Introduction to Surface Chemistry and Catalysis*, (Wiley, 1994)
- [5] G.A. Somorjai, *Surf. Sci.*, 89 (1979) 496-524
- [6] G.A. Somorjai, *Surf. Sci.*, 300 (1994) 849-866
- [7] P. Stoltze and J.K. Norskov, *Phys. Rev. Letts.*, 55 (1985) 2502-2505
- [8] F.M. Hoffman and M.D. Weisel, *J. Vac. Sci. and Technol. A*, 11 (1993) 1957-1963
- [9] S.T. Ceyer, 'New Mechanisms for Chemistry at Surfaces', *Science*, 249 (1990) 133-139
- [10] *Spectroscopy of Surfaces*, Eds. R.J.H. Clark and R.E. Hester (Wiley, 1988)

- [11] H. Ibach and D.L. Mills, *Electron Energy Loss Spectroscopy and Surface Vibrations*, (Academic press, New York, 1982)
- [12] F.M. Propst and T.C. Piper, *J. Vac. Sci. and Technol.*, 4 (1967) 53
- [13] R.G. Greenler, *J. Chem. Phys.*, 44 (1966) 310
- [14] M.A. Chesters, J. Pritchard and M.L. Sims in *Adsorption-Desorption Phenomena.*, Ed. F. Ricca, (Academic Press, New York, 1972)
- [15] A. Campion in *Methods of Surface Characterisation*, Eds. J.T. Yates and T.E. Madey, Vol 1, (Plenum, New York 1987)
- [16] M.E. Pemble in *Surface Analysis-The Principal Techniques*, Ed. J.C. Vickerman, (Wiley 1997)
- [17] H. Ibach, M. Balden and S. Lehwald, *J. Chem. Soc., Faraday Trans.*, 92 (23) (1996) 4771-4774
- [18] Prof. H. Froitzheim at the University of Erlangen-Nürnberg, Germany
- [19] D.A. Slater, P. Hollins, M.A. Chesters, J. Pritchard, D.H. Martin, M. Surman, D.A. Shaw and I.H. Munro, *Rev.Sci. Instrum.*, 63 (1992) 1547
- [20] P. Hollins, A.A. Davis, D.A. Slater, M.A. Chesters, E.C. Hargreaves, P.M. Parlett, J.C. Wenger and M. Surman, *J. Chem. Soc., Faraday Trans.*, 92(5) (1996) 879-890
- [21] H.A. Pearce and N. Sheppard, *Surf. Sci.* 59 (1976) 205
- [22] A.I. Volokitin and B.N.J. Persson, *Phys. Rev. B*, 52, (1995), 2899-2906
- [23] K. Christmann, *Surf. Sci. Reports* 9, (1988) No. 1-3, 1-163

Chapter Two

Experimental Techniques : Principles and Instrumentation

2.1 Introduction

Part A Electron Energy Loss Spectroscopy (EELS)

2.2 Experimental Details

2.2.1 Chamber

2.2.2 Pumps

2.2.3 Bake-out

2.2.4 Pressure Measurement

2.2.5 Gas Handling and Dosing

2.2.6 Sample Mounting, Manipulation and Temperature Control

2.2.7 Sample Cleaning

2.3 Principles of Electron Energy Loss Spectroscopy

2.3.1 Dipole Scattering

2.3.2 Impact Scattering

2.3.3 Practical Consequences

2.3.4 The Electron Energy Loss Spectrometer

Part B (I) Mid-Infrared Apparatus

2.4 Basic FTIR Theory

2.4.1 The Michelson Interferometer

2.4.2 Resolution

2.4.3 Apodisation

2.4.4 Advantages of FTIR

2.5 Reflection Absorption Infrared Spectroscopy (RAIRS)

2.5.1 Physical Principles

2.6 The Ultra-high Vacuum System

2.6.1 Instrumentation

2.6.2 The Experimental Chamber

2.6.3 Crystal Mounting

2.6.4 Crystal Preparation

2.6.5 Gas Sample Preparation

2.6.6 Recording Spectra

Part B (ii) The Far-Infrared Apparatus

2.7 Introduction: The Synchrotron Radiation Source

2.8. The Ultra-high Vacuum System

2.8.1 Beamline 13.3

2.8.2 Infrared Optics and Instrumentation

2.8.3 The Experimental Chamber

2.8.4 Sample Mounting and Preparation

2.9 References

2.1 Introduction

The main surface techniques employed in the investigative studies presented in this thesis were Electron Energy Loss Spectroscopy (EELS) and Reflection Absorption Infrared Spectroscopy (RAIRS). The secondary techniques of Low Energy Electron Diffraction (LEED) and Auger Electron Spectroscopy (AES) were used as aids in determining surface cleanness and will not be described here as good reviews exist in the literature [1,2,3,4,5]. This chapter is divided into two main sections, A and B. Section A is concerned with EELS; section B is further sub-divided into two parts, describing the experimental details used in the mid-infrared and far-infrared work. The study of 3,3,3-trifluoropropene on Pt (111), (Chapter 3), involved the EEL spectrometer and the mid-IR system. The far-IR beamline at Station 13.3 located at the Daresbury Synchrotron Radiation Source (SRS) was utilised for the study of carbon monoxide on Cu (111), (Chapter 4). The hydrogen on Pt (111) work (Chapter 5) was performed with the EEL spectrometer.

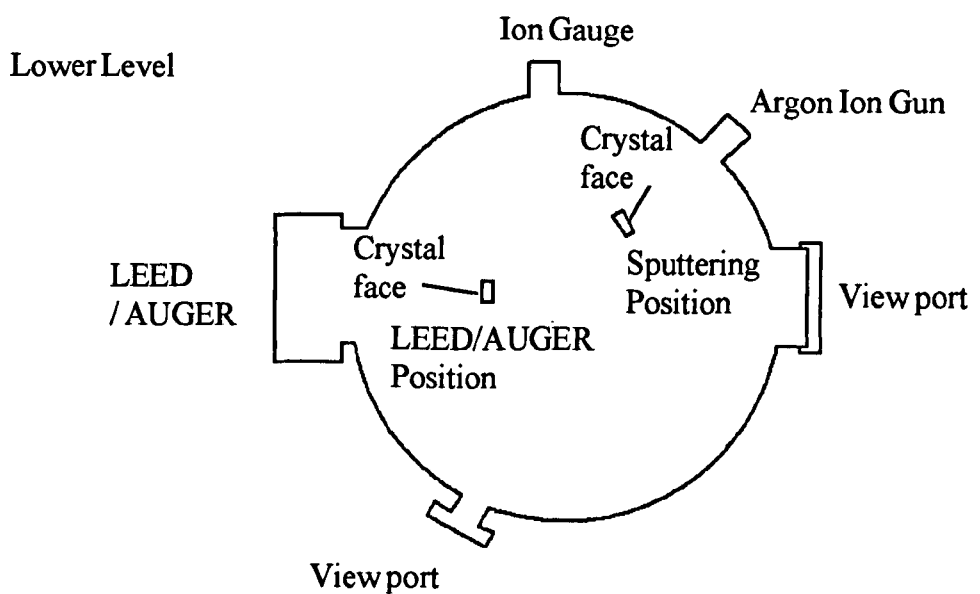
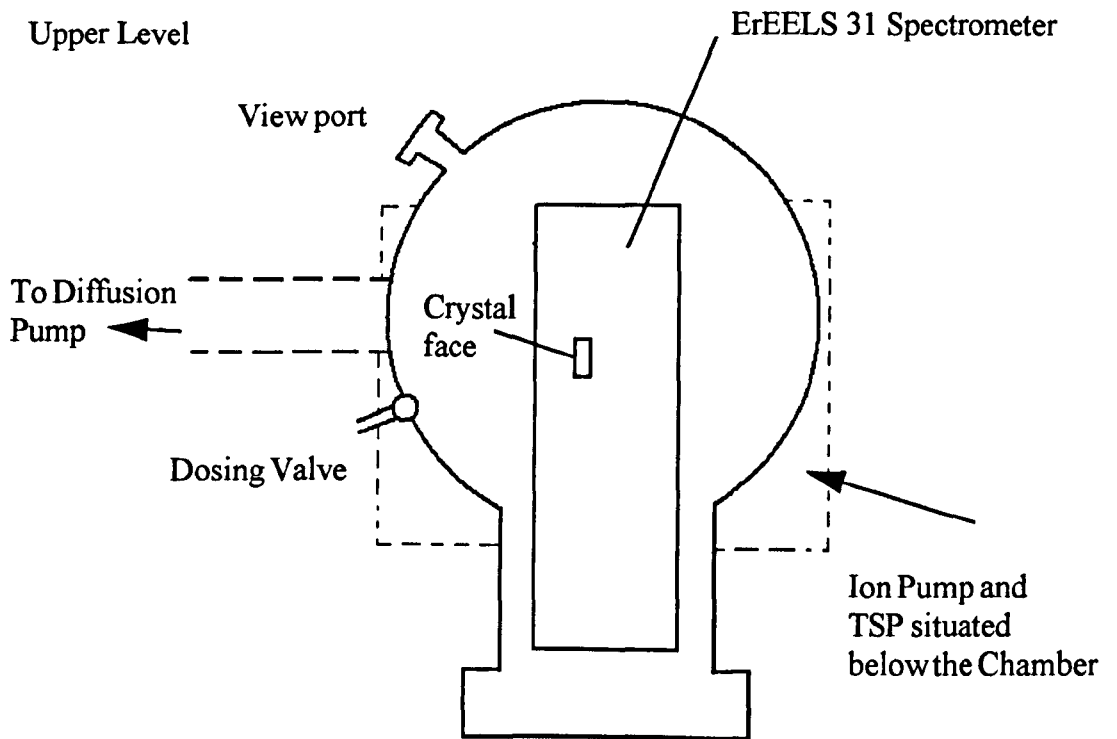
Part A Electron Energy Loss Spectroscopy (EELS)

2.2 Experimental Details

2.2.1 Chamber

The commercially built ultra-high vacuum system supplied by Vacuum Technical Services Ltd. utilised in the following investigative studies is shown schematically in figure 2.1. The construction consisted of a stainless steel bell jar with essentially 2 levels equipped for specialised functions. The upper level comprised a Bayard-Alpert ion gauge (Leybold-Heraeus IE 413 head, IM 510), a 3-grid retarding-field analyser for LEED/AES (VG Scientific), a view port and an argon ion gun for crystal cleaning (VG, AGS-2) equipped with a leak valve for argon gas introduction. The second level incorporated the sample gas leak valve and the EELS spectrometer (VSI ErEELS 31) which was mounted on a flange, in a double Conetic lined cavity, to shield it from magnetic fields. In this way the residual field was less than 10 mGauss. The walls of the chamber were lined with double Conetic magnetic shielding (1.3 mm) as a further precaution.

Figure 2.1 A Schematic Diagram of the EELS Chamber



2.2.2 Pumps

The pumping system consisted of an ion-pump (Leybold-Heraeus NIZ3), a liquid nitrogen trapped oil diffusion pump (Edwards E04) backed by a rotary pump and a water cooled titanium sublimation pump (TSP). A plate valve positioned directly below the main chamber isolated the ion-pump and the diffusion pump was isolated using a gate valve.

2.2.3 Bake Out

The UHV system was baked out at 250 °C for 60 hours using rock wool insulated aluminium panel ovens, which assembled to fit over the whole system above the table. After degassing all filaments, firing the TSP and filling the liquid nitrogen traps of the diffusion pump, once the system had cooled to room temperature a base pressure of 2×10^{-10} mbar was achieved.

2.2.4 Pressure Measurement

The pressure in the main chamber was measured with a Bayard-Alpert nude ion gauge (Leybold-Heraeus IM 51 head, IE 413). The working range of the gauge with an emission current of 0.6 mA was 10^{-10} - 10^{-4} mbar. The backing pressure of the diffusion pump was checked using a Pirani gauge (Thermovac TR201).

2.2.5 Gas Handling and Dosing

The gas handling system consisted of bakeable metal valves which led to the sample gas leak valve, enabling gases to be introduced into the chamber. A glass-gas handling line was attached to each metal valve *via* a glass to metal seal. Gas bulbs were attached *via* Youngs' joints with an 'O' ring seal. These were separated from the glass line by a double tap arrangement incorporating Youngs' greaseless taps. The purity of the gases was checked using a mass spectrometer on a different vacuum system and were used without further purification. The gas-line pumping system consisted of a diffusion pump backed by a rotary pump, which enabled the dosing line to be evacuated to a pressure of 1×10^{-7} mbar monitored with a Penning gauge (Edwards 1002).

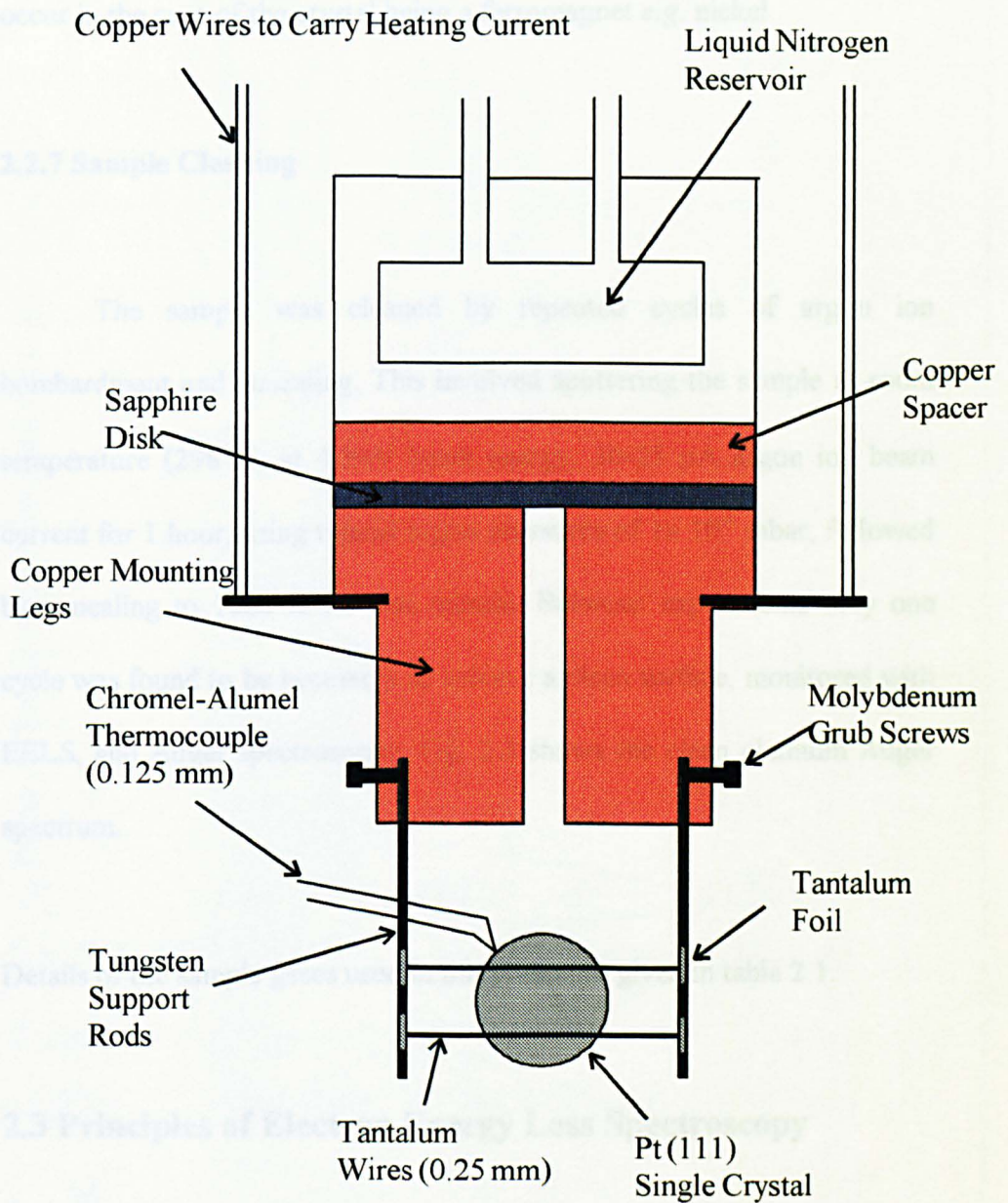
To avoid decomposition of the gas in the ion pump whilst dosing, the pump was switched off, although pumping was maintained by the diffusion pump. The EELS filament was switched off during dosing to preserve its lifetime. After completion of dosing the pressure was allowed to recover to at least 1×10^{-8} mbar before the ion pump was switched on again.

The dosing unit of a Langmuir is defined as a pressure of 1×10^{-6} Torr for 1 second, which is equivalent to 1×10^{-7} Torr for 10 seconds or 1×10^{-8} Torr for 100 seconds. ($1 \text{ Torr} \cong 1.333 \text{ mbar}$).

2.2.6 Sample Mounting, Manipulation and Temperature Control

The sample mount is illustrated in fig. 2.2. The crystal was mounted on sample holders attached to an XYZ θ manipulator such that the crystal face was 'proud' of the supports. This arrangement minimised the possibility of sputtering metal off the supports and thus contaminating the crystal and reduced the possibility of reflecting electrons off a support rod. The sample was cooled by liquid nitrogen. At the end of the manipulator liquid nitrogen was passed through a small copper reservoir, which was connected to a copper spacer. In between the spacer and two isolated copper mounting legs was fitted a sapphire disk (30 mm in diameter, 1 mm thick), which was evenly inserted so that it is kept flat. The special properties of sapphire (in being an electric insulator and a thermal conductor) were used to permit heat transfer from the liquid nitrogen reservoir whilst keeping the two separate copper mounting legs electrically isolated. The importance of electrically isolating the part of the sample mount entering the scattering chamber will be discussed further in section 2.3.4. The copper heating wires were connected to the mounting legs *via* molybdenum grub screws. At the end of the mounting legs two tungsten support rods (2 mm diameter) were fitted with molybdenum grub screws and to increase the contact of the screws with the tungsten rods, copper foil pads were introduced between them. The Pt (111) crystal was mounted by threading tantalum (Ta) wires (2 x 0.25 mm diameter) through spark-cut holes in the crystal that were then spot welded to Ta strips pre-

Figure 2.2 A Schematic Diagram of the Sample Mount used for EELS Measurements



welded to the tungsten support rods. A thermocouple junction of chromel-alumel (0.125 mm diameter) fitted into a hole in the top of the crystal to monitor temperature. The materials used for the construction of the sample mount were non-ferromagnetic. This is to avoid stray magnetic fields influencing the path of the electrons. The sample was heated resistively using an A.C. supply. This avoided magnetising the crystal which can occur in the case of the crystal being a ferromagnet *e.g.* nickel.

2.2.7 Sample Cleaning

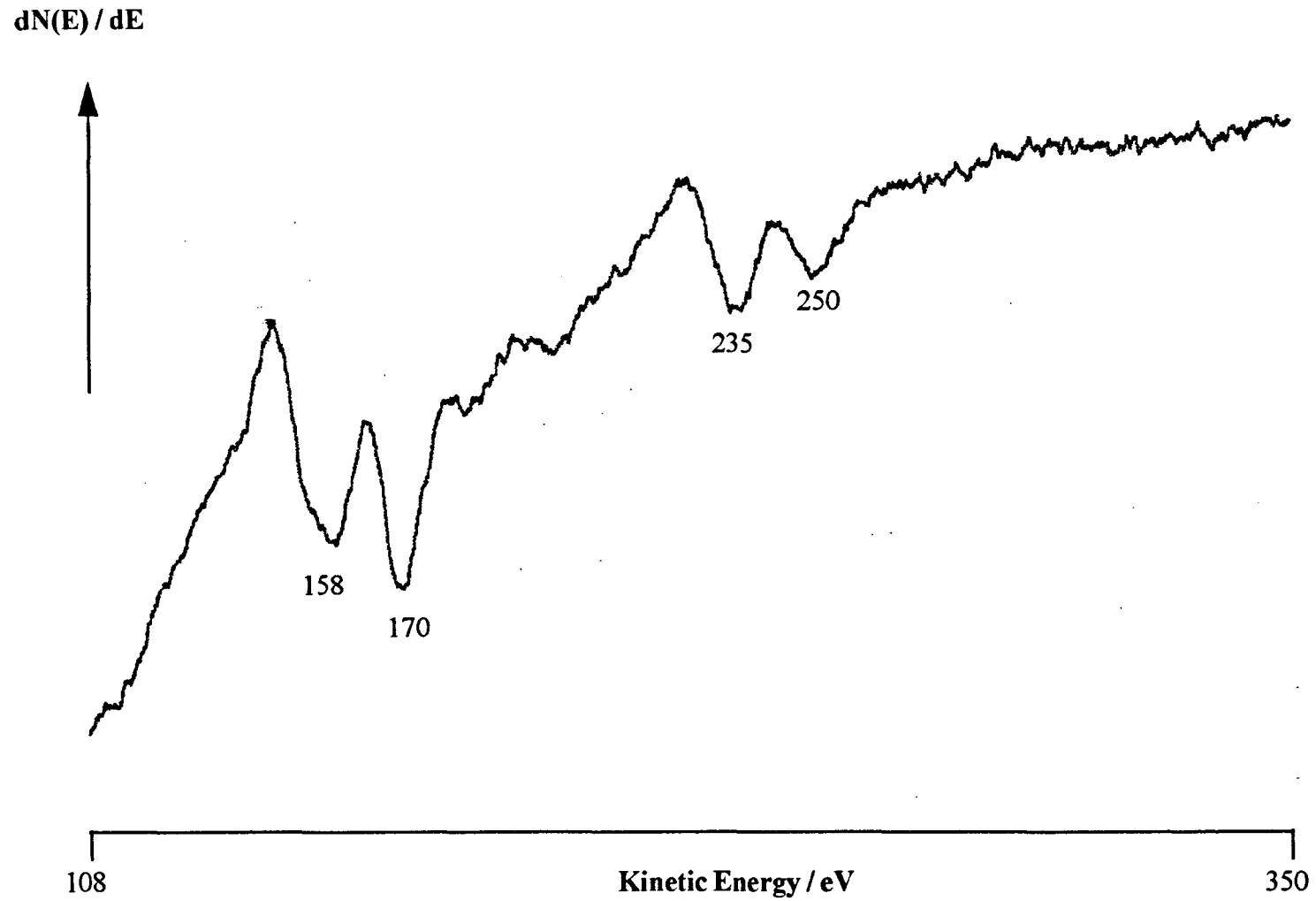
The sample was cleaned by repeated cycles of argon ion bombardment and annealing. This involved sputtering the sample at room temperature (298 K) at 4 keV beam energy, 30-35 μA argon ion beam current for 1 hour, using typical argon pressures of 1×10^{-5} mbar, followed by annealing to 1000 K for one minute. Between experiments only one cycle was found to be necessary to achieve a clean surface, monitored with EELS, and Auger spectroscopy. Fig. 2.3 shows the clean platinum Auger spectrum.

Details of the sample gases used in this thesis are given in table 2.1.

2.3 Principles of Electron Energy Loss Spectroscopy

Electron Energy Loss Spectroscopy (EELS) is a well established technique for stimulating and therefore measuring vibrations at surfaces,

Figure 2.3 The AES Spectrum of the Clean Pt (111) Surface



Gas	Supplier	Purity %	Comments
Argon	BOC	99.999	~700 Torr stored in a glass bulb. N.f.p.
Oxygen	BOC	99.999	~700 Torr stored in a glass bulb. N.f.p.
Hydrogen	BOC	99.999	~700 Torr stored in a glass bulb. N.f.p.
Deuterium	BOC	99.999	~700 Torr stored in a glass bulb. N.f.p.
Carbon Monoxide	Messer Griesheim	99.997	N.f.p
3,3,3 Trifluoropropene	Fluorochem	99.0	N.f.p

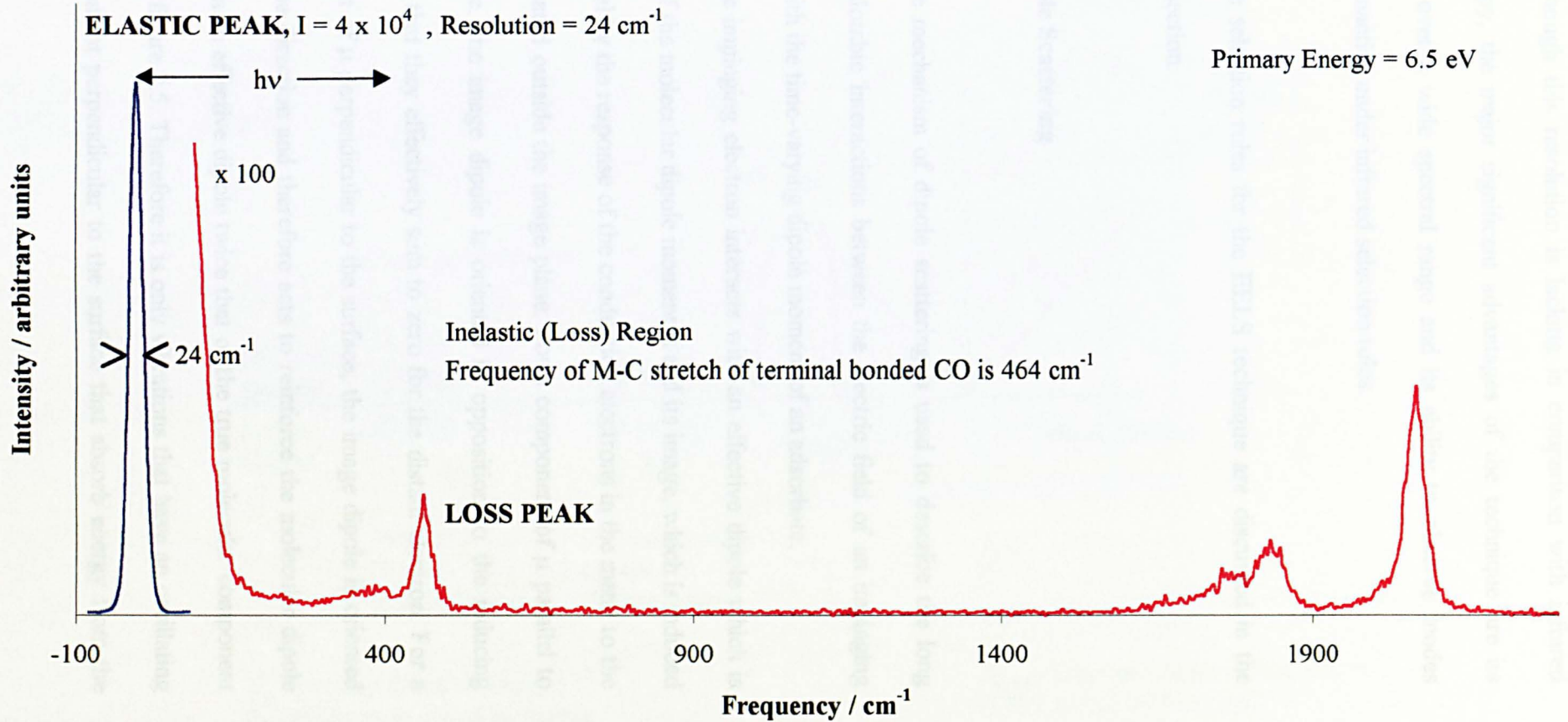
Table 2.1 Sample gases and preparation procedures. N.f.p. = No further purification.

allowing investigations probing a wide variety of clean surfaces and adsorbates [6,7].

The EELS experiment involves the measurement of the energy distribution of a beam of highly monochromatic electrons when it has been scattered from a surface. A more detailed account of the method for producing a monochromatic beam with typically 3-5 meV energy distribution and primary energy, E_p , between 1-10 eV will be described in section 2.3.4. The beam is accelerated onto the sample at an incident angle θ_i to the surface normal. The sample is usually a single crystal. The majority of the incident electrons scattered back by the surface do not exchange any energy with the surface and are elastically scattered in the specular direction ($\theta_i = \theta_r$). Approximately 1% (for a chemisorbed layer covered metal surface) of the electrons are reflected, exchanging energy with the surface. These electrons are inelastically scattered, a process in which they lose (or gain) quanta of energy corresponding to the excitation or de-excitation of a vibrational mode of the surface itself or of a species adsorbed at the surface. A composite energy spectrum of both the elastic and inelastic scattered electrons comprises of a dominating elastic peak, of the elastically scattered electrons, and loss features, where the quantum of vibrational energy is measured as the separation distance between the loss feature and the elastic peak. This is illustrated in figure 2.4.

The vibrational spectrum of the surface species can be used to determine the molecular structure and adsorption site geometry of the adsorbate layer. Until recently a typical resolution was 5-10 meV.

Figure 2.4 A Typical Composite Energy Spectrum Obtained From the EELS Experiment



Although this resolution is lacking in comparison with infrared spectroscopy, the major significant advantages of the technique are its sensitivity over a wide spectral range and its ability to observe modes which are inactive under infrared selection rules.

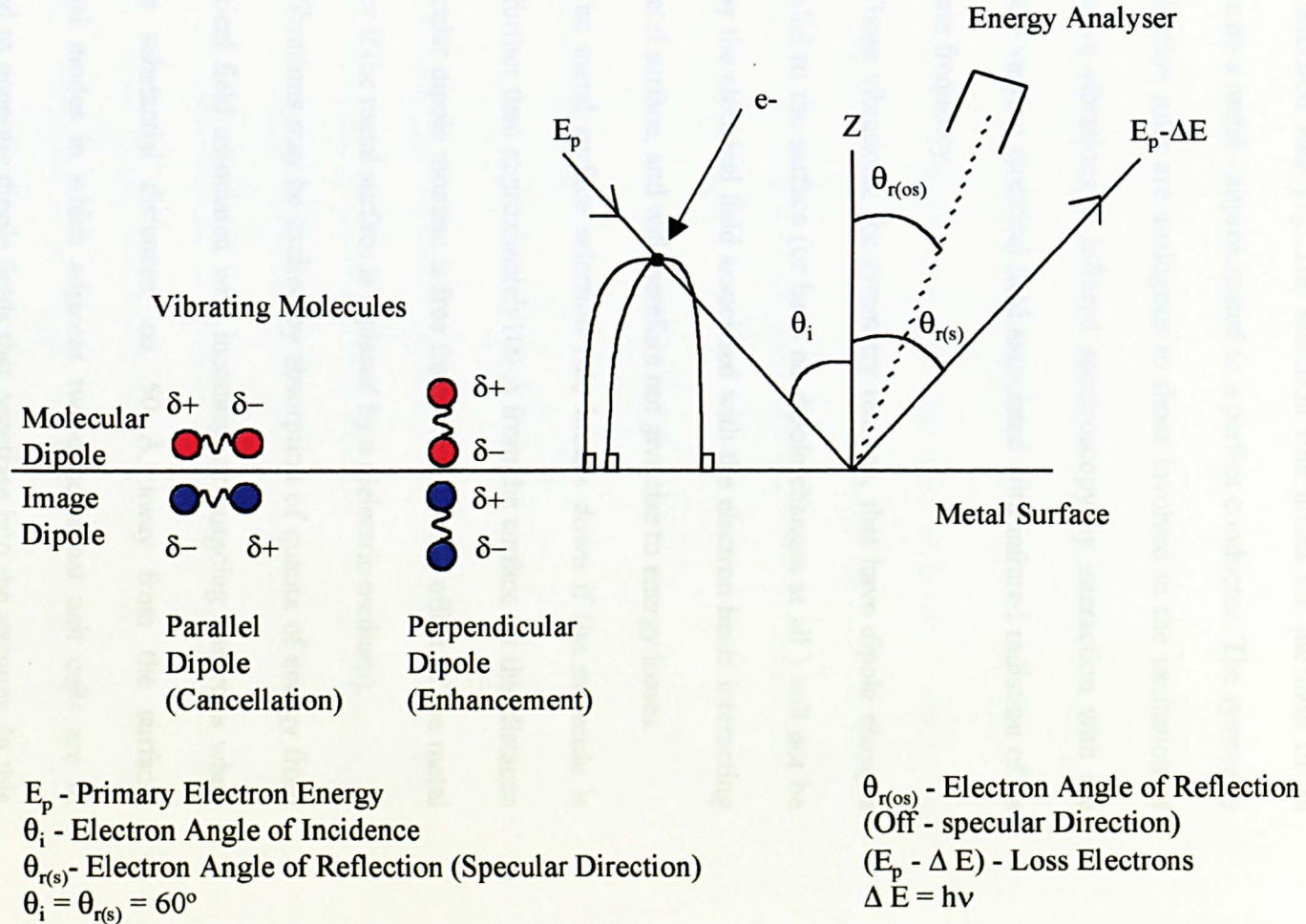
The selection rules for the EELS technique are discussed in the following section.

2.3.1 Dipole Scattering

The mechanism of dipole scattering is used to describe the long range Coulombic interactions between the electric field of an impinging electron with the time-varying dipole moment of an adsorbate.

The impinging electron interacts with an effective dipole which is made up of the molecular dipole moment μ and its image, which is induced in the metal by the response of the conduction electrons in the metal to the dipole situated outside the image plane. For a component of μ parallel to the surface, the image dipole is oriented in opposition to the inducing dipole, so that they effectively sum to zero for the distant electron. For a component of μ perpendicular to the surface, the image dipole is oriented in the same direction and therefore acts to reinforce the molecular dipole resulting in an effective dipole twice that of the true molecular component observed, figure 2.5. Therefore it is only vibrations that have an oscillating dipole moment perpendicular to the surface that absorb energy from the

Figure 2.5 A Schematic Diagram of the EELS Principle



electron beam. This results because the lines of force associated with the incoming electrical field are distorted such that they are terminated perpendicular to the metal surface. This phenomenon results in the *metal surface selection rule* [7]. The selection rule arises for the case of an adsorbate on a metal - approximated to a perfect conductor. The symmetry based selection rules are analogous to those involved in the excitation of dipole active vibrations in infrared spectroscopy by interaction with the sinusoidally varying electrical field associated with infrared radiation of an appropriate frequency.

Those vibrations, for symmetry reasons, that have dipole changes only parallel to the surface (or have no dipole changes at all) will not be excited by the electrical field associated with the electron beam interacting with a metal surface, and will therefore not give rise to energy losses.

The metal surface selection rule breaks down if the molecule is situated further than approximately 100 Å from the surface (at this distance the molecular dipole moment is free from the screening effect of the metal surface; or if the metal surface is replaced by a dielectric medium).

Vibrations may be excited by absorption of quanta of energy from the electrical field associated with incoming or outgoing electrons when these are substantial distances, *ca.* 50 Å, away from the surface. Vibrational modes in which adjacent two-dimensional unit cells are in phase tend to generate dipole fields that penetrate into the vacuum. In this case the wavelength (λ) of the surface phonon is large, the momentum ($\propto 1/\lambda$) is small, and by conservation of momentum there is little momentum

change parallel to the surface and the dipole excitation mechanism leads to near-specular scattering. See fig 2.6.

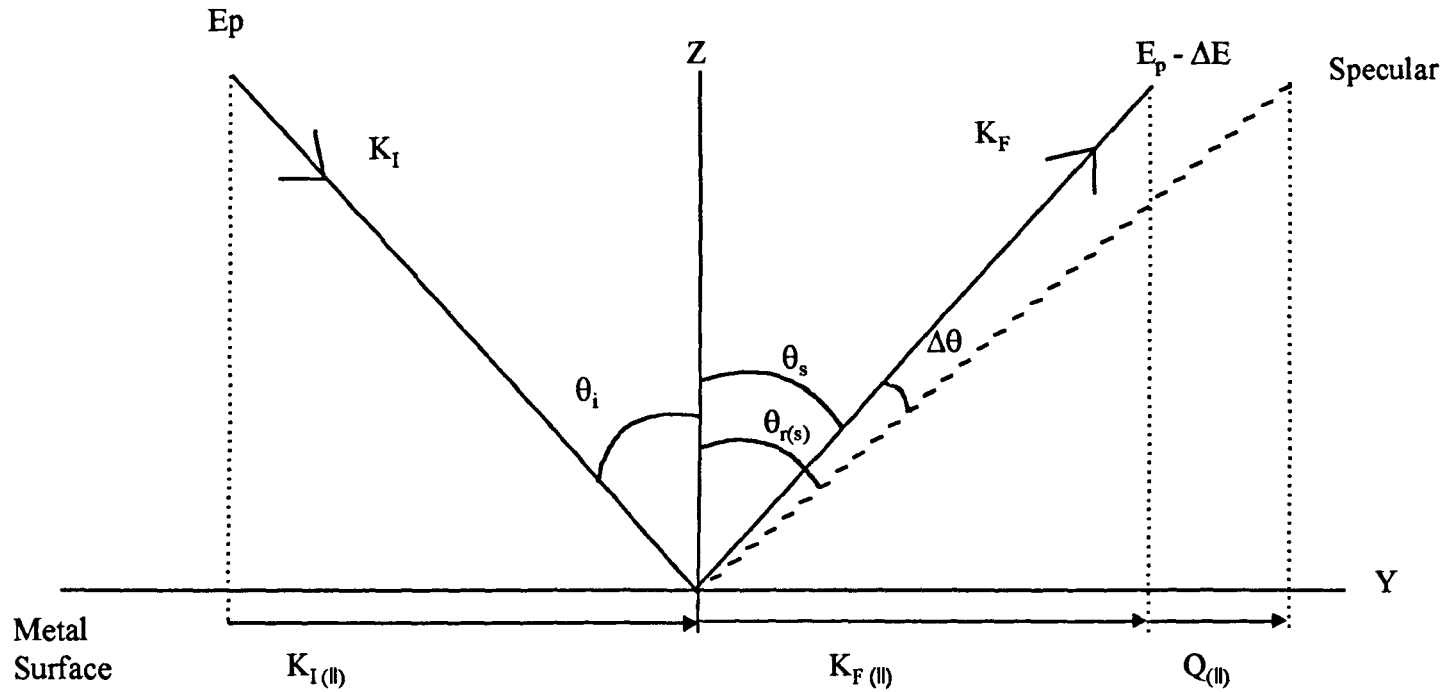
If $K_{I \parallel}$ is the momentum of the incident electron parallel to the surface, $K_{F \parallel}$ is the momentum of the outgoing electron parallel to the surface and Q_{\parallel} is the momentum of the phonon generated, then by conservation of momentum, $K_{I \parallel} = K_{F \parallel} + Q_{\parallel}$. See fig. 2.6. When Q_{\parallel} is finite but small as is the case for dipolar scattering, where the transfer ($h\nu$) is small compared to the primary energy, the electrons are scattered strongly forward but slightly away from the specular direction. The polar plot of the predicted scattering density is shown in fig 2.7. The lobe is approximately $1-2^\circ$ away from the specular direction on the normal side of the outgoing specular beam.

2.3.2 Impact Scattering

The mechanism of impact scattering is applied when short range interactions dominate. It is principally a collision between the electron and the vibrating molecule. The incident electron effectively breaks through the electronic screening effect of the metal surface to impact directly with the vibrational motion of the adsorbate-substrate surface atoms. A classical electrostatic interaction is no longer an accurate description of this mechanism and a full quantum mechanical model is required [8,9].

The expected impact intensity of impact modes in the specular direction is about 100 times lower than that of the observed dipolar modes.

Figure 2.6 Conservation of Momentum Parallel to the Surface



θ_i - Electron Angle of Incidence

$\theta_{r(s)}$ - Electron Angle of Reflection (Specular Direction)

θ_s - Scattered Angle of Electron

$\Delta E = h\nu$

$\Delta\theta = 1-2^\circ$

K_I - Incoming Momentum of Electron

K_F - Outgoing Momentum of Electron

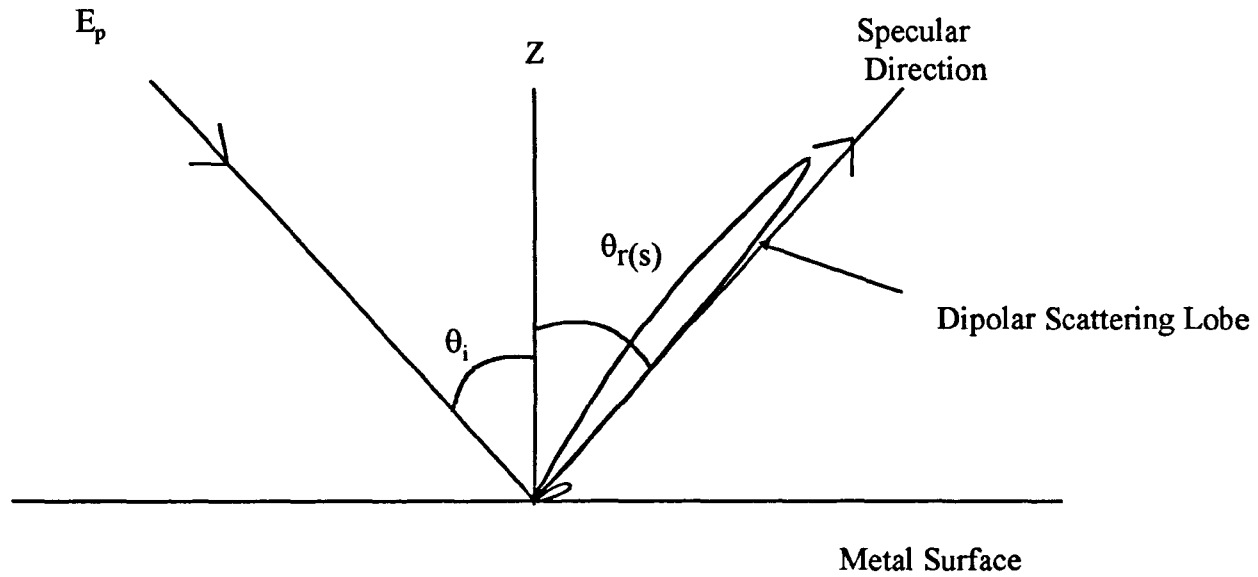
$$K_{I(II)} = K_{F(II)} + Q_{(II)}$$

$K_{I(II)}$ = Parallel Momentum of Incoming Electron

$K_{F(II)}$ = Parallel Momentum of Outgoing Electron

$Q_{(II)}$ = Parallel Momentum of Phonon

Figure 2.7 Polar Plot of Scattering Intensity in the plane of Incidence



- E_p - Primary Electron Energy
- θ_i - Electron Angle of Incidence
- $\theta_{r(s)}$ - Electron Angle of Reflection (Specular Direction)
- $\theta_i = \theta_{r(s)} = 60^\circ$

This is because phonons of all wavelengths are excited and the electrons are isotropically scattered as the momentum change can be large. Thus far fewer electrons can be detected by the analyser in an on-specular geometry. Impact scattered electrons will predominate in a spectrum taken in an off-specular geometry. See fig. 2.6.

At higher loss energies, modes that have a dipole contribution are not measured as effectively *e.g.* C-H stretching modes, thus the emphasis changes from dipole to impact scattering measurements. Modes that have a high amplitude of motion *e.g.* hydrogenic modes, have a strong impact contribution in which case measurements in an off-specular geometry are favoured.

Symmetry based vibrational selection rules apply to the impact scattering mechanism [10].

a) If a vibration is antisymmetric with respect to a 2-fold axis of the adsorption complex (axis is perpendicular to the surface), then that vibration will be impact forbidden in the specular direction, although allowed off-specular.

b) If a vibration is antisymmetric with respect to a plane of symmetry of the adsorption complex that is itself perpendicular to the plane of incidence, it will also be impact forbidden in the specular direction but it may be allowed off-specular in the plane of incidence.

c) If a vibration is antisymmetric with respect to a plane of symmetry parallel to the plane of incidence, then that vibration will be altogether

impact forbidden, on or off-specular in the plane of incidence, but it may be allowed off-specular in other planes.

Rules a) and b) are derived from considerations of the time reversibility of the scattering process and on the assumption that the energy loss is small compared with the energy of the incident electron beam. Selection rule c) is not dependant on the latter assumption.

2.3.3 Practical Consequences.

A comparison can be made between the two electron scattering mechanisms in EELS from an angular profile: The loss spectrum associated with large angle, off-specular scattering, where impact scattering dominates and the near specular loss spectrum where dipole scattering may be observed. This permits identification of the excitation mechanism of each mode in the spectrum. By exploiting the selection rules for dipole and impact scattering the symmetry of each observed mode and adsorbate geometry may be deduced. It is clear that EELS is invaluable in identifying the chemical and structural nature of an adsorbed species.

2.3.4 The Electron Energy Loss Spectrometer

The EEL spectrometer used in these experiments was a commercially built ErEELS 31 which was designed at the University of Erlangen by Prof. H Froitzheim. This is shown schematically in figures

2.8.a and 2.8.b. The basic arrangement consists of an electron gun, a monochromator, an analyser and a detector.

The fixed monochromator with electron gun and output lens consists of a double toroidal condenser with 30 mm mean dispersive radius (horizontal plane) and 62.5 mm radius (vertical plane) in the pre-monochromator. The main monochromator has a mean dispersive radius of 60 mm (horizontal plane) and a radius of 78.5 mm (vertical plane). The cathode is a tungsten hairpin filament. The output lens transmits and focuses electrons from the monochromator to the input lens of the analyser through the scattering chamber (diameter 50 mm).

The rotatable analyser with input lens and single channeltron detector is a toroidal condenser. The main analyser has a dispersive radius of 60 mm and a radius of 78.5 mm, and the second analyser has a dispersive radius of 30 mm.

The deflection potential applied between the inner and outer electrodes of the toroidal condensers determines the pass energy of the electron beam reaching the sample and the detector. The lower resolution pre-monochromator ensures a high flux of electrons leaving the electron gun with an energy spread of *ca.* 0.3 eV which is reduced to 20-30 meV half-width before being further reduced after exiting the main monochromator to 2-5 meV. The absolute intensity is maximised by using an intermediate deceleration lens between the pre and the main monochromators. Thus the potentials are imaged from the exit slit of the pre-monochromator to the entrance slit of the main monochromator. The

Figure 2.8. a A Schematic Representation of the ErEELS 31 Spectrometer

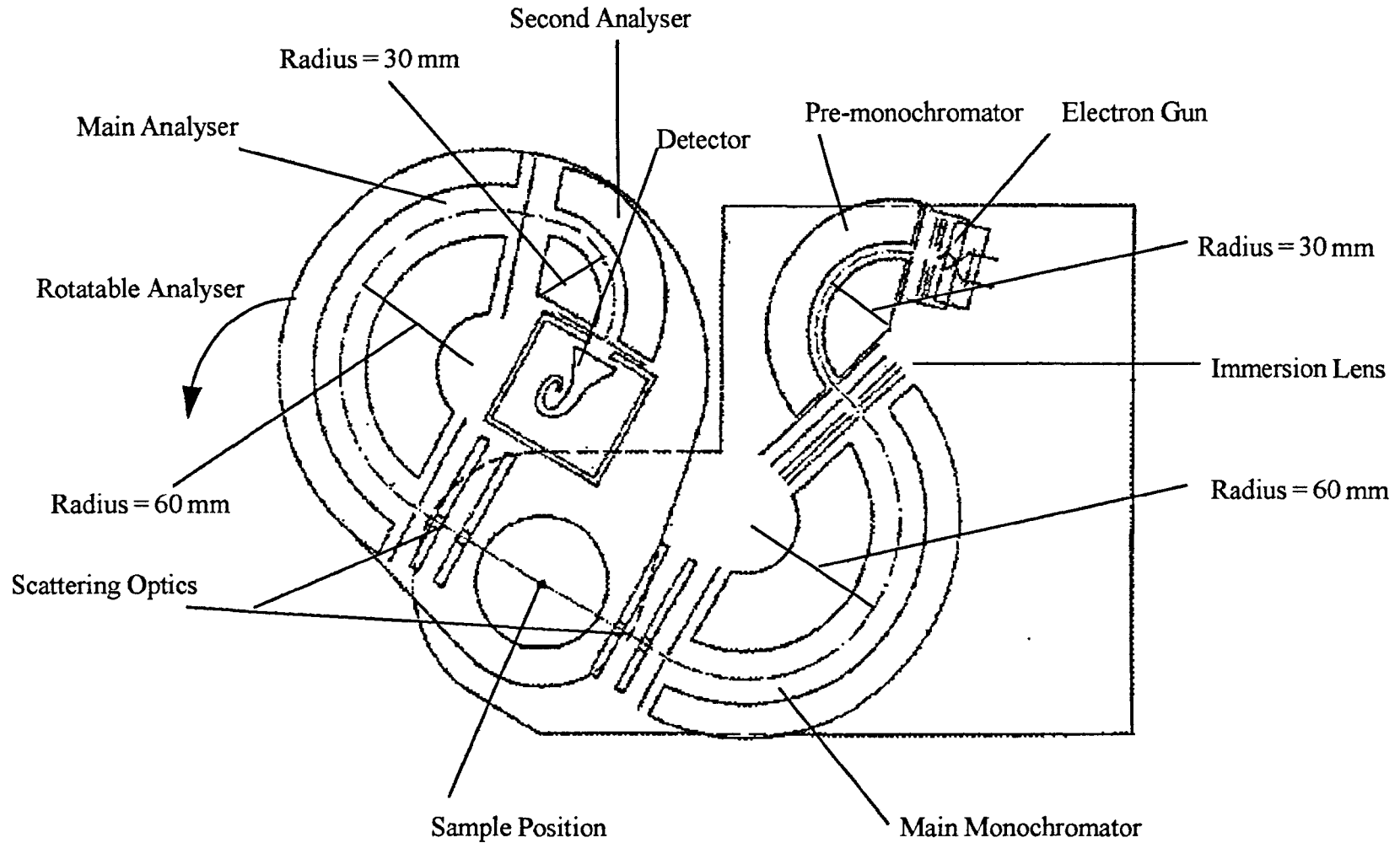
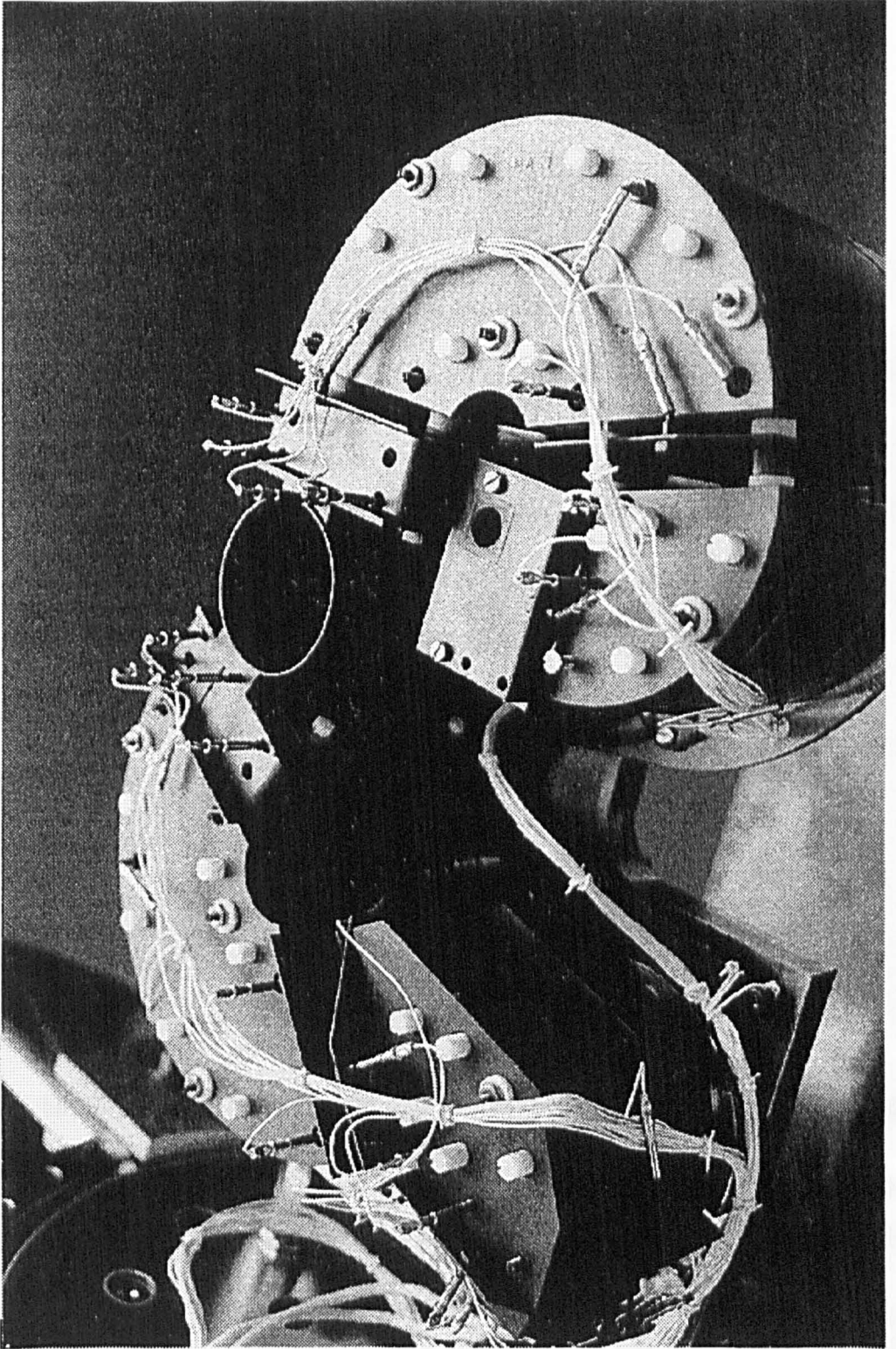


Figure 2.8.b A Photograph of the ErEELS 31 Spectrometer



scattering optics accelerate the electron beam from the monochromator to the sample. The scattering chamber determines the primary energy as the cathode is set at ground potential. The scattering optics then decelerate the electron beam into the main analyser and eventually into the secondary analyser and detector. The pass energy of the main monochromator capacitor is set to the same value as the main and second analysers.

Toroids with different radii perpendicular and parallel to the dispersion plane collect the electrons in two directions whilst maintaining a stronger focusing power than simple cylindrical capacitors.

Electrodes placed on the top and the bottom of the capacitors serve to reduce 'space-charge' effects. The space charge effect is the result of electron-electron repulsion which causes a spreading of the electron beam. This effect is greatest at low electron kinetic energies and high electron flux. This is important in the pre-monochromator as there is a high current density. The electrodes reduce the repulsive spreading.

The stability of a digital power supply which controls a personal computer allows individual automatic optimisation of all elements of the spectrometer.

The ErEELS 31 offers the advantage of increased current at lower resolution.

Initial set-up involved maximising the current at the front end of the channeltron, monitored using a Keithley electrometer, by adjusting the spectrometer potentials to obtain their optimum values. This was undertaken in the straight-through position with no sample in the scattering

Figure 2.9.a Chart Showing the Expected Intensities at Given Resolutions (Manufacturers Specifications) for the ErEELS 31

ΔE - Resolution (meV)	Intensity (pA)
10	1000
9	730
8	510
7	340
6	210
5	120
4	65
3	27
2	8
1	1

These values are plotted in figure 2.9.b together with the 'in-house' performance for comparison. The elastic peak gained from this performance is shown in figure 2.9.c.

Figure 2.9.b An Intensity Resolution Plot Comparing Manufacturers Performance with In-house Performance

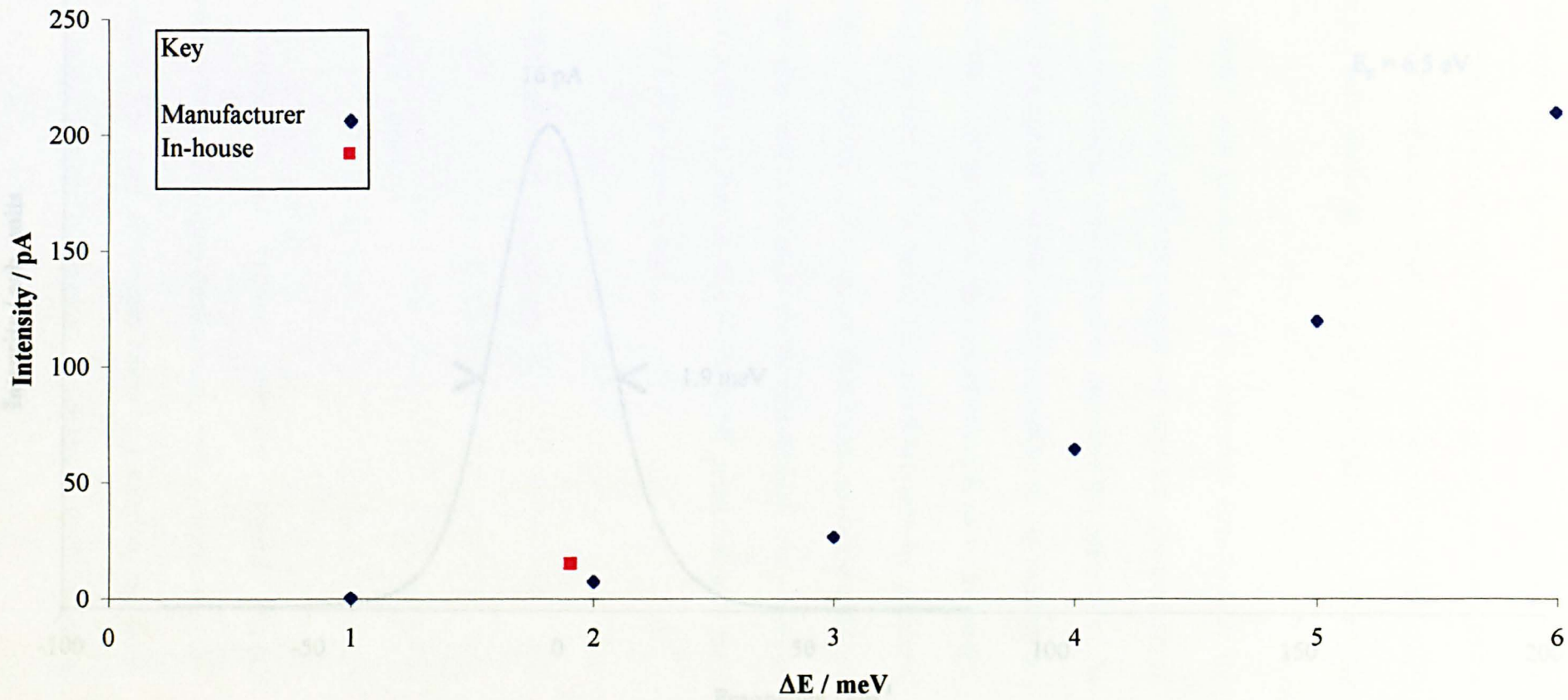
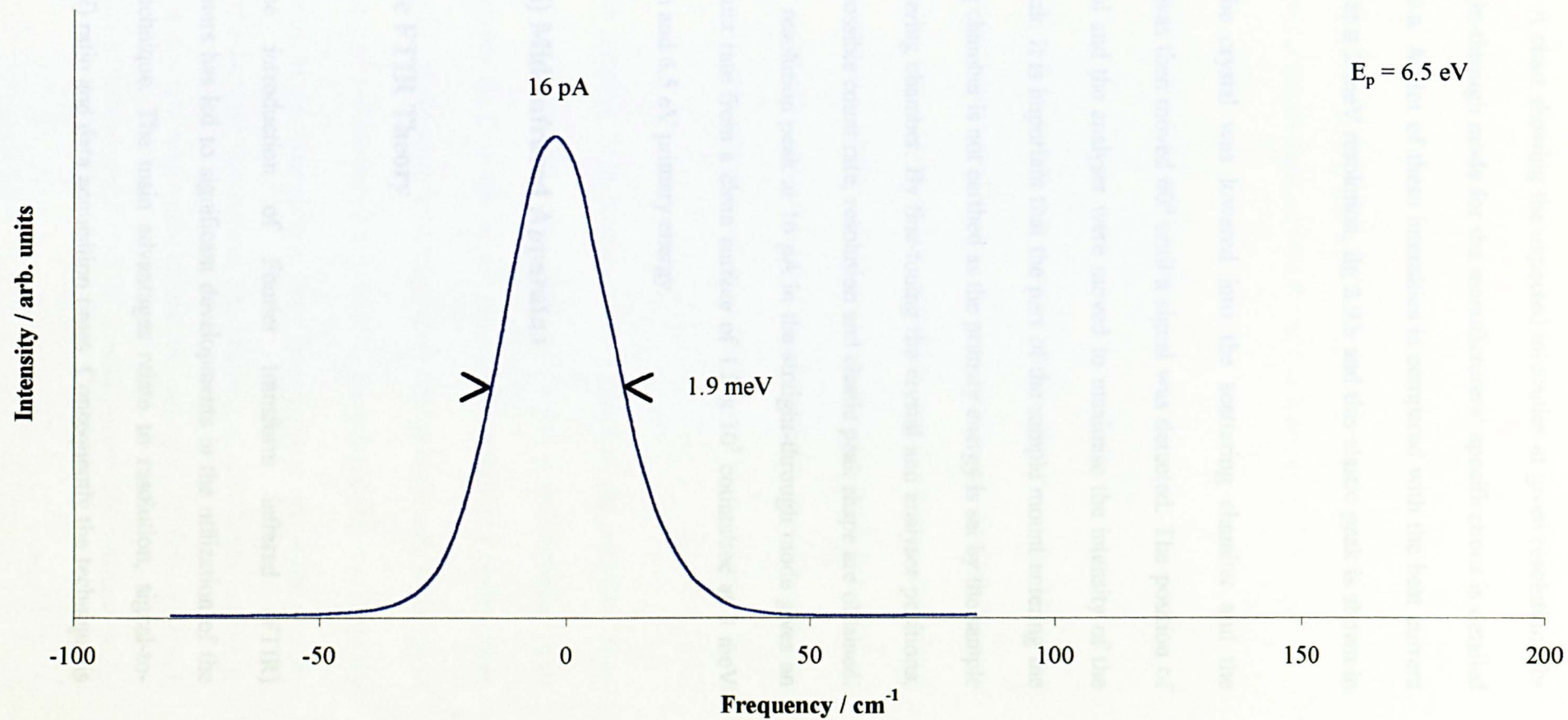


Figure 2.9.c A Typical Elastic Peak Recorded at 1.9 meV Resolution



chamber. A chart showing the expected intensities at given resolutions for the straight-through mode for the manufacturers' specifications is detailed in fig. 2.9.a. A plot of these intensities is compared with the best current achieved at $\cong 2$ meV resolution, fig 2.9.b and this elastic peak is shown in fig. 2.9.c.

The crystal was lowered into the scattering chamber and the analyser was then moved 60° until a signal was detected. The position of the crystal and the analyser were moved to maximise the intensity of the elastic peak. It is important that the part of the sample mount entering the scattering chamber is not earthed as the primary energy is set by the sample plus scattering chamber. By fine-tuning the crystal and analyser positions, the best possible count rate, resolution and elastic peak shape are obtained. A 2 meV resolution peak at 16 pA in the straight-through mode gives an elastic count rate from a clean surface of 1.2×10^5 counts/sec at 3 meV half-width and 6.5 eV primary energy.

Part B(i) Mid-Infrared Apparatus

2.4 Basic FTIR Theory

The introduction of Fourier transform infrared (FTIR) spectrometers has led to significant developments in the utilization of the RAIRS technique. The main advantages relate to resolution, signal-to-noise (S/N) ratio and data acquisition times. Consequently the technique is

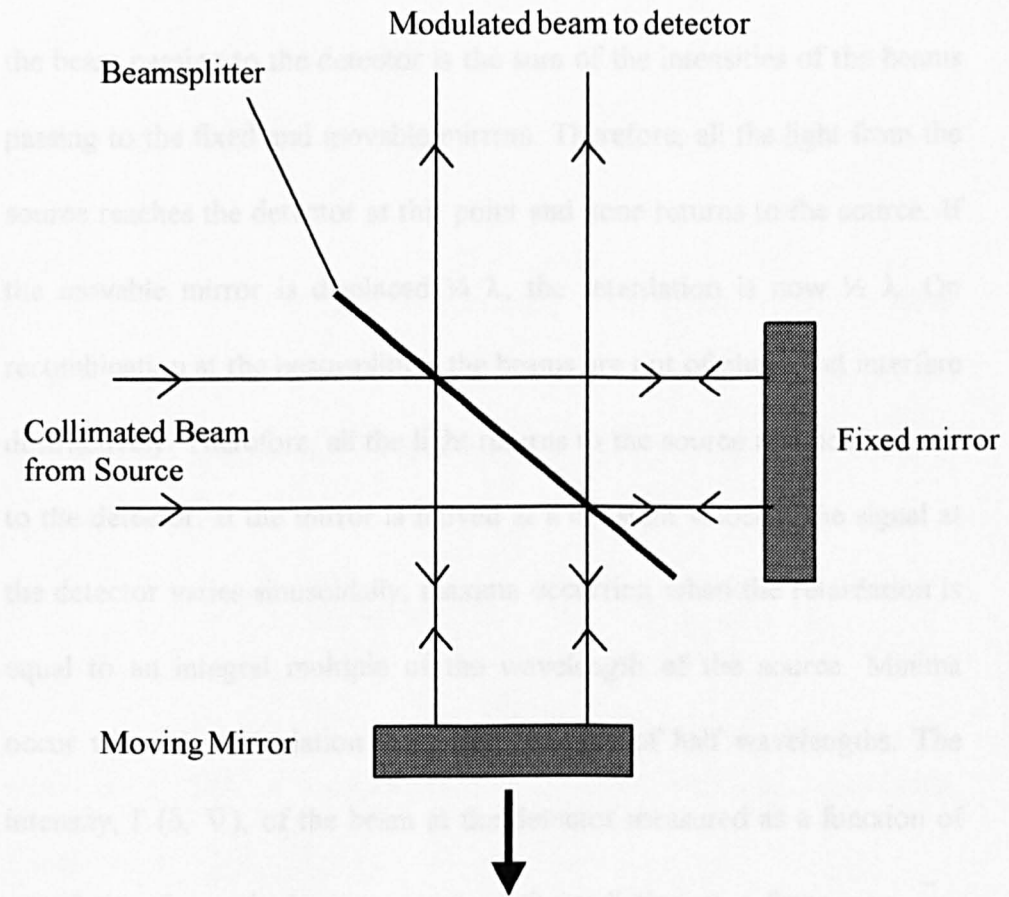
no longer restricted to strong infrared absorbers such as CO or carboxylate groups, but weak absorbers, such as hydrocarbons, can now be routinely investigated on metal single crystal surfaces. A brief description of basic FTIR theory [11,12] and the advantages it provides are explained here as a preliminary to the discussion of the RAIRS technique [13-18].

2.4.1 The Michelson Interferometer

The central component of an FTIR spectrometer is the Michelson Interferometer represented in fig 2.10. It is a device that divides a beam of radiation into two paths and then recombines the two beams after a path difference has been introduced. Interference between the two beams can therefore occur. The intensity variations of the beam emerging from the interferometer can be measured as a function of path difference by a detector.

The simplest form consists of two mutually perpendicular plane mirrors, one of which can move along an axis that is perpendicular to its plane. Between the fixed mirror and the movable mirror is a beamsplitter, where a beam of radiation from an external source is partially reflected to the fixed mirror and partially transmitted to the movable mirror. After the beam returns to the beamsplitter, they interfere and are again partially reflected and partially transmitted. The intensity of each beam passing to the detector and returning to the source depends on the difference in path of the beams in the two sections of the interferometer. The variation in the

Figure 2.10 The Michelson Interferometer



$$I(\nu) = 0.5 I_0 [1 + \cos(2\pi \nu \delta)] \quad \text{Equation 2.1}$$

$I(\nu)$ is the source intensity distribution

intensity of the beams passing to the detector and returning to the source as a function of the path difference ultimately yields the spectral information in a FT spectrometer.

The path difference between the beams is equal to twice the moving mirror displacement. This is the optical retardation, δ . When the fixed and movable mirrors are the same distance from the beamsplitter, zero retardation, the two beams interfere constructively and the intensity of the beam passing to the detector is the sum of the intensities of the beams passing to the fixed and movable mirrors. Therefore, all the light from the source reaches the detector at this point and none returns to the source. If the movable mirror is displaced $\frac{1}{4} \lambda$, the retardation is now $\frac{1}{2} \lambda$. On recombination at the beamsplitter, the beams are out of phase and interfere destructively. Therefore, all the light returns to the source and none passes to the detector. If the mirror is moved at a constant velocity, the signal at the detector varies sinusoidally, maxima occurring when the retardation is equal to an integral multiple of the wavelength of the source. Minima occur when the retardation is an odd multiple of half wavelengths. The intensity, $I'(\delta, \bar{\nu})$, of the beam at the detector measured as a function of retardation for a single component of the radiation at a frequency, $\bar{\nu}$, expressed in wavenumbers (cm^{-1}) is given by Equation 2.1.

$$I'(\delta, \bar{\nu}) = 0.5 I(\bar{\nu}) [1 + \cos(2\pi \bar{\nu} \delta)] \quad \text{Equation 2.1}$$

$I(\bar{\nu})$ is the source intensity distribution.

In ideal terms a beamsplitter is a non-absorbing film whose reflectance and transmittance are both exactly 50%. In practice these characteristics are impossible to find. The amplitude of the interferogram is affected by a number of factors including beamsplitter efficiency, detector response to the wavenumber range and amplifier characteristics. The simplest equation representing the interferogram therefore becomes, Equation 2.2.

$$I(\delta) = B(\bar{\nu}) \cos(2\pi\delta\bar{\nu}) \quad \text{Equation 2.2}$$

Where $B(\bar{\nu})$ represents the source intensity at frequency $\bar{\nu}$ with the effect of all instrumental characteristics included. For a broad band source the interferogram is expressed by the integral over all frequencies, Equation 2.3.

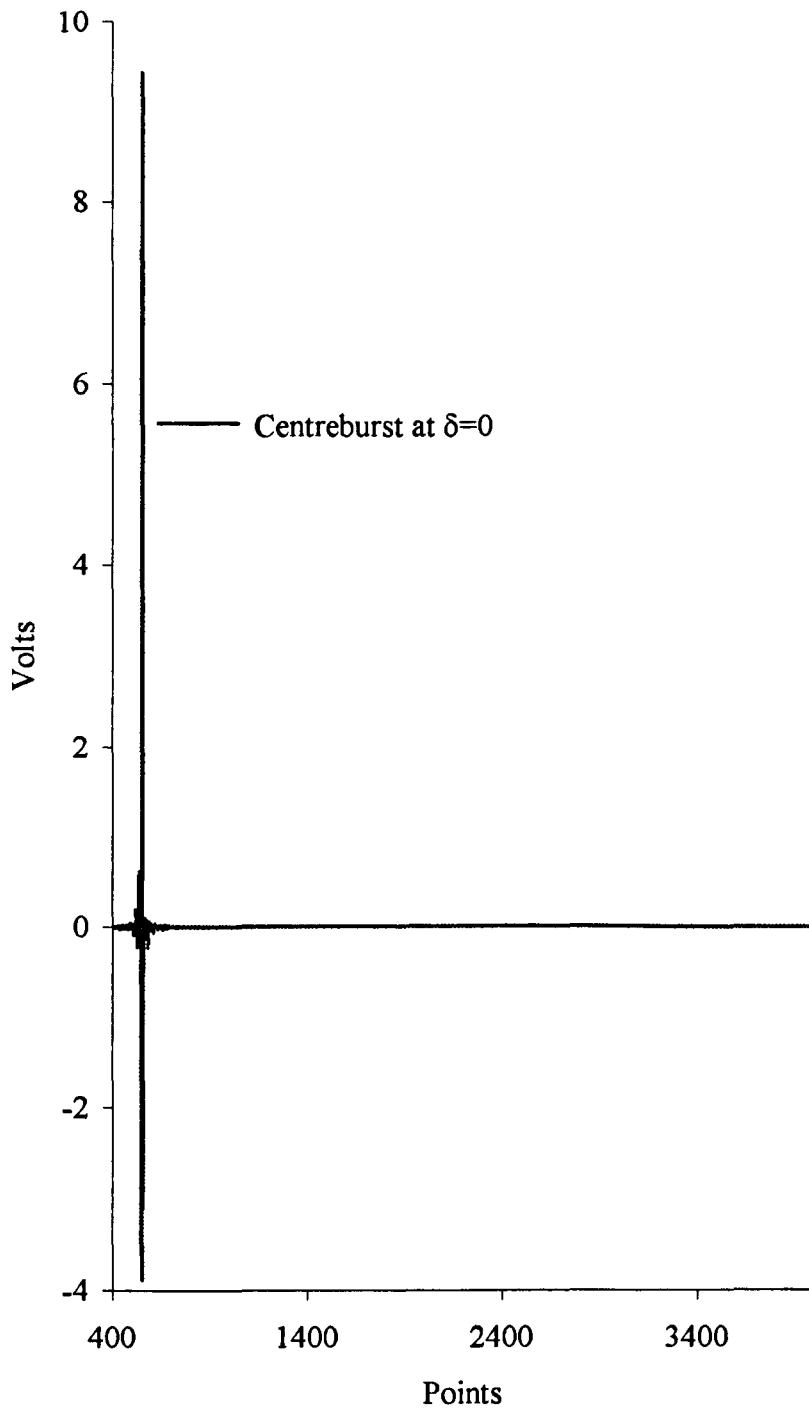
$$I(\delta) = \int_0^{\infty} B(\bar{\nu}) \cos(2\pi\delta\bar{\nu}) .d\bar{\nu} \quad \text{Equation 2.3}$$

which is one half of a cosine Fourier transform pair, the other being, Equation 2.4

$$B(\nu) = \int_{-\infty}^{+\infty} I(\delta) \cos(2\pi\nu\delta) .d\delta \quad \text{Equation 2.4}$$

Fig. 2.11 displays the result of this interferogram. It consists of an intense centreburst at zero retardation which then decays rapidly with increasing δ .

Figure 2.11 A typical interferogram



Since $I(\delta)$ is an even function, the equation can be written, Equation 2.5.

$$B(\nu) = 2 \int_0^{\infty} I(\delta) \cos(2\pi\nu\delta) . d\delta \quad \text{Equation 2.5}$$

In practice the interferogram is measured over a finite retardation which results in finite resolution. A typical single beam spectrum is shown in fig 2.12. The transmittance spectrum is obtained by ratioing the single beam spectrum of the sample to a background single beam spectrum.

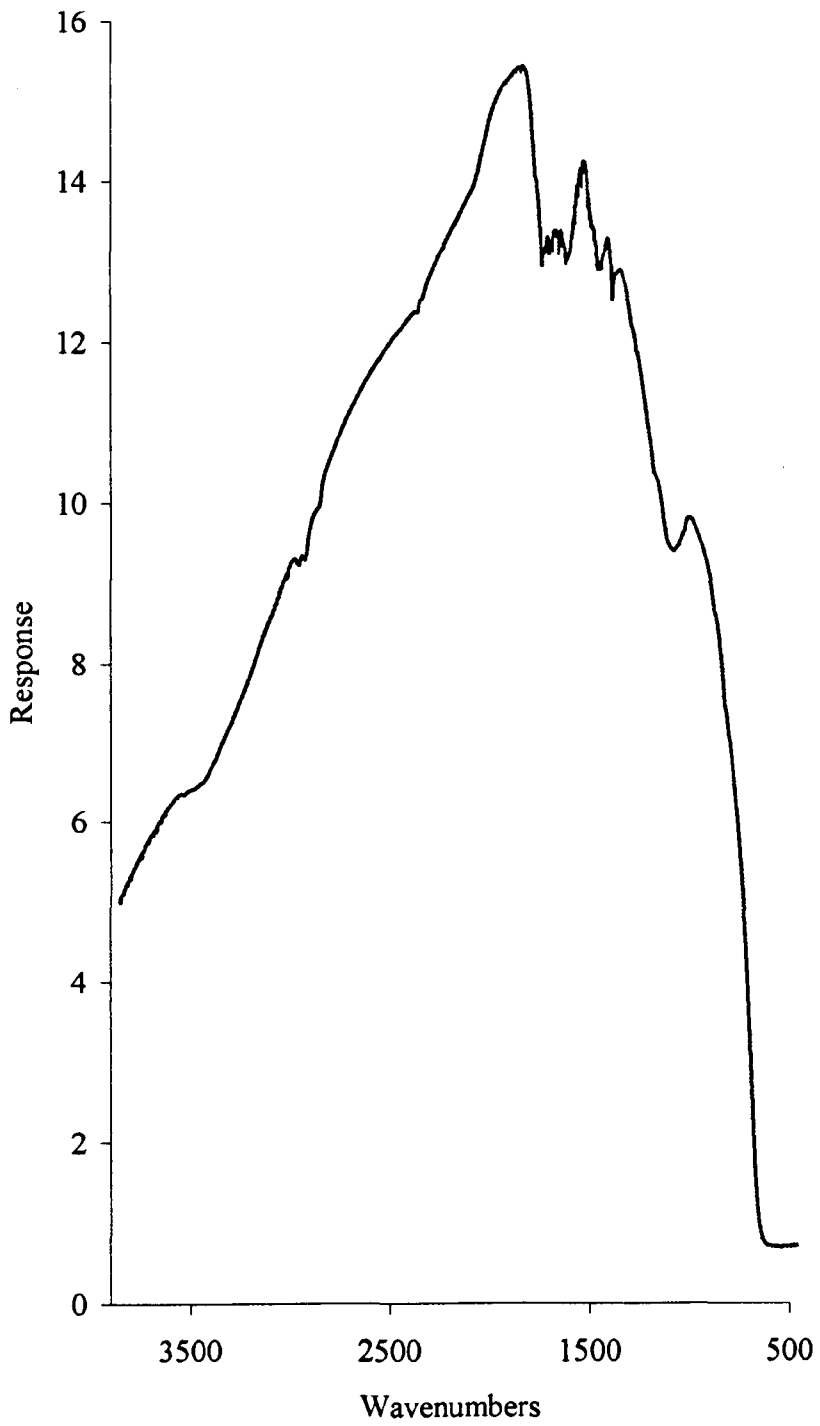
2.4.2 Resolution

Consider the case of a spectrum consisting of a doublet of equal intensity separated by $\Delta\bar{\nu}$ ($\bar{\nu}_1 - \bar{\nu}_2$). The two cosine waves are out of phase after a retardation of $0.5 (\Delta\bar{\nu})^{-1}$. Therefore the resolution depends on the maximum retardation of the interferometer. The two waves can be resolved when the two waves become in phase for the first time after zero retardation. This is when, Equation 2.6.

$$\delta = (\Delta\bar{\nu})^{-1} \quad \text{Equation 2.6}$$

Thus if the maximum retardation of an interferometer is δ_{\max} then the best resolution that can be obtained is given by Equation 2.7.

Figure 2.12 A typical single beam spectrum



$$\Delta \bar{\nu} = 1/\delta_{\max} \quad \text{Equation 2.7}$$

In practice this means that greater retardations i.e. greater mirror travel will produce higher resolution information in the wings of the interferogram and there will be a limit to how far the movable mirror can be displaced.

2.4.3 Apodisation

If retardation values from $-\Delta$ cm to $+\Delta$ cm are set, the complete interferogram is multiplied by a boxcar function. That is for all values of δ greater than Δ and less than $-\Delta$ it is set to 0 and 1 for all other values. The effect on the lineshape is to produce negative and positive side lobes to peaks in the spectrum. To avoid losing information for the frequencies corresponding to the minima, the negative side lobes can be removed by substituting a triangular apodisation function, Figures 2.13 and 2.14. The interferogram is set equal to 0 for values of $\delta > \Delta$ and $\delta = -\Delta$. Between $-\Delta$ and $+\Delta$ the interferogram is multiplied by a linear function which has the value of 0 at $-\Delta$ and $+\Delta$ and a value of 1.0 at $\delta = 0$. The resolution is slightly lowered by using this function, but information is retained. The mid-IR and far-IR experiments used triangular apodisation in the measurements taken.

Figure 2.13 The Effect of Boxcar Truncation on Lineshape

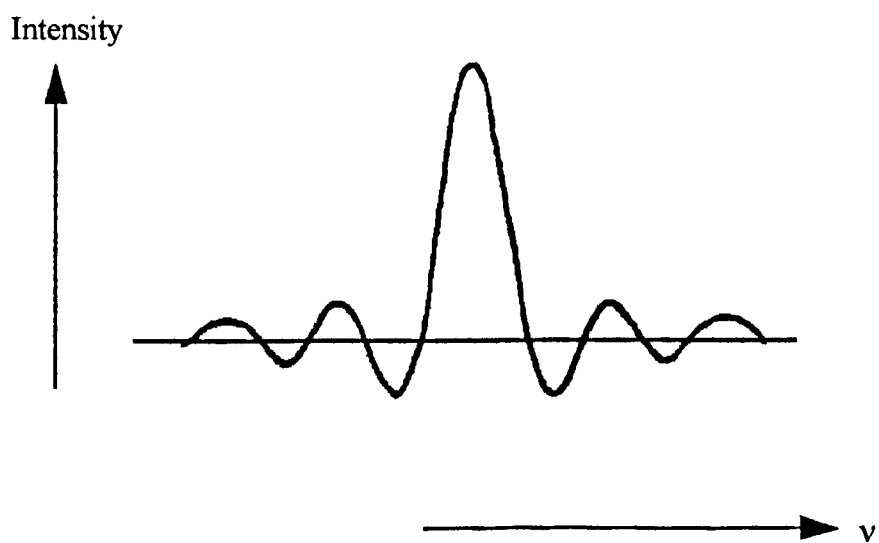
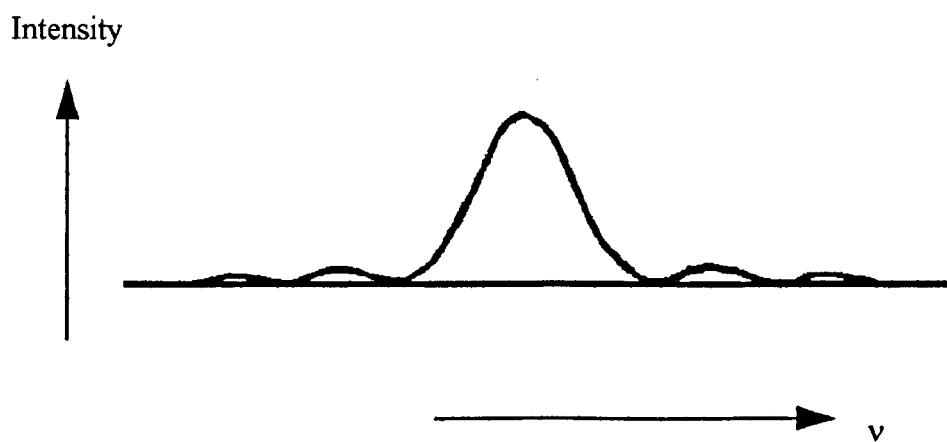


Figure 2.14 The Effect of Triangular Truncation on Lineshape



2.4.4 Advantages of FTIR

The most significant advantage is the higher signal-to-noise ratio of the FTIR system. Fellgett [12] showed that since the interferogram sees all of the wavelengths present all of the time during the scan, (as opposed to one resolution element), the magnitude of the signal-to-noise advantage is equal to the square root of the number of resolution elements in the wavenumber range that is being scanned. Equation 2.8.

$$\text{Fellgett's advantage} = \sqrt{(\bar{\nu}_1 - \bar{\nu}_2) / \Delta\bar{\nu}} \quad \text{Equation 2.8}$$

where $\bar{\nu}_1$ is the highest wavenumber in the region of interest, $\bar{\nu}_2$ is the lowest wavenumber and $\Delta\bar{\nu}$ is the resolution.

In practice scanning a region from 4000 to 400 cm^{-1} at a resolution of 4 cm^{-1} results in an advantage factor of 30.

The Jacquinot advantage states that a greater throughput of energy can be achieved. The energy throughput, or *étendue*, is the conserved product of image size and beam divergence. This is of less importance than the Fellgett advantage and in many applications *étendue* is limited by the sample size.

Connes advantage is the ability to accurately sample the interferogram resulting in an accurate spectrum. This requires that the data points are taken at very precise equal intervals of retardation. To achieve this a monochromatic helium-neon laser of wavelength 632.8 nm generates

a reference interferogram, the interferogram corresponding to a single frequency source is a cosine function and the zero crossings of this interferogram can be used to trigger the collection of the data point sampled from the infrared interferogram. A high wavenumber accuracy is achieved.

2.5 Reflection Absorption Infrared Spectroscopy (RAIRS)

2.5.1 Physical Principles

Francis and Ellison [19] were the first to recognize that the absorption of infrared radiation by thin films at a metal surface is increased by reflecting the incident light at grazing angles of incidence and is effectively limited to p-polarized light, the component of the radiation whose electric vector lies parallel to the plane of incidence.

Greenler [20] calculated the angular dependence of the resultant amplitude of the electric field produced by radiation at a bare metal surface and deduced that the sensitivity of the technique depends upon the polarization of the incident radiation, the angle of incidence and the number of reflections. Pritchard and Sims [21] confirmed these findings experimentally. A qualitative description of the prominent aspects of the theoretical calculation is described below.

Infrared radiation can be resolved into components whose electric vectors lie perpendicular and parallel to the plane of incidence, respectively

s and p-polarization, see fig 2.15. The consequences of the differing phase and amplitude changes upon reflection at a metal surface for these components is illustrated in fig. 2.16. At all angles of incidence the s-polarized component undergoes a phase shift of close to 180° , fig. 2.16.a. The fractional reflection coefficient is near unity and the resultant of the incident and reflected vectors is close to zero at the surface. The interaction between electric dipoles of an adsorbate and s-polarized light is negligible as the electric field parallel is effectively zero.

The p-component undergoes a phase change that varies strongly with the angle of incidence. The resultant electric field vector at the surface can be resolved into components perpendicular, $E_{p\perp}$, and parallel, $E_{p\parallel}$, to the metal surface. Those vectors are dependent on the fractional reflection coefficient and the phase change on reflection in addition to the angle of incidence. The phase change for p-polarised light at the surface is small over a wide range of angles. Hence, the incident and reflected normal components reinforce each other. This is illustrated in fig. 2.16.b. The resultant normal electric field increases with θ as shown in fig. 2.17 as there is an increasing normal component of the light and the field approaches twice the vacuum field strength at high angles of incidence before falling effectively to zero at $\theta = 90^\circ$ as the phase change tends to 180° . the resultant parallel electric field strength remains low as the incident and reflected components lie in opposite directions.

Therefore s-polarised light gives rise to a negligible electric field at the surface and p-polarised light generates a significant electric field normal

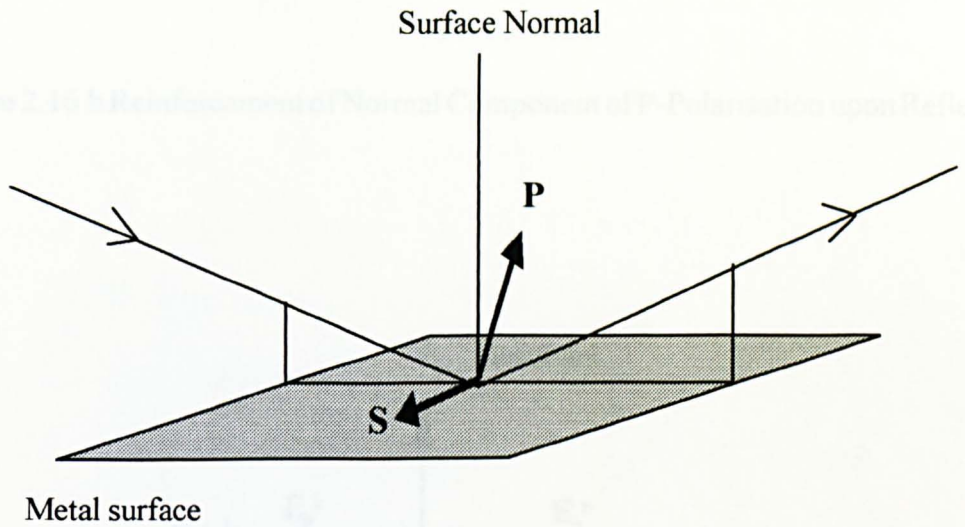


Figure 2.15 Diagram Showing S and P Polarisations

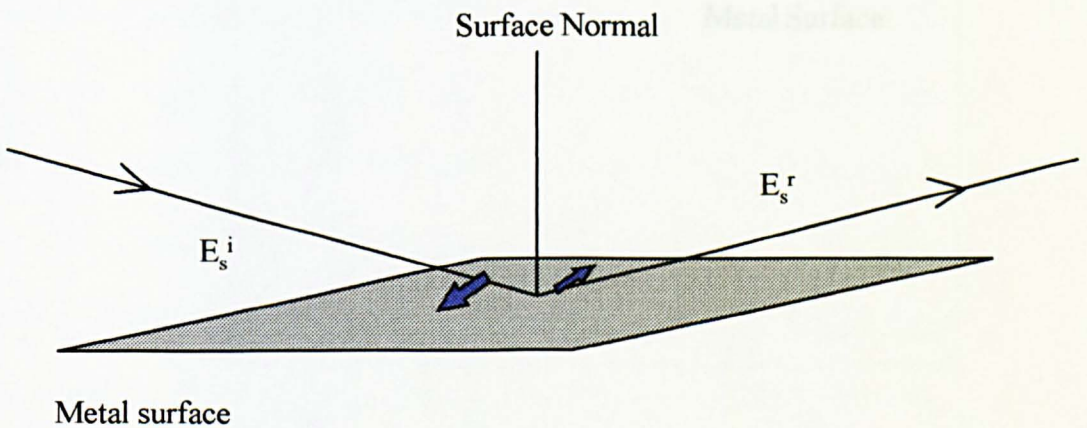


Figure 2.16.a Diagram showing the 180° Phase Change for S Polarisation upon Reflection

Figure 2.16.b Reinforcement of Normal Component of P-Polarisation upon Reflection

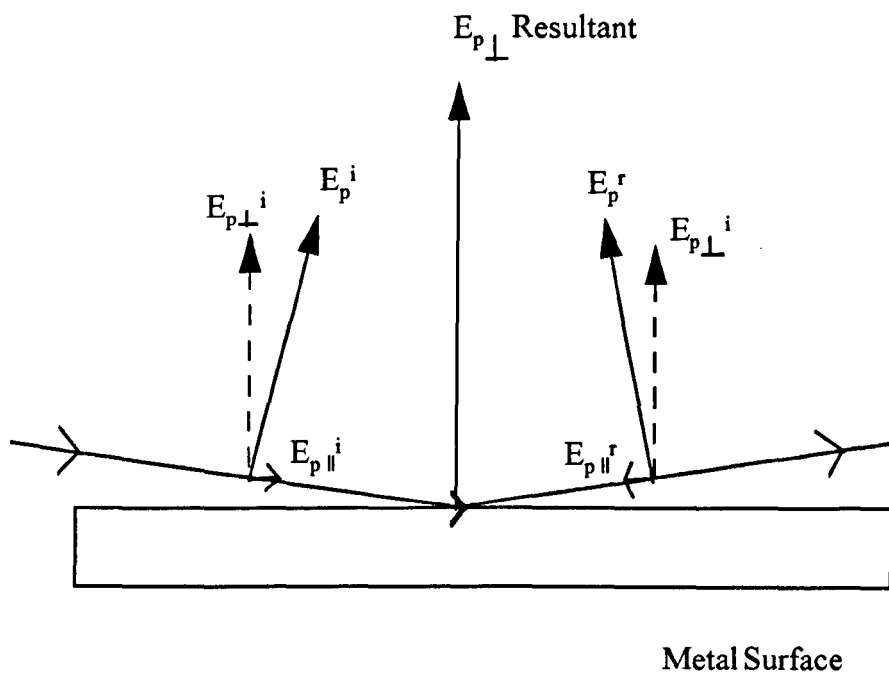
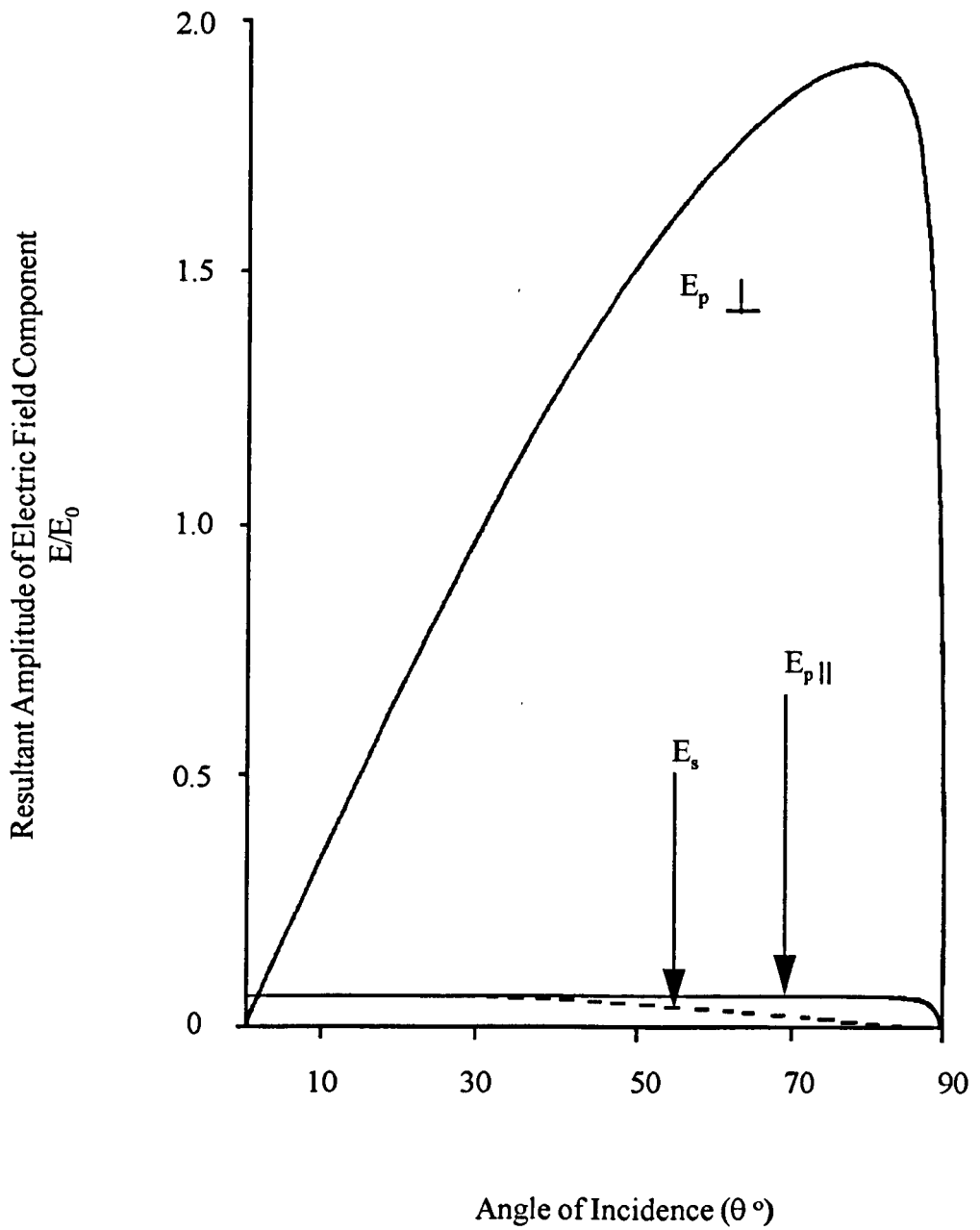


Figure 2.17 The Resultant Amplitudes of the Components of the Electric Field Generated at a Metal Surface due to Radiation (of Amplitude E_0) Incident at an Angle θ

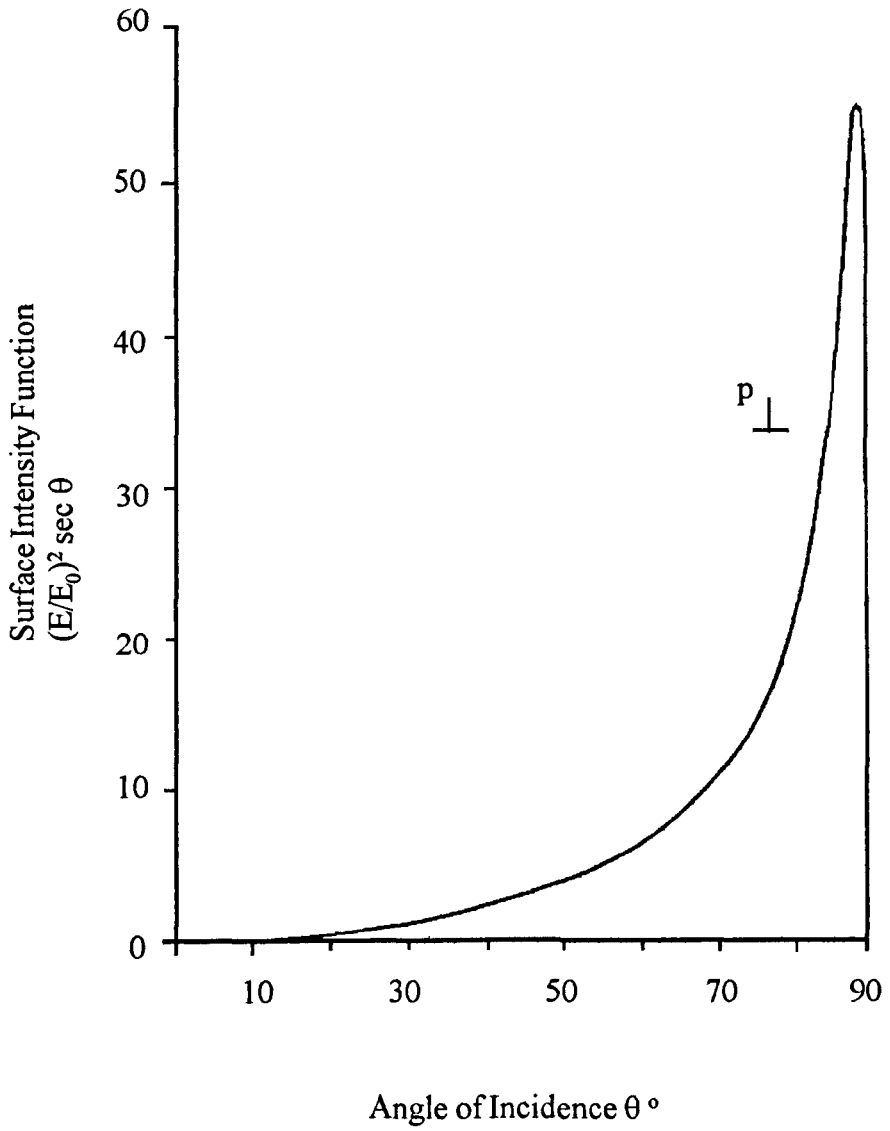


to the surface. Thus the metallic surface imposes a strict selection rule which states that 'only vibrational modes with a component of the dynamic dipole moment oriented perpendicular to the surface will interact with the electric field generated by the infrared radiation'. This phenomenon is known as the 'metal surface selection rule' [22].

Together with the general selection rule for electric dipole transitions a more rigorous symmetry requirement is imposed. A group theoretical treatment of the symmetry requirements effectively means that only the totally symmetric vibrational modes of the adsorbate-surface complex can be observed with RAIRS.

The previous discussion has focused on the reflection of infrared radiation from a bare metal surface. Theoretical considerations of the influence of an adsorbed layer on the surface and the intensity of the absorption bands associated with this layer were first calculated by Greenler [20]. The effect of the adsorbed layer on the optical properties of the reflecting surface was taken into account; resulting in the amplitude reflectivity of the system. More simply the absorption intensity can be considered as proportional to the square of the amplitude of the electric field and the number of absorbing species. Since $E_{p||}$ is small and the pathlength of the radiation through the adsorbed layer varies as $1/\cos\theta$, the parameter known as 'the surface intensity function', can be written as $(E_{p\perp}/E_0)^2/\cos\theta$ and shows the strong sensitivity of the experiment to the incident angle θ , fig. 2.18. As predicted by the accurate absorption

Figure 2.18 The Variation Of the Absorption Intensity Function with θ



function deduced by Greenler, the amplitude of this 'surface intensity function' peaks sharply at high angles of incidence.

Above it was shown that the surface intensity function was dependent on the number of absorbing species at the surface. Greenler considered theoretically if it would be advantageous to increase the number of absorbers interacting with the infrared radiation by a multiple reflection. At the grazing angle of incidence, the reflectivity of the metal goes through a minimum and after reflection there is a loss in the total intensity. An increasing number of reflections reduces this total intensity further. Therefore there is an optimum number of reflections that produces the greatest reflectivity change on absorption. This is dependent on the metal and the angle of incidence. However a multiple reflection experiment increases the complexity of the optical set-up and since with a single reflection experiment, 60-80% of the maximum signal intensity is possible, the single reflection RAIRS experiment is usually preferred.

A high signal-to-noise is required for RAIRS experiments, this results from the optical requirement of focusing light onto a small single crystal at grazing angles of incidence in the UHV chamber. The étendue that results is typically $10^{-1} \text{ mm}^2 \text{ sr}$, one to two orders lower energy throughput than a FTIR spectrometer. A comfortable sample size for a bulk infrared experiment is *ca.* 10^{20-21} molecules. This compares with 10^{15} molecules in a monolayer for a RAIRS experiment. When these two conditions are considered together it is necessary for a high signal-to-noise

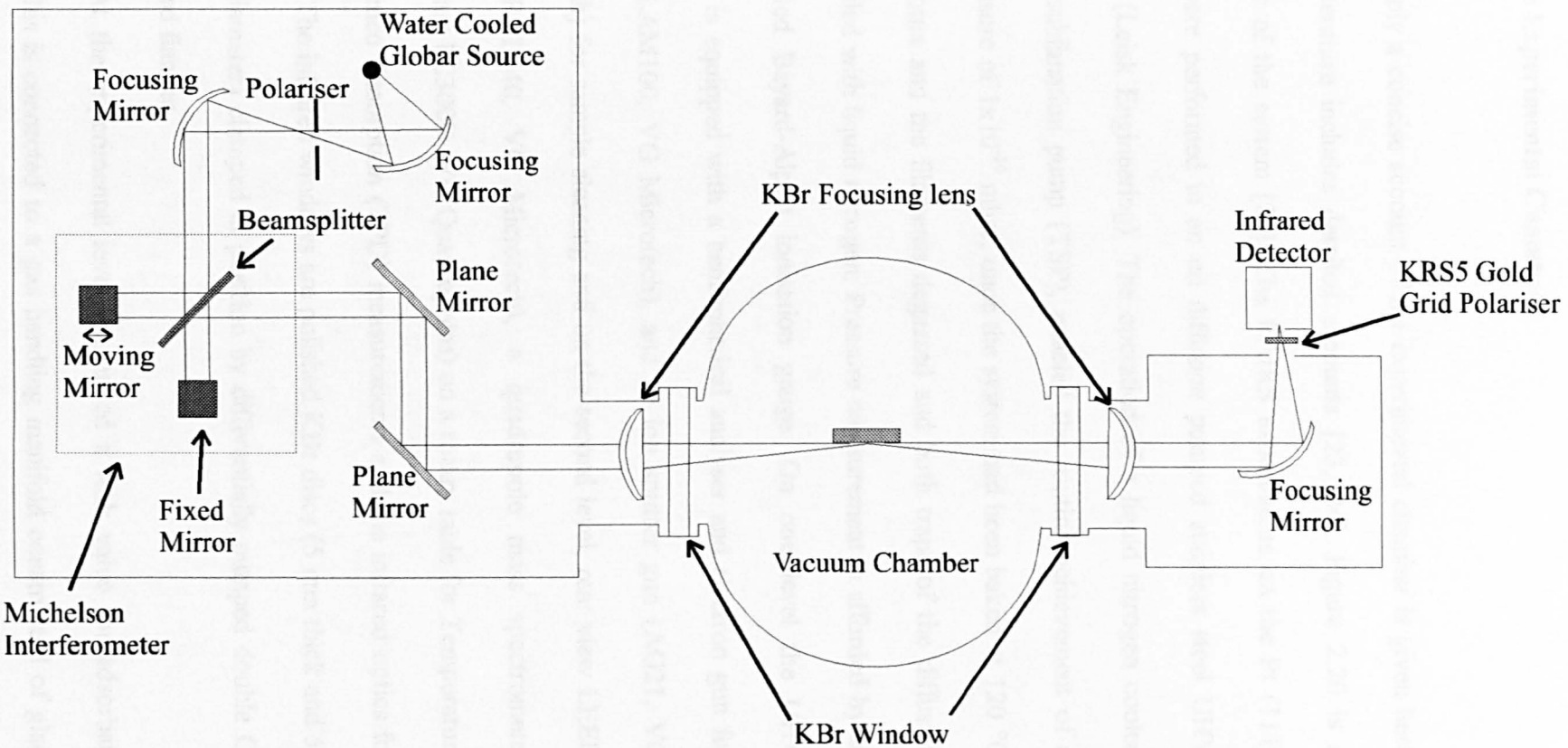
level to be achieved, for example a weak absorber with an absorption band less than 0.1% requires a S/N of 10^4 (0.01% peak-to-peak noise).

2.6 The Ultra-high Vacuum System

2.6.1 Instrumentation

RAIR spectra in the trifluoropropene experiments were recorded using a BIO-RAD FTS-60A/ 896 FTIR spectrometer. The collimated IR beam from the interferometer is reflected from a plane mirror out of the spectrometer and focused through a KBr window onto a platinum single crystal sample in a stainless steel vacuum chamber, fig. 2.19. The angle of incidence is estimated to be $85 \pm 5^\circ$ to the surface normal. The reflected beam exits the vacuum chamber *via* a second KBr window into the collection optics. It is passed through a polariser ensuring that only p-polarised radiation reaches the detector window. A narrow band mercury cadmium telluride (MCT) detector is used to record spectra in the range $4000\text{-}800\text{ cm}^{-1}$. The spectrometer and the manifolds containing the optical components were purged with dry CO_2 -free air from a commercial air dryer. This helps to limit the intensity of the background atmospheric absorption bands of H_2O and CO_2 , whose presence would obscure weak absorption bands of the adsorbate of interest if the frequencies were similar.

Figure 2.19 A Schematic Diagram of the Optical Configuration of the RAIRS system

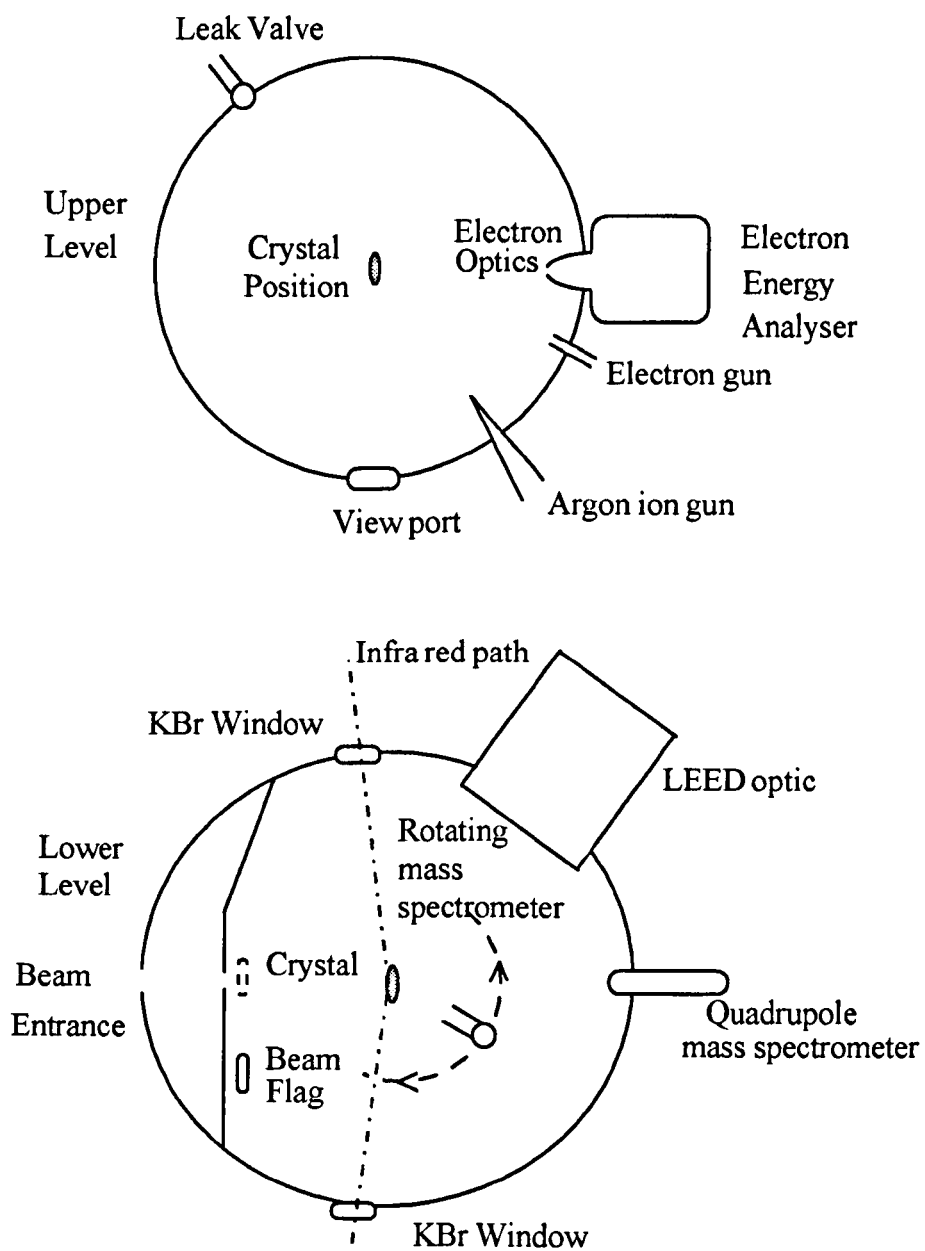


2.6.2 The Experimental Chamber

Only a concise account of the experimental chamber is given here as the literature includes detailed accounts [23, 24]. Figure 2.20 is a schematic of the system [25]. The RAIRS experiments on the Pt (111) crystal were performed in an oil diffusion pumped stainless steel UHV chamber (Leisk Engineering). The operation of a liquid nitrogen cooled titanium sublimation pump (TSP), enabled the routine achievement of a base pressure of 1×10^{-10} mbar; once the system had been baked at 120 °C for 48 hours and the filaments degassed and both traps of the diffusion pumps filled with liquid nitrogen. Pressure measurement is afforded by an uncorrected Bayard-Alpert ionisation gauge. On one level the UHV chamber is equipped with a hemispherical analyser and electron gun for AES (CLAM100, VG Microtech), and an ion sputter gun (AG21, VG Microtech) for sample cleaning and on the second level, rear view LEED optics (RVL640, VG Microtech), a quadrupole mass spectrometer (Micromass PC300D, VG Quadrupoles) on a rotary table for Temperature Programmed Desorption (TPD) measurements and the infrared optics for RAIRS. The infrared windows are polished KBr discs (5 mm thick and 50 mm in diameter) clamped in position by differentially pumped double O-ring sealed flanges.

At the experimental level is situated a leak valve for adsorbate gases. This is connected to a gas handling manifold constructed of glass and stainless steel. The line is pumped to a pressure of 1×10^{-7} by a 2" oil

Figure 2.20 A Schematic Diagram of the Chamber Used for the RAIRS Experiments



diffusion pump backed by a rotary pump. The glass part of the manifold can be isolated and is used to handle the vapours of liquid samples or gaseous samples stored in glass bulbs connected *via* glass connectors. The stainless steel part is used to handle the gaseous samples or sample preparation gases which are stored in pressure cans and are attached *via* appropriate gauges to the gas line.

2.6.3 Crystal Mounting

The Pt (111) single crystal was mounted on a XYZ θ manipulator manufactured by Leisk Engineering (fig. 2.21) [25]. A differentially pumped O-ring seal is fitted at the top of the manipulator assembly. At the top of the differentially pumped rotary drive is a stainless steel re-entrant tube which is connected at its base to a copper stud which is held in place by a grub screw. The crystal was attached to the copper stud by an electrically insulating but thermally conducting copper-sapphire-copper sandwich. The bottom of the sandwich consisted of two copper semi-circles to each half a 1 mm tungsten rod was soldered in position. The platinum crystal was mounted on the tungsten rods as shown in fig. 2.22 [25]. Three 0.38 mm diameter tungsten wires were pushed through holes either side of the crystal. The three heating wires were spot welded onto nickel foil tabs located on the rods. the chromel-alumel thermocouple was positioned in a small hole in the top of the crystal and secured in place by ceramic glue (Aremco 617). Short copper heating braids were attached on

Figure 2.21 A Schematic Diagram of the Sample Manipulator used in the RAIRS Experiments [25]

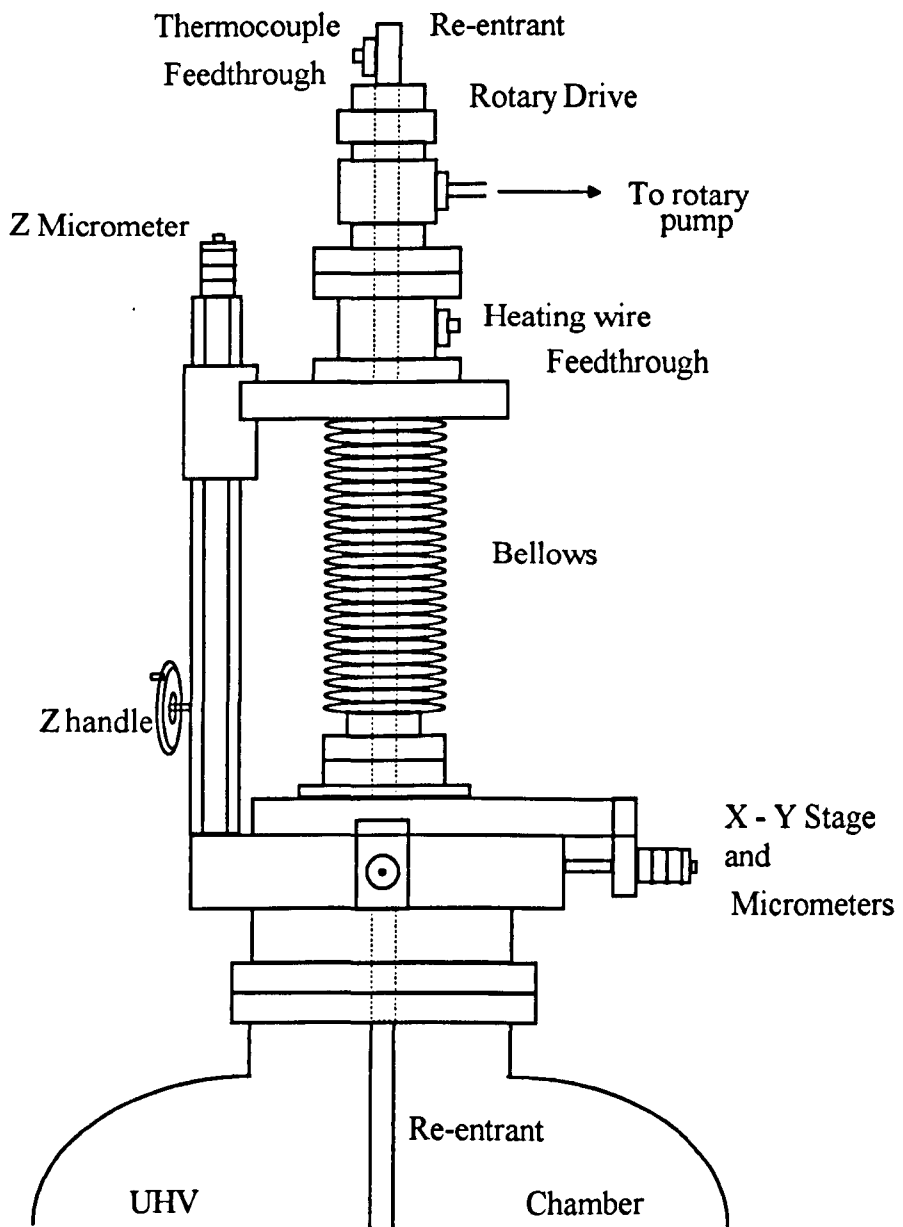
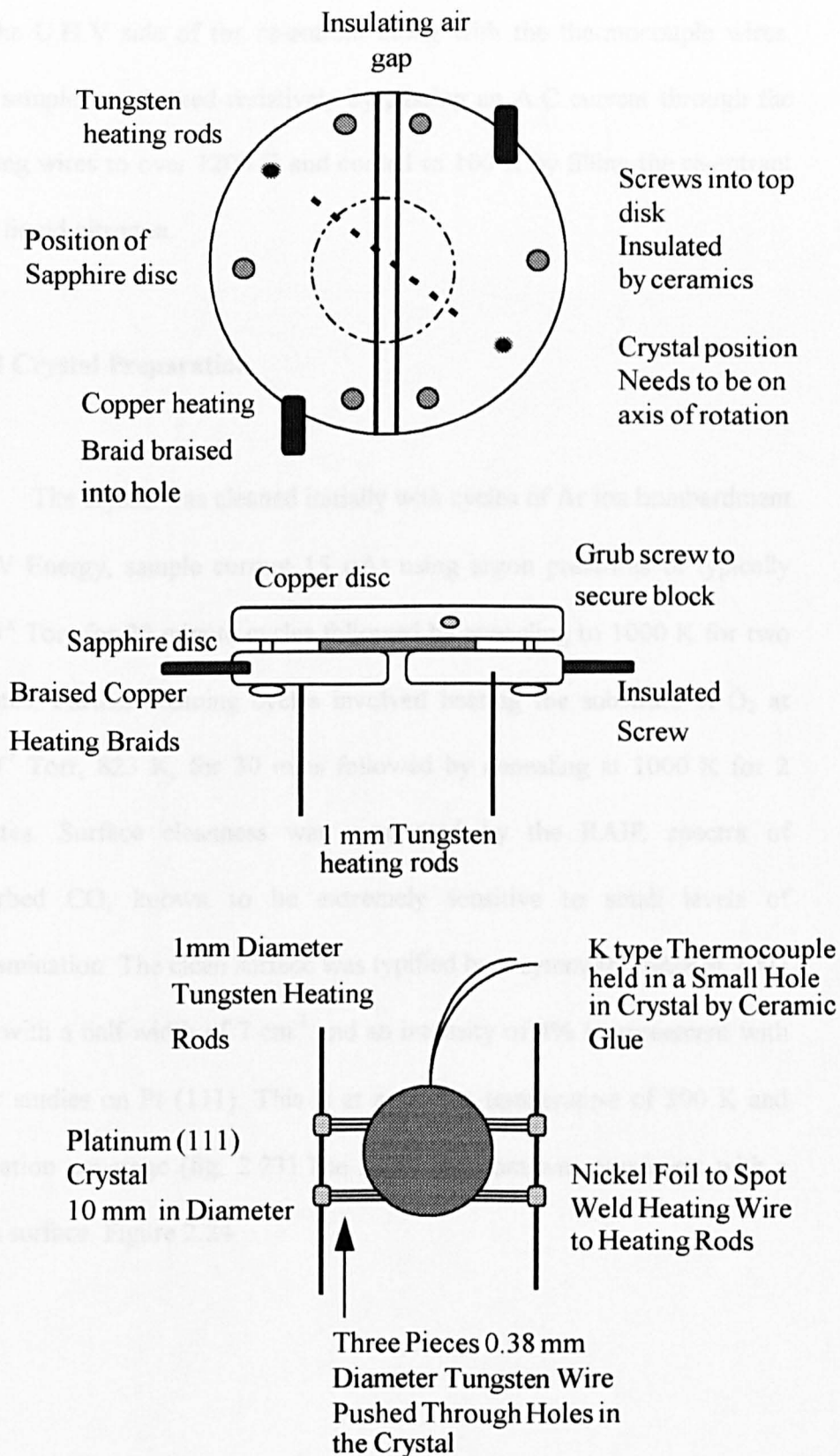


Figure 2.22 The Details of the Sample Mount used for the RAIRS Experiments [25]



either side by a barrel connector to the tungsten rods which in turn connect the heating wires to the top of the manipulator. The heating wires passed up the U.H.V side of the re-entrant along with the thermocouple wires. The sample was heated resistively by passing an A.C current through the heating wires to over 1200 K and cooled to 100 K by filling the re-entrant with liquid nitrogen.

2.6.4 Crystal Preparation

The crystal was cleaned initially with cycles of Ar ion bombardment (4 kV Energy, sample current 15 μA) using argon pressures of typically 2×10^{-6} Torr for 20 minute cycles followed by annealing to 1000 K for two minutes. Further cleaning cycles involved heating the substrate in O_2 at 5×10^{-7} Torr, 823 K, for 30 mins followed by annealing at 1000 K for 2 minutes. Surface cleanness was monitored by the RAIR spectra of adsorbed CO, known to be extremely sensitive to small levels of contamination. The clean surface was typified by a symmetric peak at 2097 cm^{-1} with a half-width of 7 cm^{-1} and an intensity of 4% in agreement with other studies on Pt (111). This is at a sample temperature of 300 K and saturation coverage (fig. 2.23). The AES spectrum was consistent with a clean surface. Figure 2.24.

Figure 2.23 The RAIR spectrum of 5 L CO on clean Pt (111) at 300 K

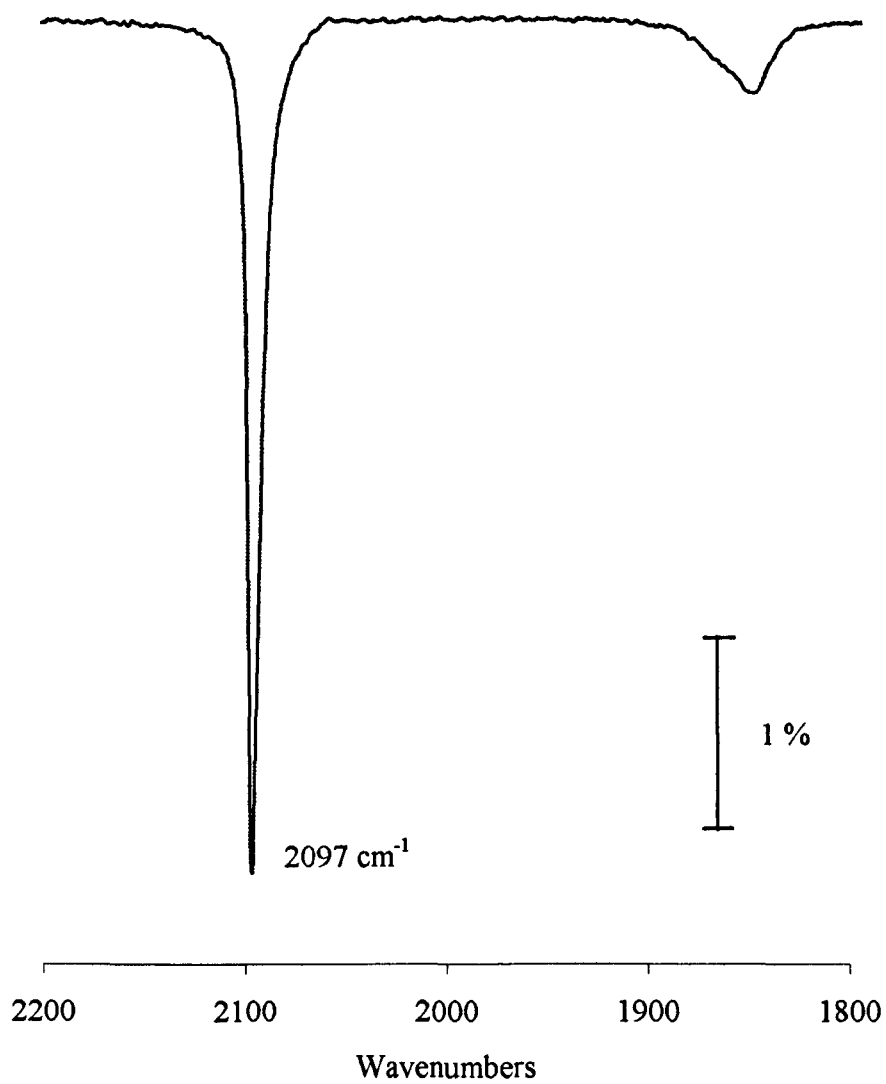
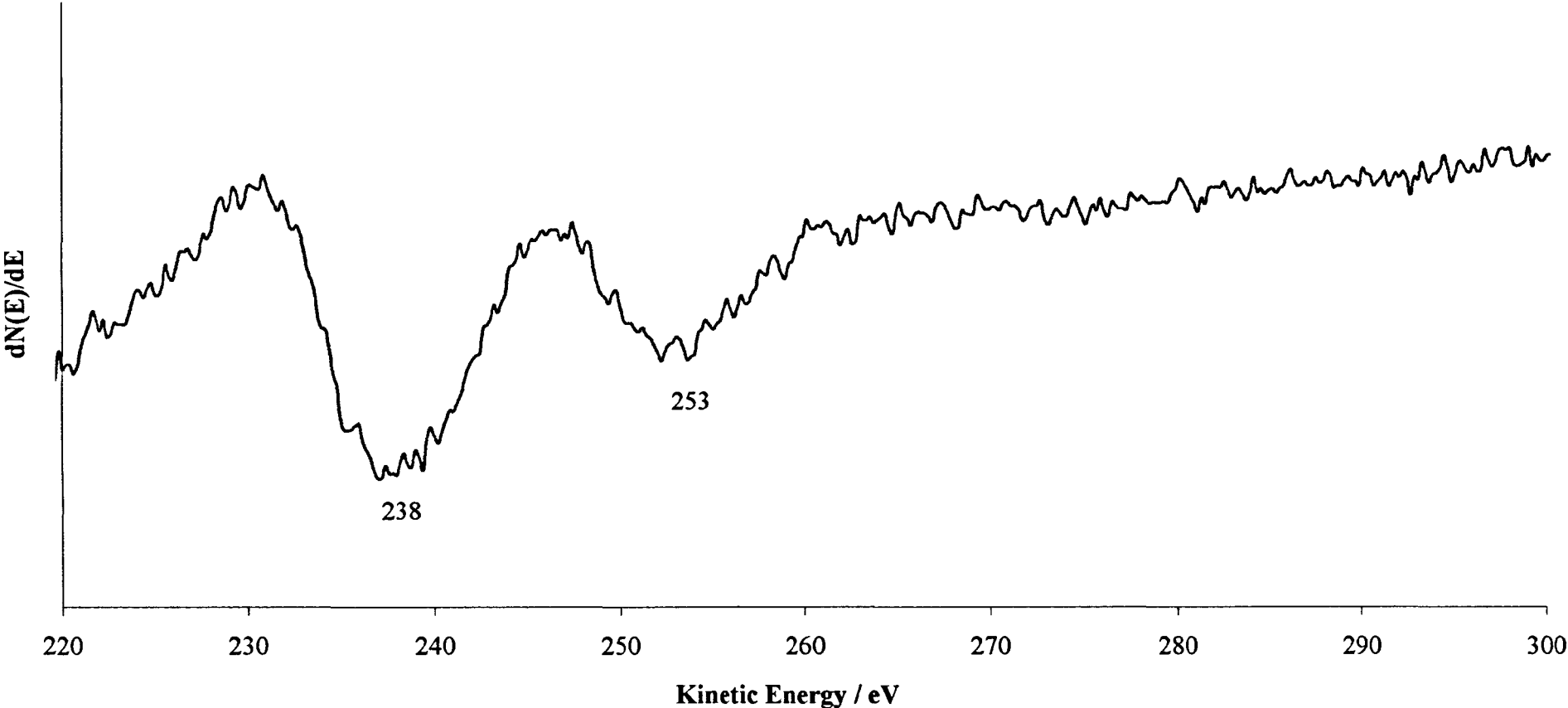


Figure 2.24 The AES Spectrum of the Clean Pt (111) Surface



2.6.5 Gas Sample Preparation

Sample dosing was achieved by backfilling the vacuum chamber. All exposures are based on uncorrected ion gauge readings and are expressed in Langmuirs. 3,3,3-Trifluoropropene was supplied by Fluorochem Ltd. and was stored in an air tight glass bulb sealed with Youngs' greaseless taps. The purity was checked by mass spectrometry and the gas was used without further purification.

2.6.6 Recording Spectra

Following the cycle of oxygen treatment and annealing at 1000 K for 2 minutes, the crystal was cooled rapidly to approximately 350 K by flushing the re-entrant tube with nitrogen gas. This minimized the CO pick-up from the background. As an extra precaution the crystal was flashed to 473 K at least twice to desorb any CO that had contaminated the crystal. Then the temperature was held constant at approximately 350 K whilst the background spectrum was recorded. In the case of CO-RAIRS, 256 clean background scans at a resolution of 2 cm^{-1} were recorded. The adsorbate was dosed into the vacuum chamber through the leak valve. Once the crystal had received the desired dose, the adsorbate gas was pumped away (until a pressure of below 1×10^{-9} mbar was achieved), and the single beam spectrum of the crystal surface with the adsorbed layer (sample spectra) was recorded. Transmittance spectra were obtained from the ratio of 256

sample scans to 256 clean background scans at 2cm^{-1} . From the CO peak position as mentioned before the cleanness of the sample was assessed. Once clean, the CO was flashed off as before and the background was recorded at the desired temperature for those experiments that were above room temperature. The sample dosing was then achieved by the description above. If a cold background was desired the sample was cooled first and then the CO was flashed off before re-cooling to record the cold background. This minimizes further CO contamination. The spectra were obtained as a ratio of 1024 sample scans to 1024 clean background scans at a resolution of 4 cm^{-1} , or 256 sample scans to 256 clean background scans at a resolution of 2 cm^{-1} . Further sample spectra, either as a function of exposure or temperature were recorded in the same manner as above.

Part B (ii) The Far-Infrared Apparatus

2.7 Introduction: The Synchrotron Radiation Source

A Synchrotron accelerates charged particles, such as electrons, to speeds close to that of light. A series of magnets is used to bend the path of the electrons along a curved path. As the electrons pass these 'bending magnets', intense beams of light are emitted as the path of the electrons is deflected. This is known as synchrotron radiation [26].

The Synchrotron Radiation Source (SRS) at Daresbury was the world's first machine dedicated to the production and use of synchrotron

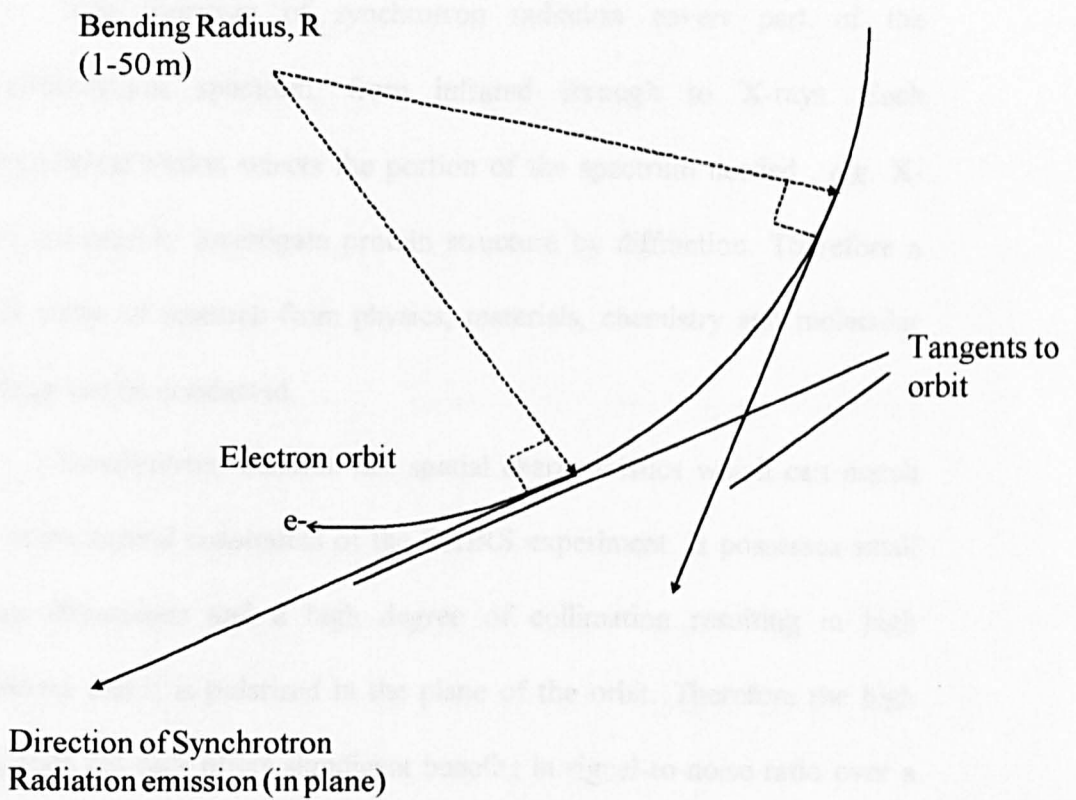
radiation. The facility consists of three main parts: a linear accelerator (an “electron gun”), a booster synchrotron and a storage ring. Electrons are fired from the linear accelerator into the booster synchrotron, where they are accelerated to almost the speed of light before being injected into a storage ring. Here they travel in a vacuum inside a tube around the 96 m circumference of the ring producing synchrotron radiation.

The magnetic field of the storage ring is produced by sixteen huge ‘dipole’ electromagnets which constrain the beam to a roughly circular path. Synchrotron light is produced at each of the 16 bending magnets and 3 special magnets known as ‘insertion devices’. The light appears like a searchlight in front of the emitting particle so it appears at a tangent to the bend, see fig 2.25. The type of light produced at sources like the SRS depend on both the energy of the electron beam and the magnetic fields used to bend the beam. The higher the beam energy, the shorter the wavelength of the light produced. Strong magnetic fields will also bend the beam more sharply thus increasing the acceleration which also gives shorter wavelength light.

To replace the energy lost in emitting synchrotron light the electrons orbit in a series of bunches pulsed along with radio-frequency waves fed into the electron beam in four places as the beam travels along the SRS, in this way synchrotron light is emitted continuously for many hours.

The Daresbury SRS has two principal modes of operation; multibunch and single bunch modes. This is indicative of the number of

Figure 2.25 A Schematic Diagram of Synchrotron Radiation Emission



electron bunches in circulation around the ring. For the RAIRS experiment, single bunch is not applicable due to the small ring current and therefore radiation intensity available. The Daresbury SRS is about 30 metres in diameter with a bending radius of 5.56 m. It has an electron energy of 2 GeV and a typical ring current following injection of around 250 mA in multibunch mode with a lifetime of about 30 hours (time taken for the current to fall to 1/e of its original value).

The spectrum of synchrotron radiation covers part of the electromagnetic spectrum, from infrared through to X-rays. Each experimental station selects the portion of the spectrum needed, *e.g.* X-rays are used to investigate protein structure by diffraction. Therefore a wide range of research from physics, materials, chemistry and molecular biology can be conducted.

Synchrotron radiation has spatial characteristics which can match the experimental constraints of the RAIRS experiment. It possesses small beam dimensions and a high degree of collimation resulting in high brilliance and it is polarised in the plane of the orbit. Therefore the high brilliance not only offers significant benefits in signal-to-noise ratio over a black body source but is ideal for use in experiments where the étendue (conserved product of image size and beam divergence) is restricted. Thus for the requirements of RAIRS where the étendue is inherently low (due to the use of small single crystals and the optical requirement of a grazing angle of incidence), synchrotron radiation can be advantageous. This idea is discussed further in Chapter 4.

2.8 The Ultra-high Vacuum System

2.8.1 Beamline 13.3

A diagram of the experimental station , 13.3, is shown in figure 2.26. The synchrotron radiation light produced at the SR source in the storage ring is carried by a series of optics through a high vacuum beam line, maintained by ion pumps, to the experimental area. The optics designed for the transportation of the radiation are reported in the literature [27].

Radiation from a line of tangent points along the optical axis is intercepted first by a plane mirror, M1, and the horizontal infrared beam is deflected vertically. In the vertical direction the beam height at M1 varies from 78 mm at 20 cm^{-1} to just 16 mm at 3000 cm^{-1} . The mirror is placed at 1.08 m from the tangent point, fig 2.27. the beam then travels 3.25 m through concrete shielding to a mirror, M2, which is an ellipsoidal mirror designed to focus an image of the effective point source at the diamond exit window. Design implications are discussed below.

To cope with the enormous heat loading of the bright light source which results from the close proximity of M1 to the beam orbit, the mirror is a plane reflector of gold coated copper equipped with a cooled thermal shield,fig. 2.28. The shield absorbs the highly collimated and energetic X-ray beam and consists of a continuous length of copper tubing of O.D 3/8" with a cooling water flow rate of 24 litres/second. The mirror itself is

Figure 2.26 Beamline 13.3

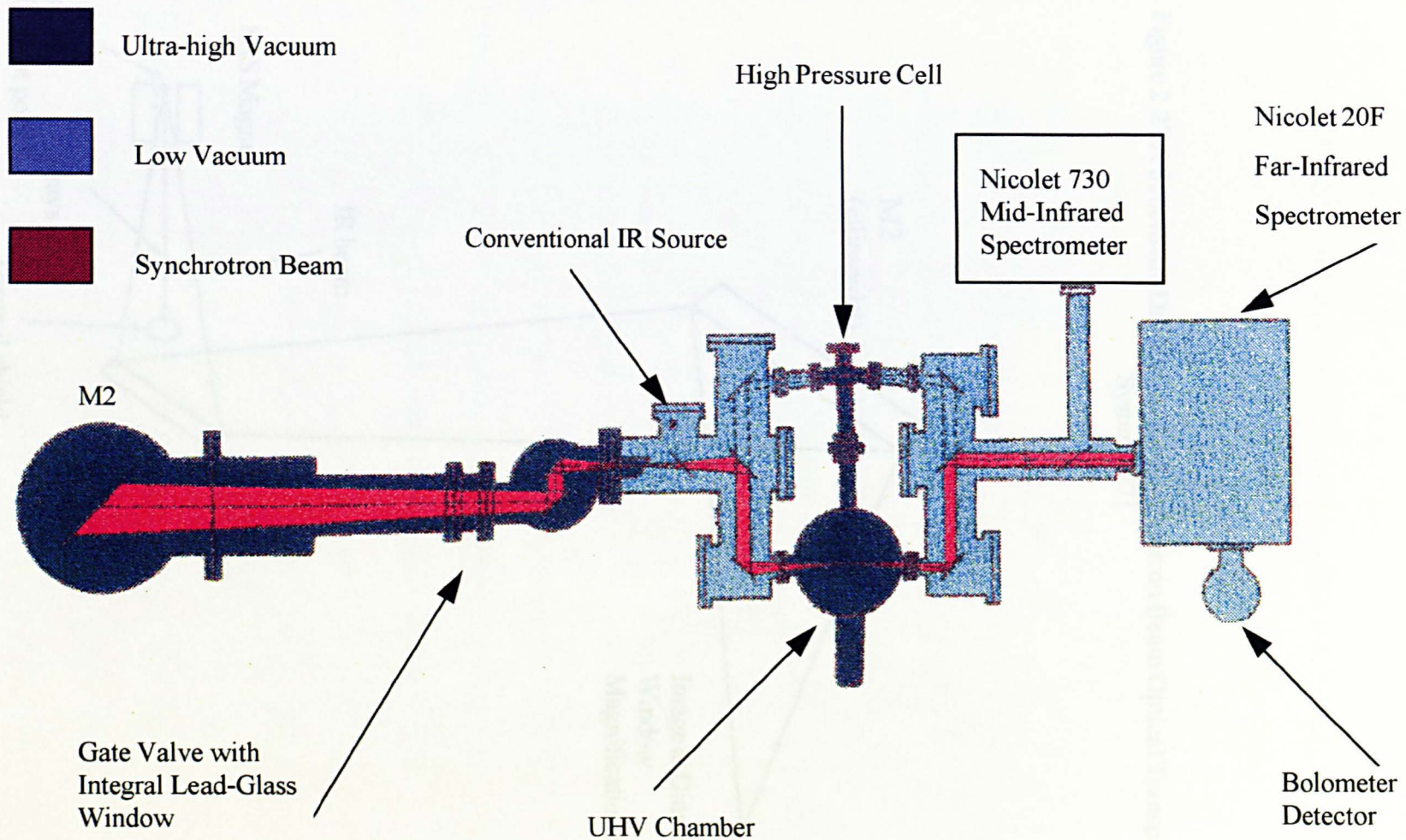


Figure 2.27 A Schematic Diagram of the Synchrotron Beam Optical Transport System [27]

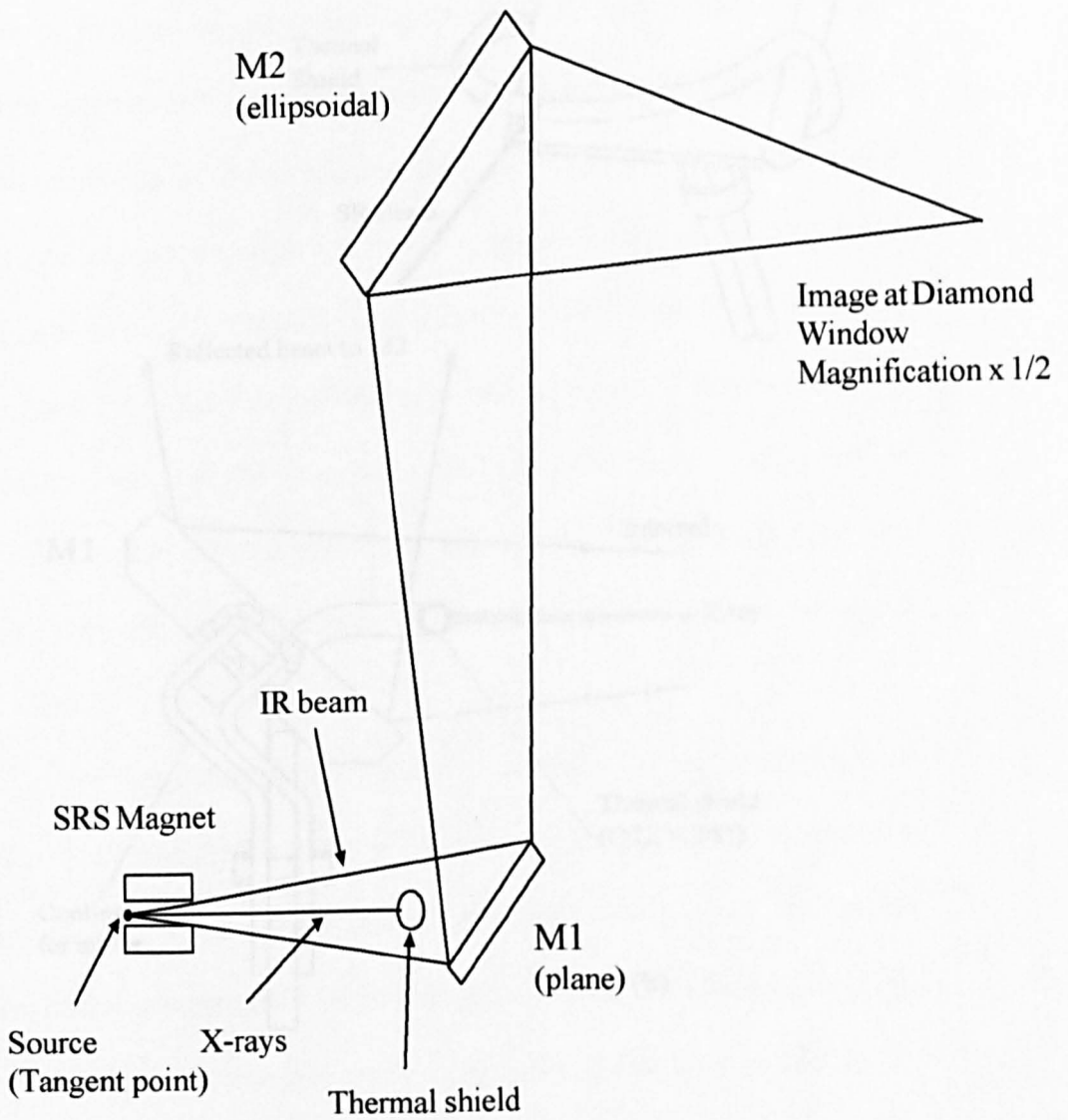
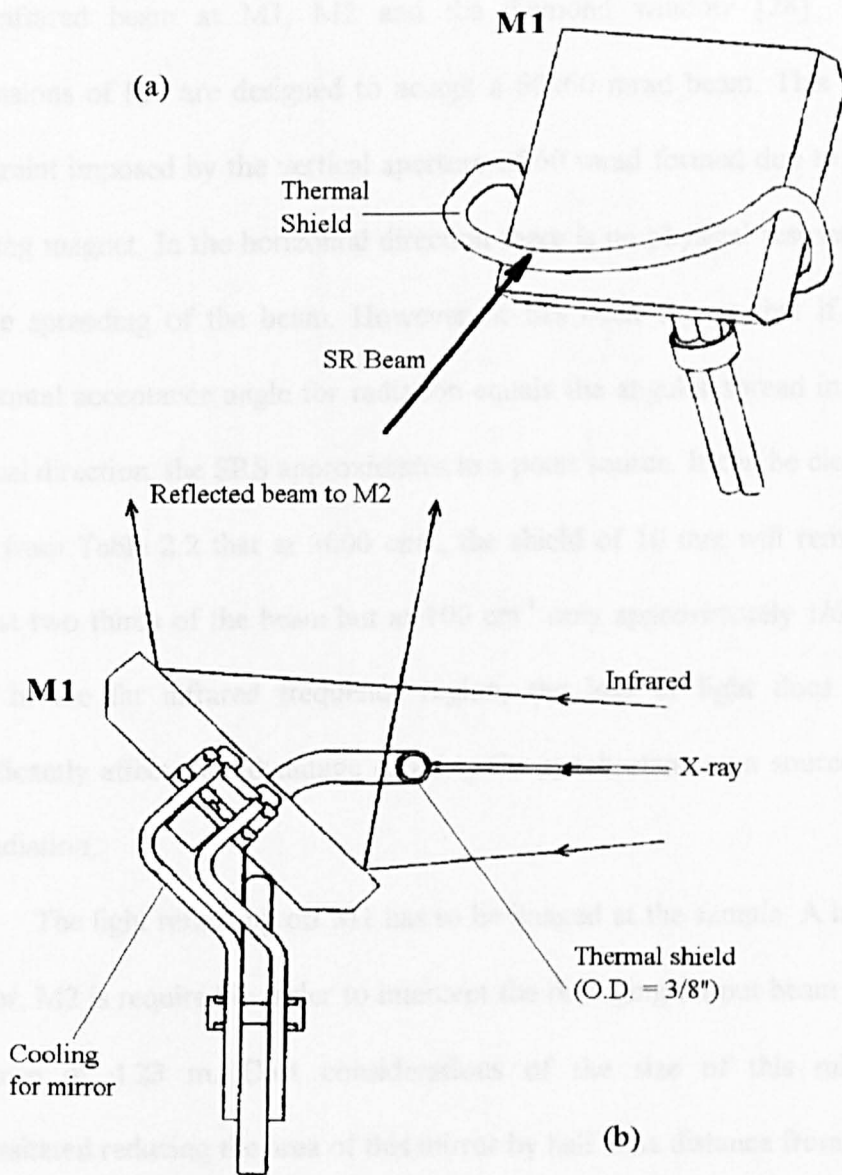


Figure 2.28 Diagram of Mirror M1 and the Thermal Shield Viewed from a) the Front and b) the Side



water-cooled to withstand the effects of low energy light or scattered light from the shield falling on it. The size of the X-ray beam is of the order of a millimetre and the thermal shield is nearly 10 mm. This allows for movement of the beam but unfortunately the dimension is too large to avoid losing some of the infra-red light. Table 2.2 gives the dimensions of the infrared beam at M1, M2 and the diamond window [28]. The dimensions of M1 are designed to accept a 60x60 mrad beam. This is a constraint imposed by the vertical aperture of 60 mrad formed due to the bending magnet. In the horizontal direction there is no physical restriction to the spreading of the beam. However, it has been shown that if the horizontal acceptance angle for radiation equals the angular spread in the vertical direction, the SRS approximates to a point source. It can be clearly seen from Table 2.2 that at 3000 cm^{-1} , the shield of 10 mm will remove almost two thirds of the beam but at 100 cm^{-1} only approximately $1/6^{\text{th}}$ is lost. In the far infrared frequency region, the loss of light does not significantly affect the advantage of using the synchrotron as a source of IR radiation.

The light reflecting off M1 has to be imaged at the sample. A large mirror, M2 is required in order to intercept the diverging output beam at a distance of 4.23 m. Cost considerations of the size of this mirror necessitated reducing the area of this mirror by half. The distance from M2 to the exit window *via* two small plane steering windows is 2.00 m. An image diameter of one half that of the source is produced [27].

Table 2.2 Calculated Beam Widths in the Horizontal and Vertical Planes at Key Points in the Optical Train [28]. (Allowance has not been made for the finite size of the electron beam: this results in an underestimate of the image size for wavenumbers above 100 cm^{-1}).

Wave-number $/\text{cm}^{-1}$	Beam width/mm						Convergence angle/mrad	
	M1		M2		Window		Window	
	H	V	H	V	H	V	H	V
20	65	78	255	305	5.1	4.2	130	152
50	65	74	255	290	2.0	1.8	130	145
100	65	58	255	227	1.0	1.1	130	116
300	65	41	255	161	0.33	0.58	130	82
1000	65	27	255	106	0.10	0.16	130	54
3000	65	16	255	75	0.03	0.11	130	38

The requirements of the exit window are strict. It is responsible for the isolation of the storage ring vacuum. Therefore it must be transparent to infrared, UHV compatible and free of absorption bands in the spectral region of interest. Diamond fulfills all these requirements. The diamond window measures 14x7x0.25 mm yielding a free aperture of 5x5 mm when mounted at the Brewster angle. This is to avoid both reflection losses and interference fringes resulting in background structure. The diamond is mounted in a molybdenum plate in turn welded to a re-entrant steel tube at the Brewster angle. The diamond window can be isolated by a gate valve positioned before the two plane steering mirrors.

2.8.2 Infrared Optics and Instrumentation

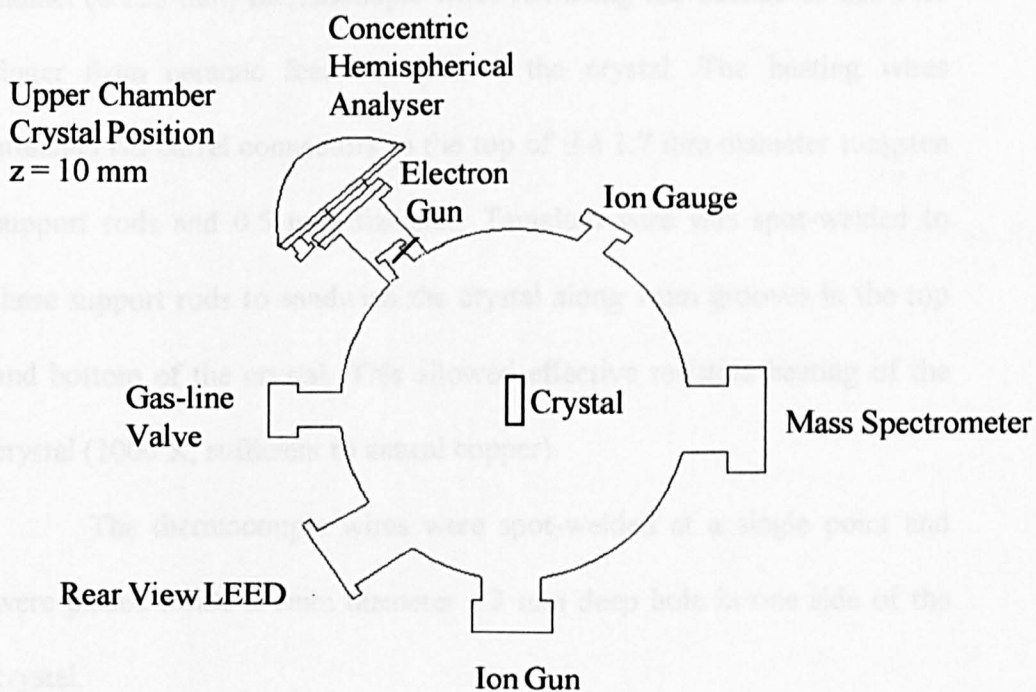
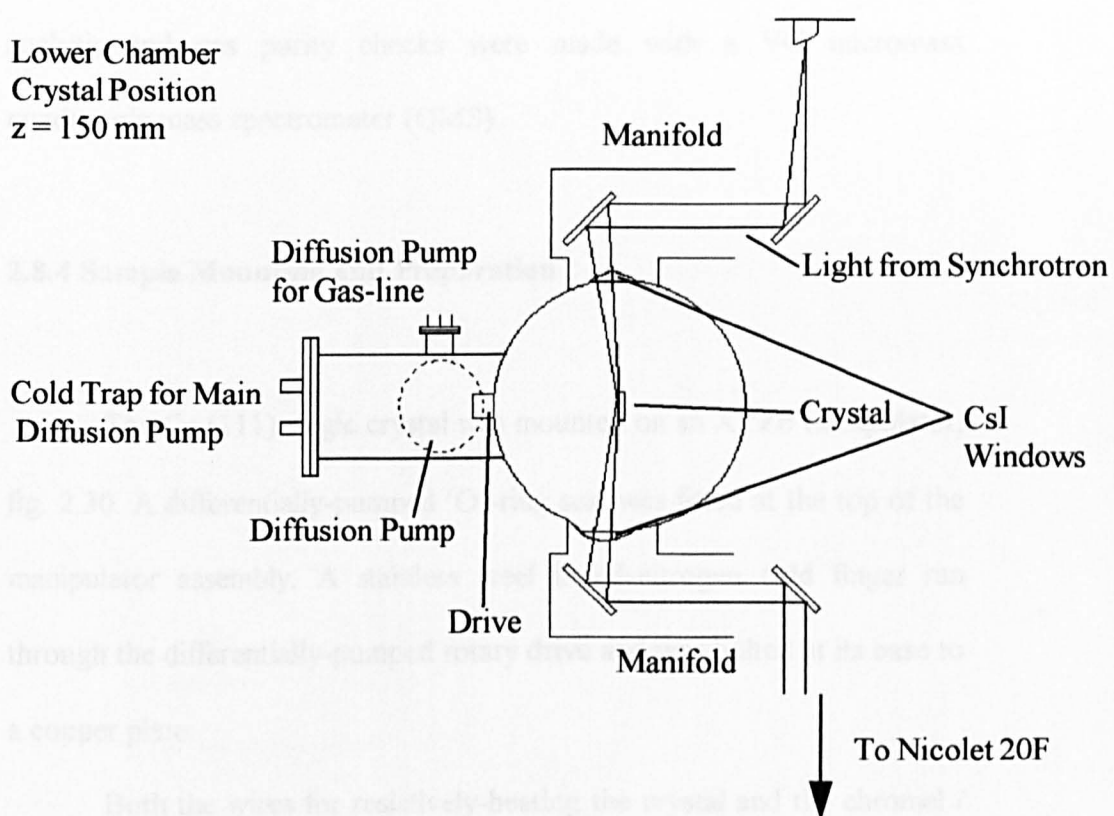
After exiting the storage ring vacuum *via* the diamond window the beam is collimated by small off axis parabolic mirrors and refocused through differentially pumped CsI windows (cut off $\sim 200\text{ cm}^{-1}$) for reflection from the single crystal sample. The incident angle is 87° . The plane of polarization of the radiation lies parallel to the plane of incidence. The image at the crystal is a 1:1 magnification of the diamond window image. The manifold which contains the optics is held at a pressure of $<10^{-1}$ mbar by a rotary pump, to minimise atmospheric absorption particularly by water vapour. Upon exiting the experimental chamber again through CsI windows, the beam is recollimated by a second optics manifold and directed into a Nicolet 20F spectrometer. This is a dedicated

far infrared Fourier transform spectrometer, which is equipped with a (Solid Substrate TM) beamsplitter and liquid helium cooled germanium bolometer (QMC Instruments Ltd). Inside the 20F the beam is modulated by the Michelson interferometer and then focused at the sample compartment, with an image magnification of ½ from the sample focus in the UHV RAIRS chamber, and secondly at the bolometer. The beam passes through a low-pass filter of 500 cm⁻¹. This is composed of a mixture of alkali-halide materials baked into a polypropylene substrate. The beam is then intercepted by a gold plated copper parabolic Winston cone collector before it finally reaches the germanium element bolometer [29]. Synchrotron radiation is polarised in the plane of the source, hence a polariser was not required in these experiments.

2.8.3 The Experimental Chamber

The UHV experimental chamber used for conducting the far-IR RAIRS experiments on beamline 13.3 is shown schematically in fig. 2.29. The chamber consists of a diffusion pumped main chamber with a liquid nitrogen cooled cold trap. A titanium sublimation pump (TSP) provides additional pumping. After bakeout at 120 °C for 48 hours, upon cooling, degassing all the filaments and filling the traps, a typical base pressure of 2x10⁻¹⁰ mbar was achieved. The chamber is split into two levels, the lower one contains the optical axis and the CsI windows and the upper level is equipped with Omicron rear view LEED, A VSW HA100 concentric

Figure 2.29 A Schematic Diagram of the UHV Chamber on Beamline 13.3



hemispherical analyser and EG5 gun for Auger electron spectroscopy and a PHI electronics noble gas ion sputter gun was used for sample cleaning. Pressures were measured with a Bayard-Alpert ion gauge and residual gas analysis and gas purity checks were made with a VG micromass quadrupole mass spectrometer (QMS).

2.8.4 Sample Mounting and Preparation

The Cu (111) single crystal was mounted on an XYZ θ manipulator, fig. 2.30. A differentially-pumped 'O'-ring seal was fitted at the top of the manipulator assembly. A stainless steel liquid-nitrogen cold finger ran through the differentially-pumped rotary drive and was bolted at its base to a copper plate.

Both the wires for resistively-heating the crystal and the chromel / alumel (0.125 mm) thermocouple wires ran along the outside of this cold finger from ceramic feed-throughs to the crystal. The heating wires attached *via* barrel connectors to the top of the 1.7 mm diameter tungsten support rods and 0.5 mm diameter. Tantalum wire was spot-welded to these support rods to sandwich the crystal along 1mm grooves in the top and bottom of the crystal. This allowed effective resistive heating of the crystal (1000 K, sufficient to anneal copper).

The thermocouple wires were spot-welded at a single point and were placed inside a 1mm diameter / 3 mm deep hole in one side of the crystal.

Figure 2.30 A Schematic Diagram of the Cu (111) Sample Mount

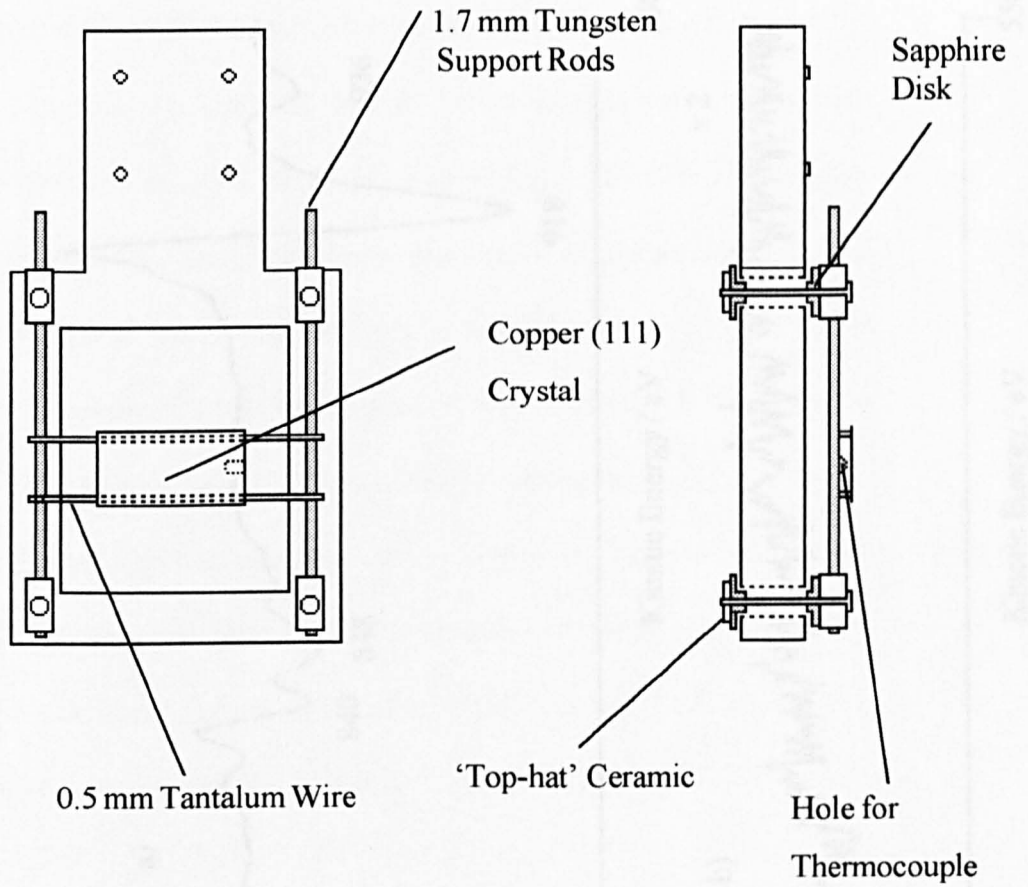
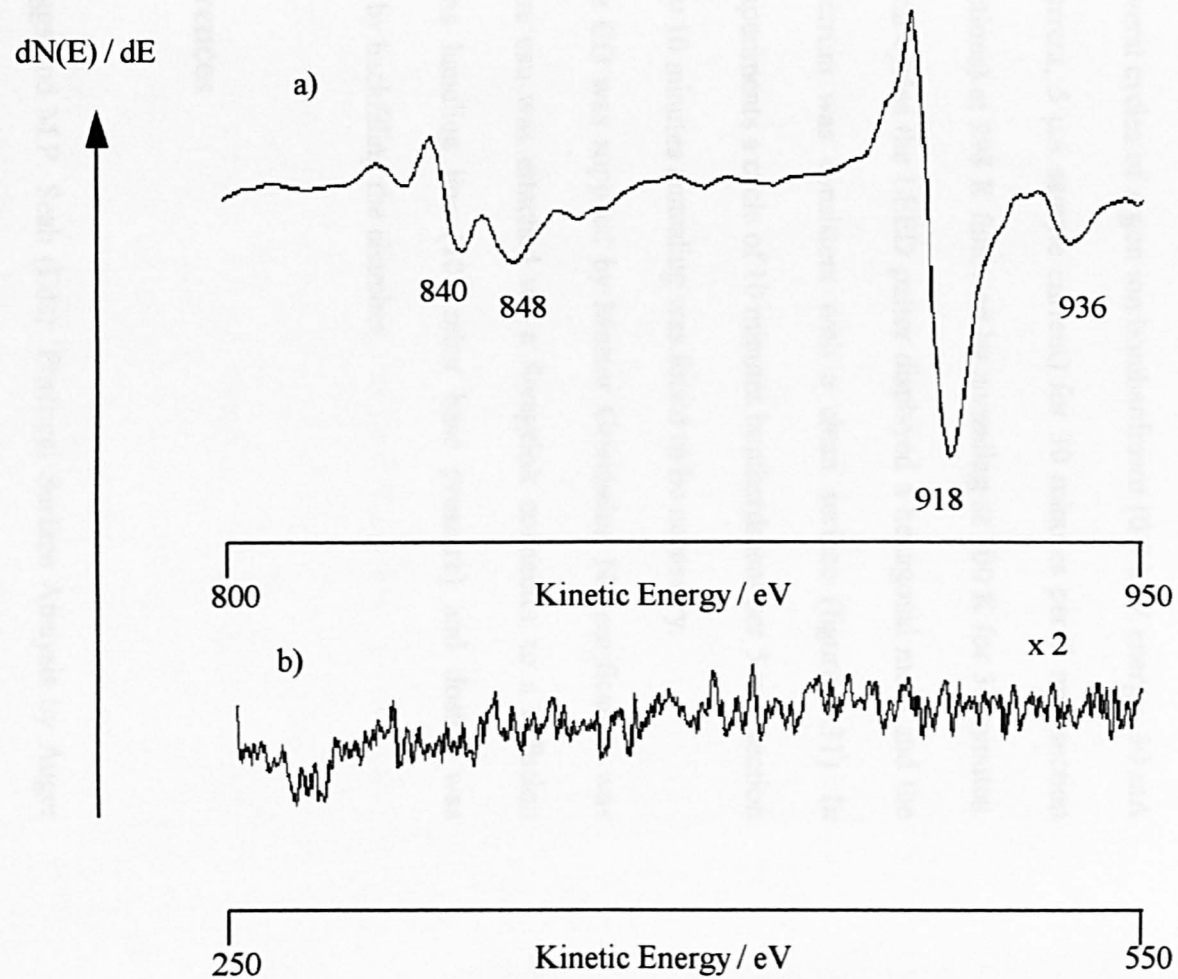


Figure 2.31 The AES Spectrum of the Clean Cu (111) Surface in the Region
a) 800 - 950 eV and b) 250-550 eV



The support rods were electrically-isolated from the copper frame by means of a sapphire disk and “top-hat” ceramic (as shown in fig. 2.30). This allowed thermal contact for cooling the crystal. The cooling system gave a temperature of approximately 120 K.

The crystal was chemically etched in a mixture of glacial acetic acid, orthophosphoric acid and concentrated nitric acid in a 1:1:1 ratio prior to several cycles of argon ion bombardment (0.5 keV energy, 30 mA filament current, 5 μ A sample current) for 30 minutes per 5 mm section (total 4 sections) at 298 K followed by annealing at 700 K for 30 minutes. After several cycles the LEED pattern displayed a hexagonal mesh and the Auger spectrum was consistent with a clean surface (figure 2.31). In between experiments a cycle of 10 minutes bombardment per 5 mm section followed by 10 minutes annealing was found to be necessary.

The CO was supplied by Messer Griesheim. No purification was needed. The can was attached *via* a Swagelok connector to a diffusion pumped gas handling line (10^{-5} mbar base pressure) and dosing was performed by backfilling the chamber.

2.9 References

- [1] D. Briggs and M.P. Seah (Eds) ‘Practical Surface Analysis by Auger and X-ray Photoelectron Spectroscopy’, (Wiley, New York 1983)
- [2] L.J. Clarke, Surface Crystallography: ‘An Introduction to Electron Diffraction’, (Wiley, 1985)

- [3] J.B. Hudson, *Surface Science: An Introduction* (Butterworth and Heinemann) 1992
- [4] D.P. Woodruff and T.A. Delchar, 'Modern Techniques of Surface Science', Second Edition, (Cambridge University Press, 1994)
- [5] *Surface Analysis - 'The Principle Techniques'*, Ed. J.C. Vickerman. (Wiley 1997)
- [6] Neville V. Richardson, 'Electrons to Stimulate vibrations' article in *Chemistry in Britain* 29 (1993) 41
- [7] H. Ibach and D.L. Mills, 'Electron Energy Loss Spectroscopy and Surface Vibrations', (Academic Press, New York, 1982)
- [8] R.F. Willis, 'Vibrational Spectroscopy of Adsorbates'. Springer Series in Chemical Physics, Vol.15.
- [9] D.M. Newns, *Phys., Letts.*, 60 A (1977) 464
- [10] M.A. Chesters and N. Sheppard 'Electron Energy Loss Spectroscopy' in *Spectroscopy of Surfaces* (Eds. R.J.H. Clarke and R.E. Hester) (Wiley 1988)
- [11] P.R. Griffith, *Chemical Infrared Fourier Transform Spectroscopy*, (Wiley 1975)
- [12] W.D. Perkins, *J. Chem. Ed.*, 63 (1986) A5; *J.Chem. Ed.* 64 (1987) A269
- [13] F.M. Hoffmann, *Surf. Sci. Reports*, 2 (1983) 107
- [14] P. Hollins and J. Pritchard, *Progress in Surf. Sci.*, 19 (1985) 275
- [15] M.A. Chesters, *J. Electron Spec. Rel. Phenom.*, 38 (1986) 123

- [16] B.E. Hayden, in 'Methods of Surface Characterisation', Vol. 1, Eds. J.T. Yates and T.E. Madey (Plenum, New York 1987)
- [17] Y.J. Chabal, Surf. Sci. Reports 8 (1988) 211
- [18] A.M. Bradshaw and E. Schweizer, in 'Spectroscopy of Surfaces' (Eds. R.J.H. Clarke and R.E. Hester) (Wiley 1988)
- [19] S.A. Francis and A.H. Ellison, J. Opt. Soc. Amer., 49 (1959) 131
- [20] R.G. Greenler, J. Chem. Phys., 44 (1966) 310
- [21] J. Pritchard and M.L. Sims, Trans. Farad. Soc. 72 (1978) 513
- [22] H.A. Pearce and N. Sheppard, Surf. Sci., 59 (1976) 205
- [23] J.C. Wenger PhD Thesis UEA 1993
- [24] D. Oakes PhD Thesis UEA 1994
- [25] H.E. Newell PhD Thesis University of Nottingham 1997. With kind permission.
- [26] G. Margaritondo, 'Introduction to Synchrotron Radiation', (Oxford University Press, 1988)
- [27] D.A. Slater, P. Hollins, M.A. Chesters, J.Pritchard, D.H. Martin, M. Surman, D.A. Shaw and I. Munro, Rev. Sci. Instrum., 63 (1992) 1547
- [28] D.H. Martin, Report on Contract B 13344XT to Daresbury Laboratory
- [29] Ken Wood, QMC Instruments Ltd. Private Communication

Chapter Three

The Adsorption of 3,3,3-trifluoropropene on Pt (111)

3.1 Introduction

3.2 Experimental

3.2.1 RAIRS

3.2.2 EELS

3.3 Results

3.3.1 EELS - Clean Surface Spectra

3.3.2 EEL and RAIR Spectra of 3,3,3-trifluoropropene

3.4 Discussion

3.5 Comparison of EELS and RAIRS Intensities

3.6 Conclusions

3.7 References

3.1 Introduction

The possibility of producing a surface which has specific chemical and physical properties has been enhanced in recent years with the development of stable-structured monolayer assemblies consisting of long-chain amphiphiles. They are known to be close-packed ordered structures exposing a variety of chemical functionalities at the outer monolayer interface. One such monolayer, perfluorinated acid ester (PFAE), has been studied due to its exposed CF_3 group [1]. The purpose of this study was to model an amphiphile by a CF_3 terminated short-chain hydrocarbon where the end group has been replaced by a Pt metal surface, for use in molecular beam experiments.

Molecular beam scattering from solid surfaces is a way of probing energy transfer between gas molecules and the surface. Time-of-flight methods have been used to probe changes in translational energy of the colliding particle. Laser spectroscopic techniques (LIF and REMPI) can be used to examine transfer of internal energy (vibrational, rotational).

The extent of energy transfer is sensitive to the nature of the surface. Most studies of this type have concentrated on scattering from metal surfaces. More recently other 'organic' surfaces have been probed. Cohen *et al* [2] scattered NO from two different long chain (C_{18}) self-assembled monolayers (SAM), one of which was methyl, CH_3 , terminated and one which was CF_3 terminated. They observed that the extent of rotational energy transfer of NO was far greater when scattered from the methyl terminated SAM than the CF_3 terminated SAM. They attributed

this difference as being due to more efficient energy transfer with the high frequency internal modes of the methyl group (rotations, vibrations) as compared to the low frequency CF_3 internal modes. Their interpretation was limited because of the length of the chains and the complexity of the layers. They couldn't say exactly which modes were responsible for the rotational excitation.

Examining smaller hydrocarbon chains adsorbed onto single crystal surfaces under well controlled conditions may reveal more detailed information on these energy transfer processes.

The reaction of adsorbed propene ($\text{CH}_3\text{CH}=\text{CH}_2$) on Pt(111) to form the surface propylidyne species ($\text{CH}_3\text{CH}_2\text{CM}_3$, M=Metal) has been extensively studied [3,4]. The terminal CH_3 group in this species was an ideal candidate to functionalise. Substituted propenes such as halogenated propenes have been employed previously in studies in order to investigate mechanistic, inductive or back-bonding effects. The substituted propene, 3,3,3-trifluoropropene ($\text{CF}_3\text{CH}=\text{CH}_2$) was chosen with the expectation that it would undergo a similar reaction to propene to form the fluorinated alkylidyne species ($\text{CF}_3\text{CH}_2\text{CM}_3$), which possesses the desired terminal CF_3 group.

The 3,3,3-trifluoropropene was therefore studied under identical conditions to the formation of propylidyne. The purpose was to confirm that 3,3,3-trifluoropropylidyne is formed and that another reaction is not occurring.

3.2 EXPERIMENTAL

3.2.1 RAIRS

The Pt (111) crystal cleaning procedure and method used to monitor the surface cleanness have been described in section 2.6.4. The CO used in monitoring the surface cleanness was then flashed off by rapidly increasing the temperature to at least 473 K twice to desorb the CO. Then the temperature was held constant at approximately 360 K whilst the background spectra was recorded. The 3,3,3-trifluoropropene dosing was achieved by backfilling the vacuum chamber. All exposures are based on uncorrected ion gauge readings and are expressed in Langmuirs. The sample spectrum was collected at 360 K. Subsequent spectra were then taken at elevated temperatures. Spectra were recorded at either 4 cm⁻¹ or 2 cm⁻¹ resolution as the result of 1024 or 256 scans taking 6 or 3 minutes.

3.2.2 EELS

The Pt (111) crystal cleaning procedure and checks of cleanness have been described in section 2.2.7. Following annealing the temperature was allowed to cool to 360 K and then it was kept constant whilst the 3,3,3-trifluoropropene was dosed on by backfilling the chamber. The spectra were all recorded at 300 K. Both on and off-specular

measurements were undertaken. The resolution was between 3-4 meV. A typical scan was measured in 0.49 meV steps with a gate time of 3 seconds/step.

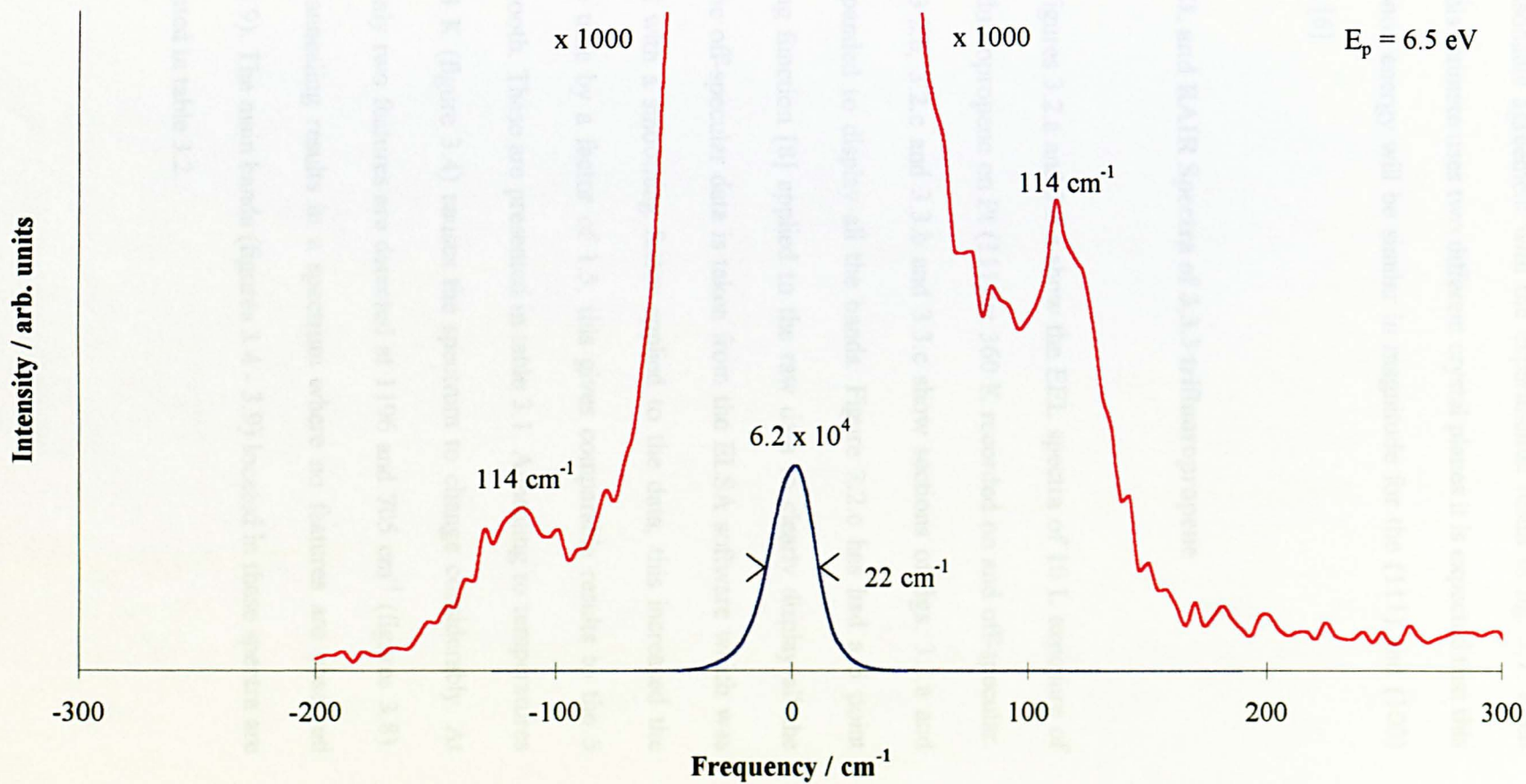
3.3 Results

3.3.1 EELS-Clean Surface Spectra

The EEL spectra of the clean Pt (111) surface shows a single loss at $114 \pm 5 \text{ cm}^{-1}$ (fig 3.1). This was unexpected as there have been no previous reports of this excitation from EELS. The gain peak at 114 cm^{-1} is observed at room temperature with the loss : gain intensity ratio as expected from the difference in the population of the ground and first excited states.

This vibrational feature will be assigned to a bulk phonon of the Pt crystal and is equivalent to the phonon excitation previously described for Ni and Cu surfaces as discussed in [5]. It corresponds to rigid displacements of the (111) lattice planes against each other. This generates an active normal component μ of the dipole moment because the top layer of metal atoms has a different charge distribution than the lower layers. Hence the dipole is generated by the bulk phonon at the surface. The incident electron will excite only longitudinal phonons propagating normal to the surface by dipole scattering for the (111) surface. The equivalent feature on Cu (100) has been measured at $\cong 155 \text{ cm}^{-1}$, which, if scaled by

Figure 3.1 The Elastic Peak Region of the EEL Spectrum of the Clean Pt (111) Surface



the ratio of the maximum phonon frequencies for platinum and copper (192 cm^{-1} : 238 cm^{-1} [6,7]) would occur at 126 cm^{-1} on Pt (111). This gives reasonable agreement with the experimental result in fig. 3.1. Even though this estimate uses two different crystal planes it is expected that this bulk phonon energy will be similar in magnitude for the (111) and (100) direction [6].

3.3.2 EEL and RAIR Spectra of 3,3,3-trifluoropropene

Figures 3.2.a and 3.3.a show the EEL spectra of 10 L exposure of 3,3,3-trifluoropropene on Pt (111) at 360 K recorded on and off-specular. Figures 3.2.b, 3.2.c and 3.3.b and 3.3.c show sections of figs. 3.2.a and 3.3.a expanded to display all the bands. Figure 3.2.c has had a 5 point smoothing function [8] applied to the raw data to clearly display all the bands, the off-specular data is taken from the ELSA software which was recorded with a smoothing factor applied to the data, this increased the response time by a factor of 1.5, this gives comparable results to the 5 point smooth. These are presented in table 3.1. Annealing to temperatures of $> 473\text{ K}$ (figure 3.4) causes the spectrum to change considerably. At 730 K only two features are detected at 1196 and 705 cm^{-1} (figures 3.8). Further annealing results in a spectrum where no features are observed (figure 3.9). The main bands (figures 3.4 - 3.9) located in these spectra are documented in table 3.2.

Figure 3.2.a The On-specular EEL Spectrum Recorded Following an Exposure of 10 L of 3,3,3-trifluoropropene to the Pt(111) Crystal at 360 K

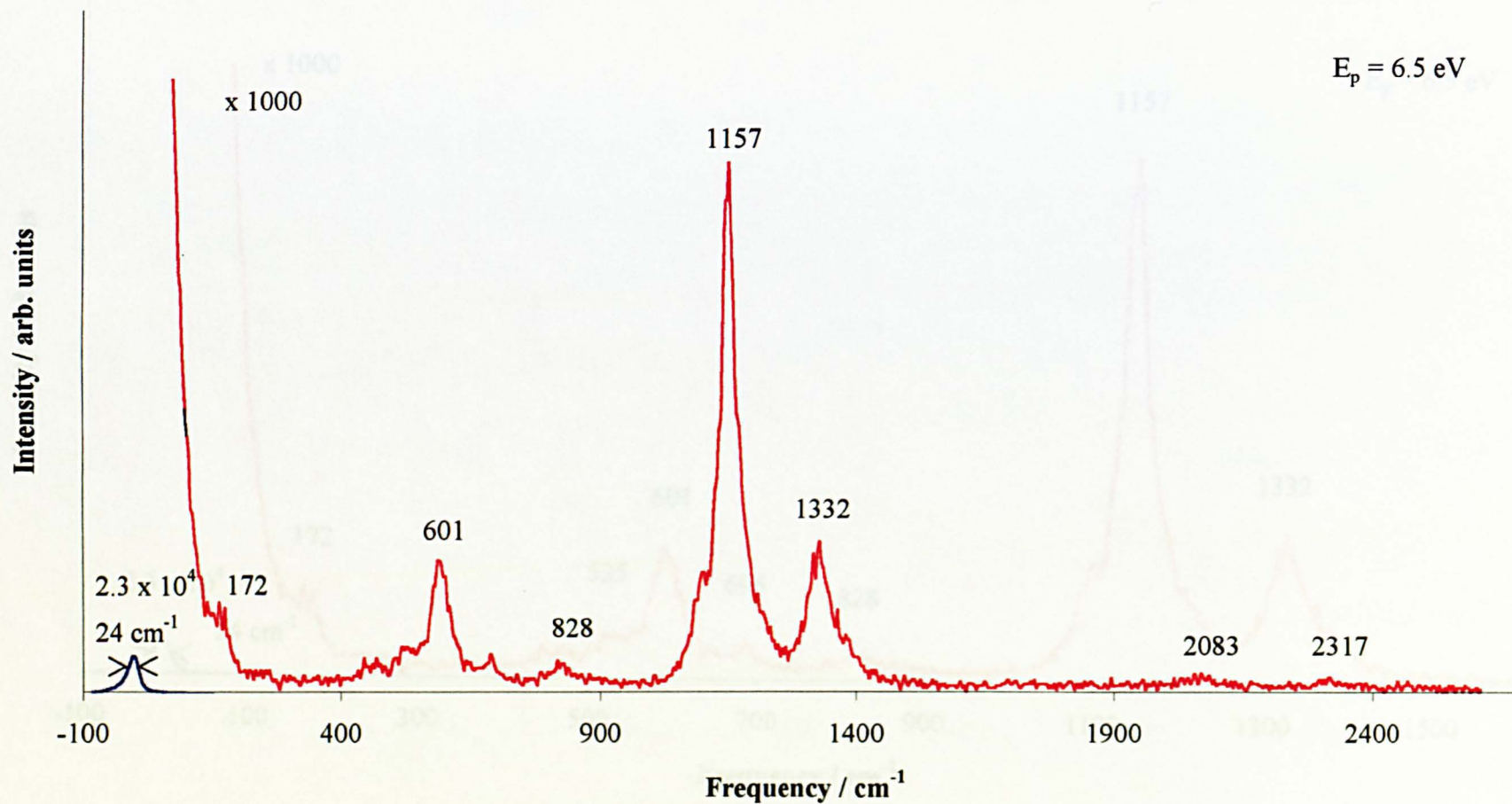


Figure 3.2.b Expanded Low Frequency Region of the On-specular EEL Spectrum Recorded Following Exposure of 10 L 3,3,3-trifluoropropene to the Pt(111) Crystal at 360 K

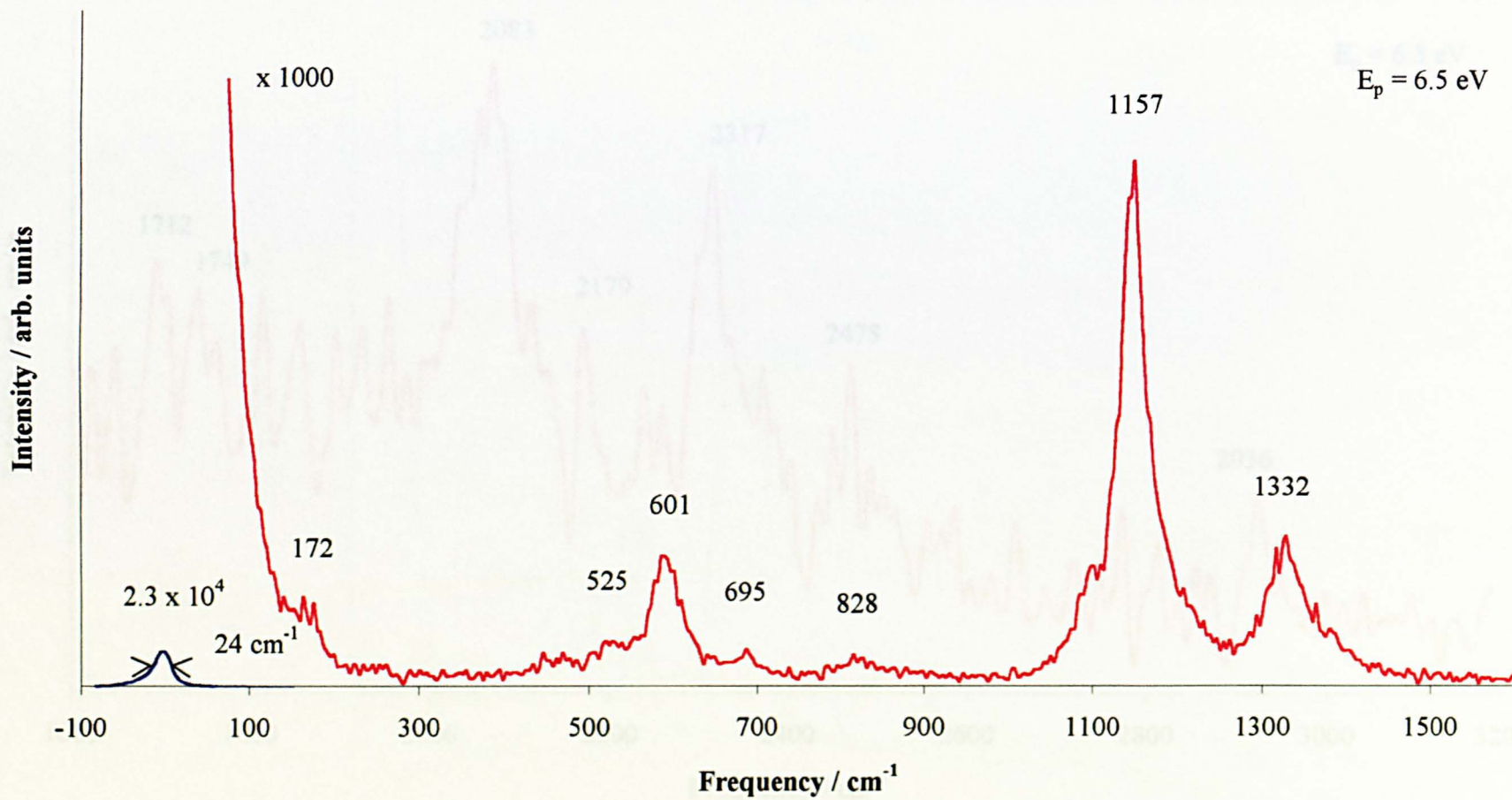


Figure 3.2.c Expanded High Frequency Region of the On-specular EEL Spectrum Recorded Following Exposure of 10 L 3,3,3-trifluoropropene to the Pt(111) Crystal at 360 K

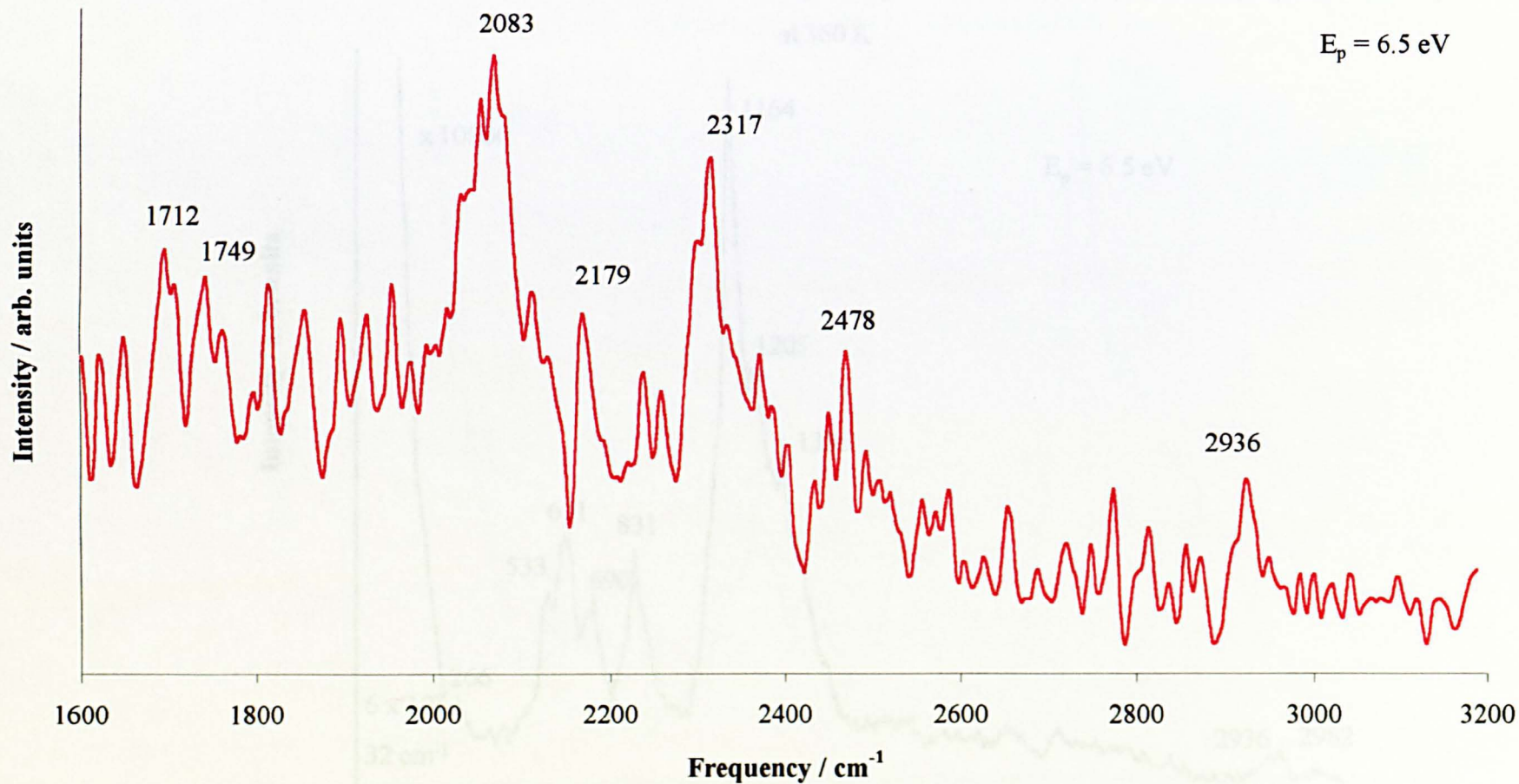


Figure 3.3.a The Off-specular (12°) Spectrum Recorded Following an Exposure of 10 L of 3,3,3-trifluoropropene to the Pt (111) Crystal at 360 K

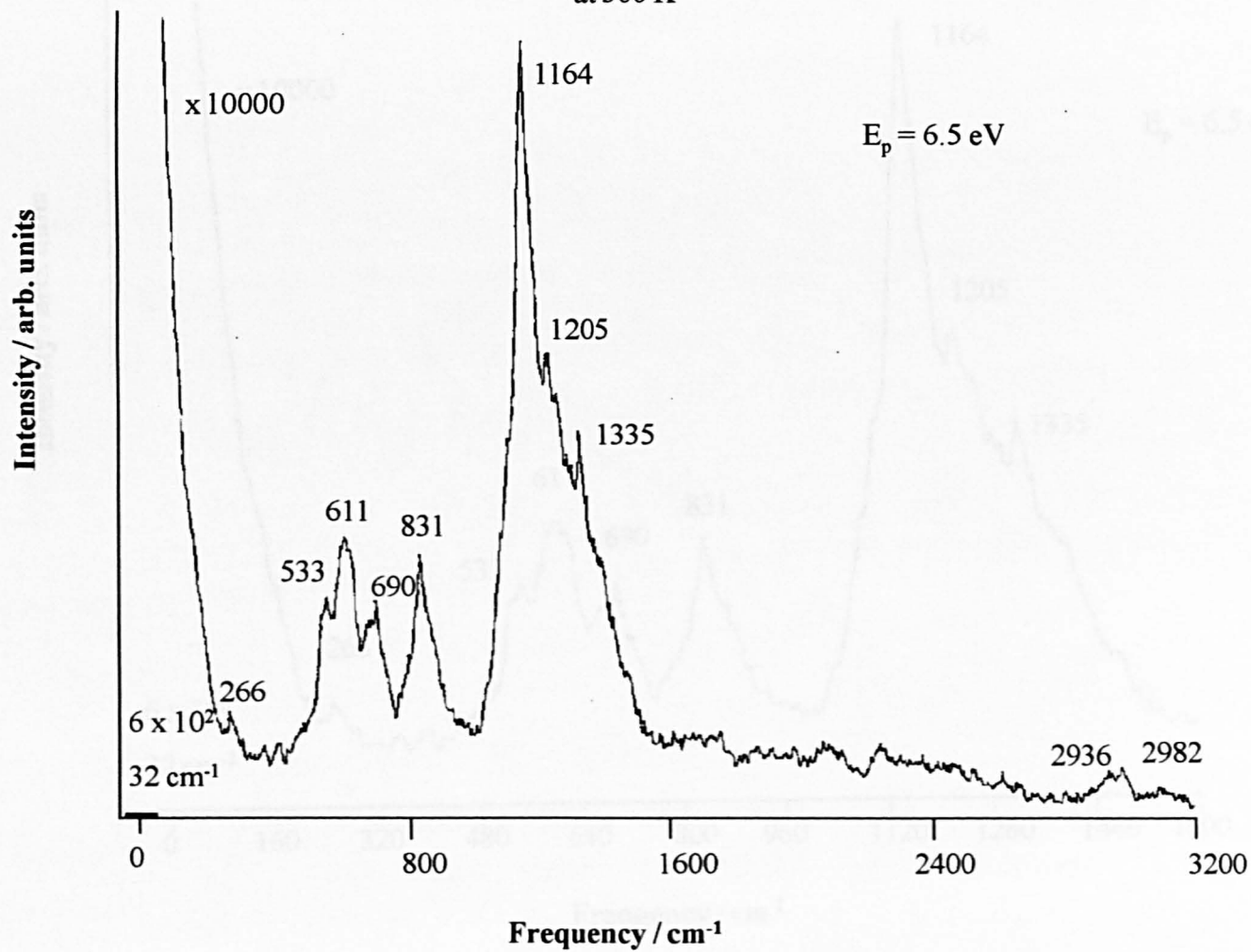


Figure 3.3.b Expanded Low Frequency Region of the Off-specular (12°) Spectrum Recorded Following an Exposure of 10 L of 3,3,3-trifluoropropene to the Pt (111) Crystal at 360 K

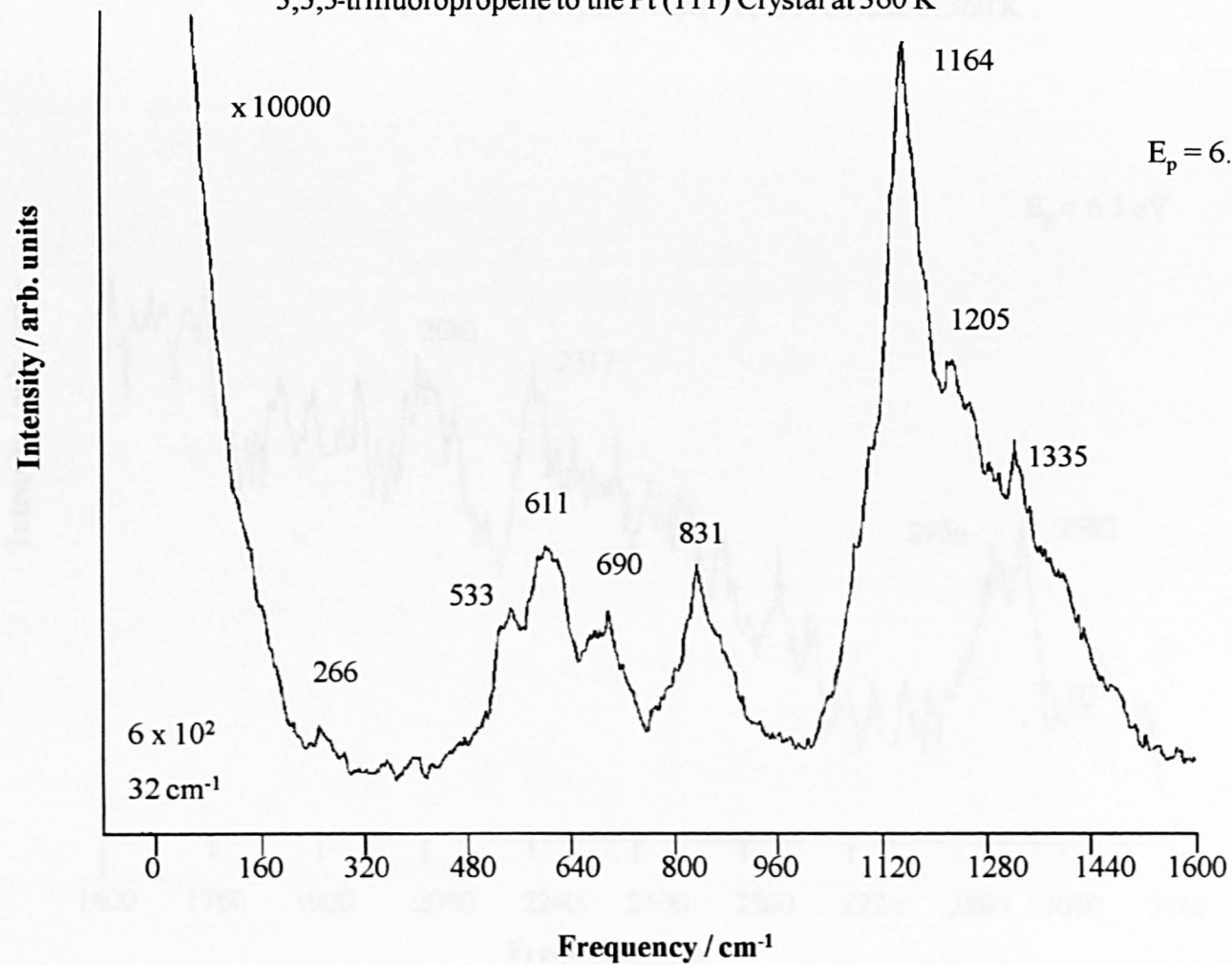


Figure 3.3.c Expanded High Frequency Region of the Off-specular (12°) Spectrum Recorded Following an Exposure of 10 L of 3,3,3-trifluoropropene to the Pt (111) Crystal at 360 K

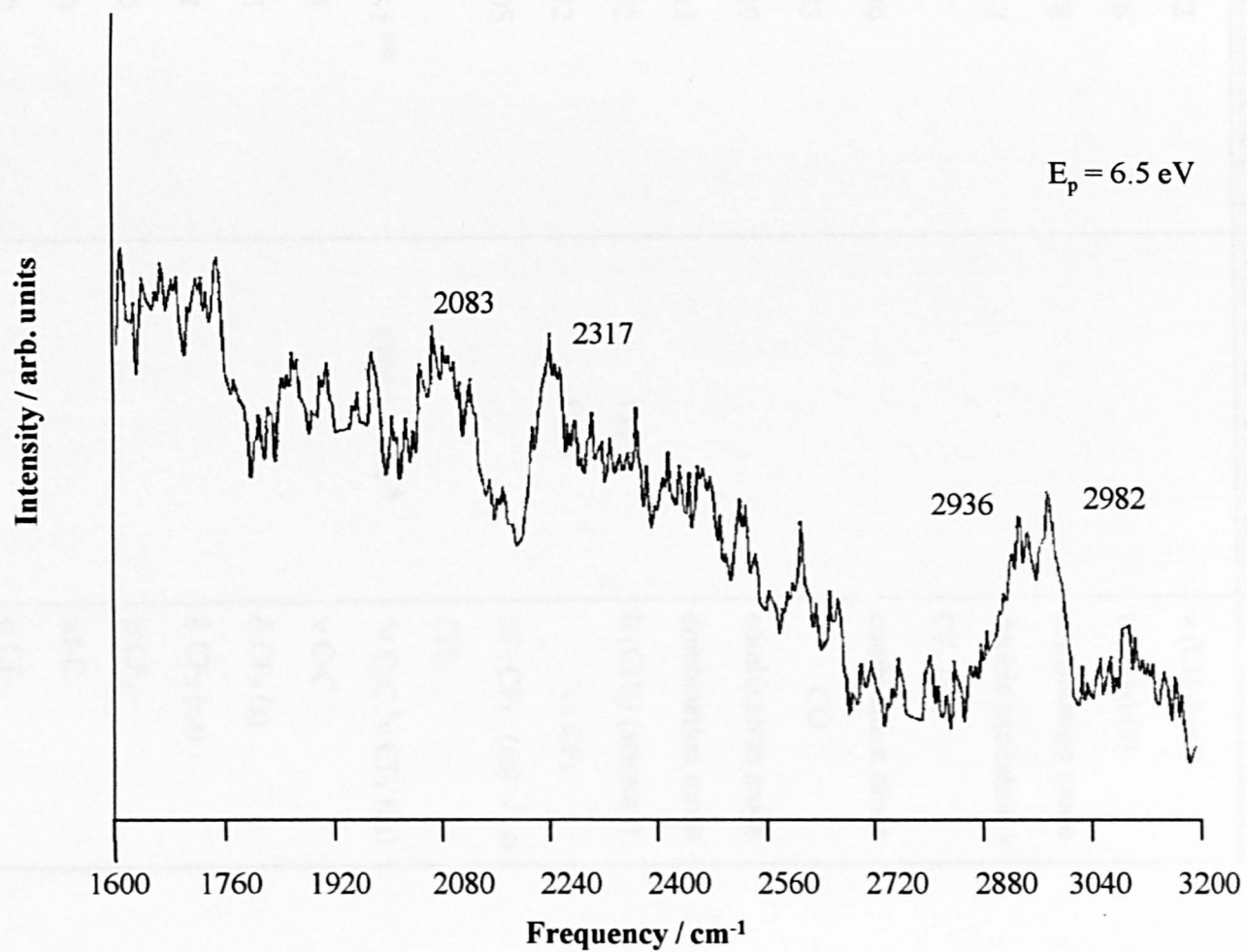


Table 3.1 The assignment of the observed IR and EELS bands from 3,3,3-trifluoropropene adsorbed on Pt (111)

Pt (111) EELS at 360 K (cm ⁻¹)	Pt (111) RAIRS at 360 K (cm ⁻¹)	Assignments
2982		ν (CH ₂) (as)
2936		ν (CH ₂) (s)
2478		combination mode
2317		double excitation ν CF ₃ (as)
2179		combination mode
2083		CO
1749		combination mode
1712		combination mode
1392	1397	δ (CH ₂) (scissors)
1332	1334	vs CF ₃
1205		2 δ CF ₃ (as) / ω CH ₂
1157 ^{a+b}	1105 ^a 1164 ^b	^a ν C-C ^b ν CF ₃ (as)
828		ν C-C
695		δ CF ₃ (s)
601		δ CF ₃ (as)
525		ρ CF ₃
470		M-C
400		ρ CF ₃
357		ρ CH ₂
266		δ C-C-C
172		surface phonon

Figure 3.4 The EEL Spectrum Recorded Following Exposure of 10 L 3,3,3-trifluoropropene to the Pt(111) Crystal at 360 K and Subsequent Annealing to 473 K

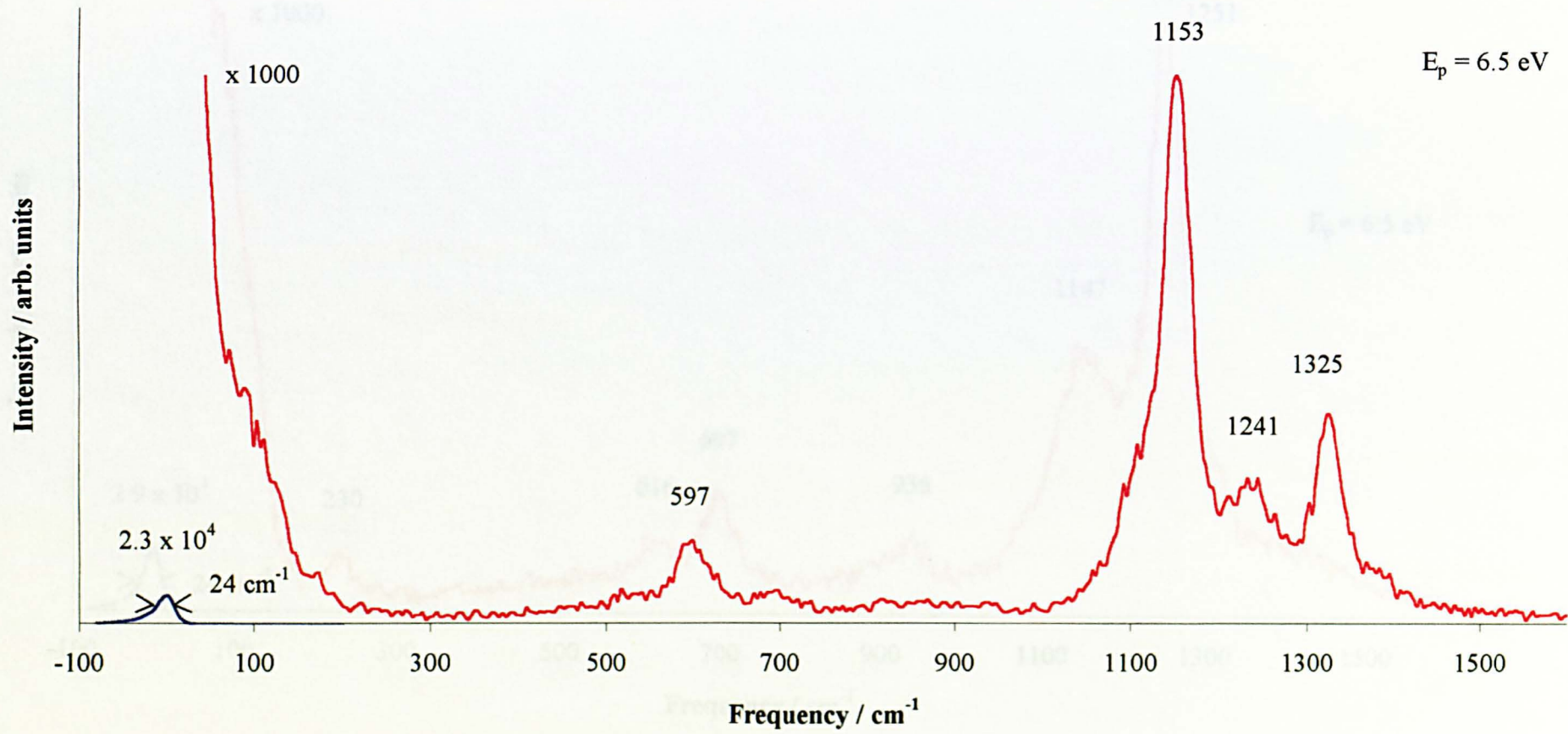


Figure 3.5 The EEL Spectrum Recorded Following Exposure of 10 L 3,3,3-trifluoropropene to the Pt(111) Crystal at 360 K and Subsequent Annealing to 501 K

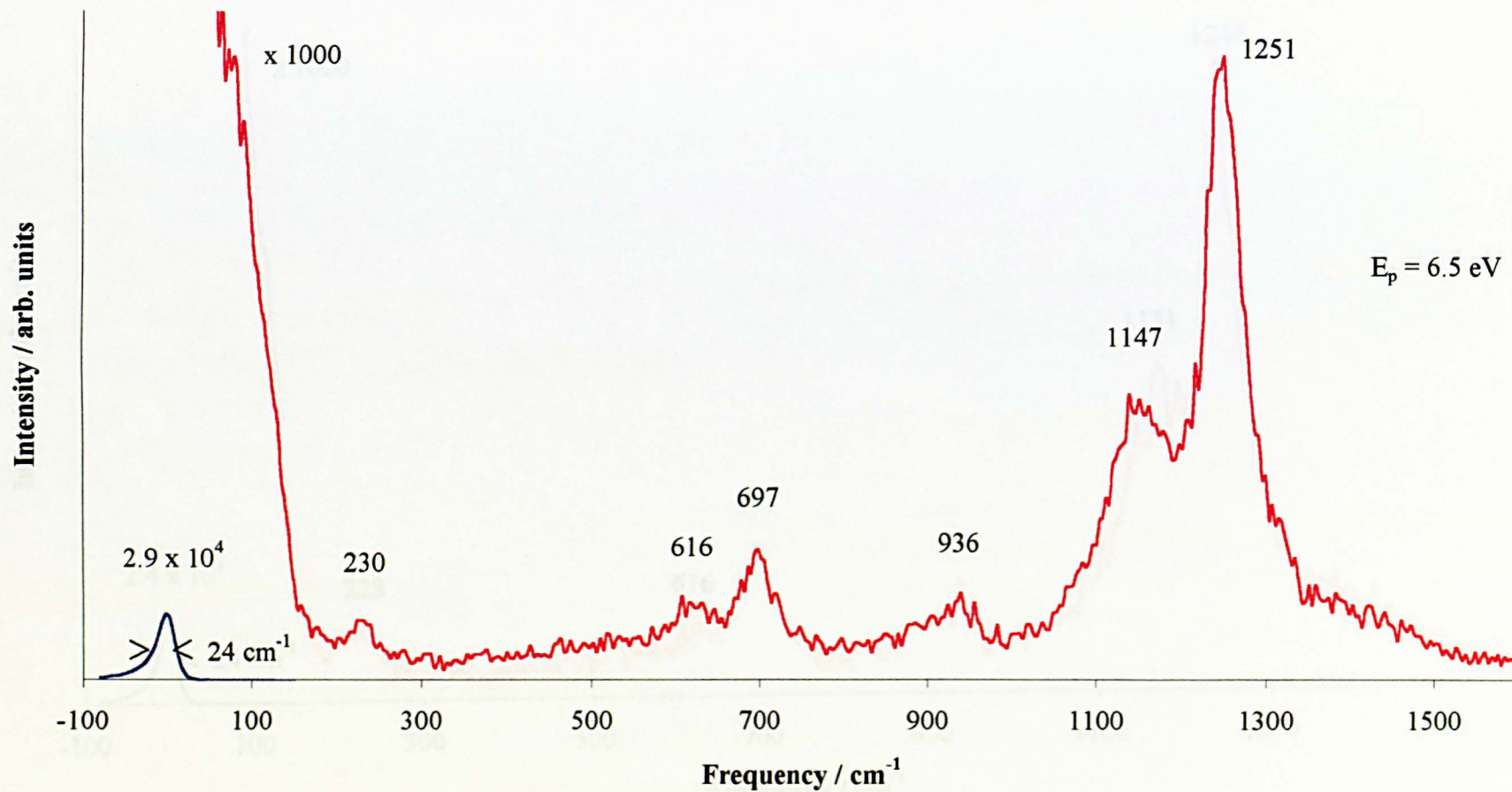


Figure 3.6 The EEL Spectrum Recorded Following Exposure of 10 L 3,3,3-trifluoropropene to the Pt(111) Crystal at 360 K and Subsequent Annealing to 570 K

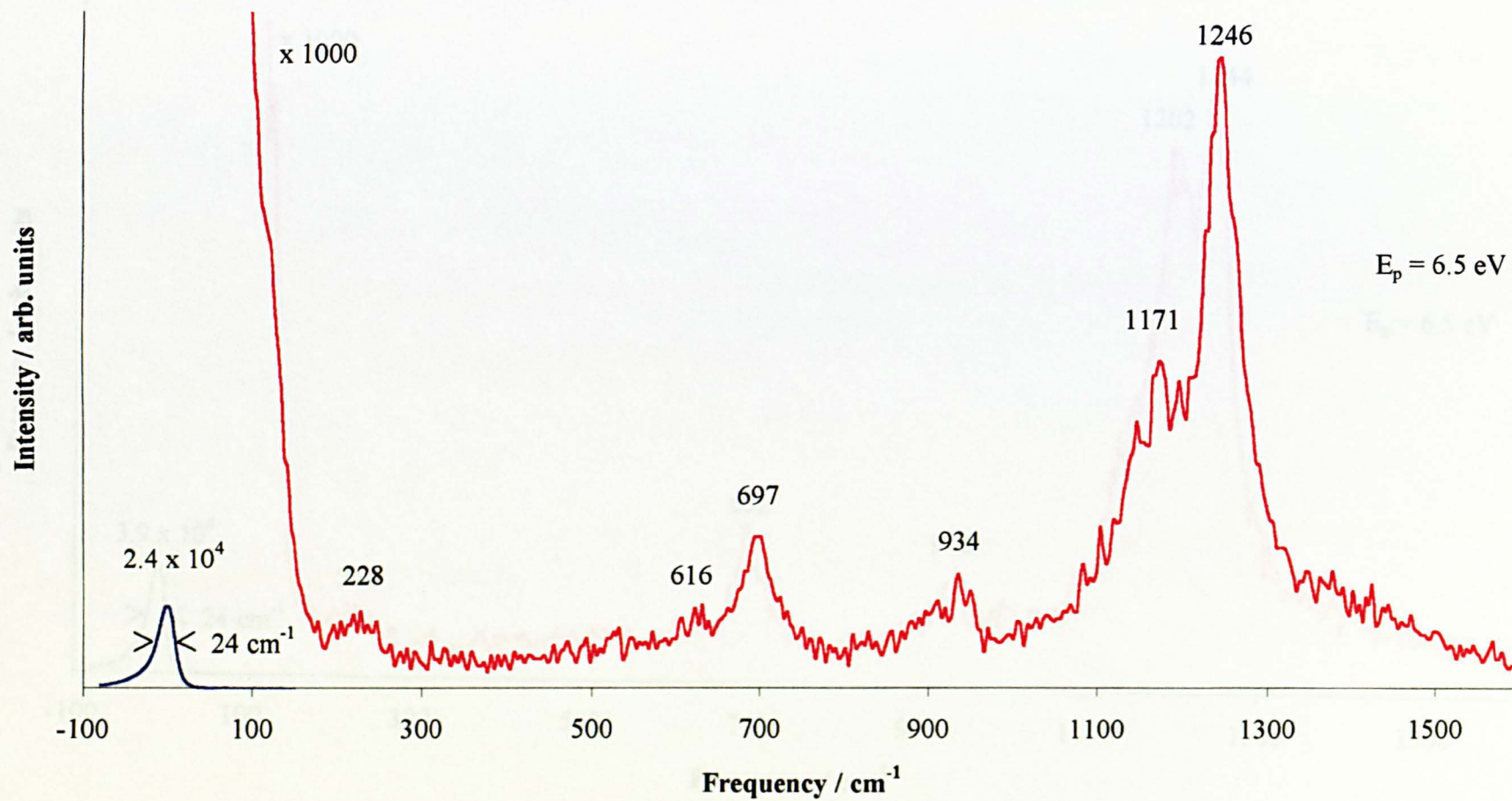


Figure 3.7 The EEL Spectrum Recorded Following Exposure of 10 L 3,3,3-trifluoropropene to the Pt(111) Crystal at 360 K and Subsequent Annealing to 625 K

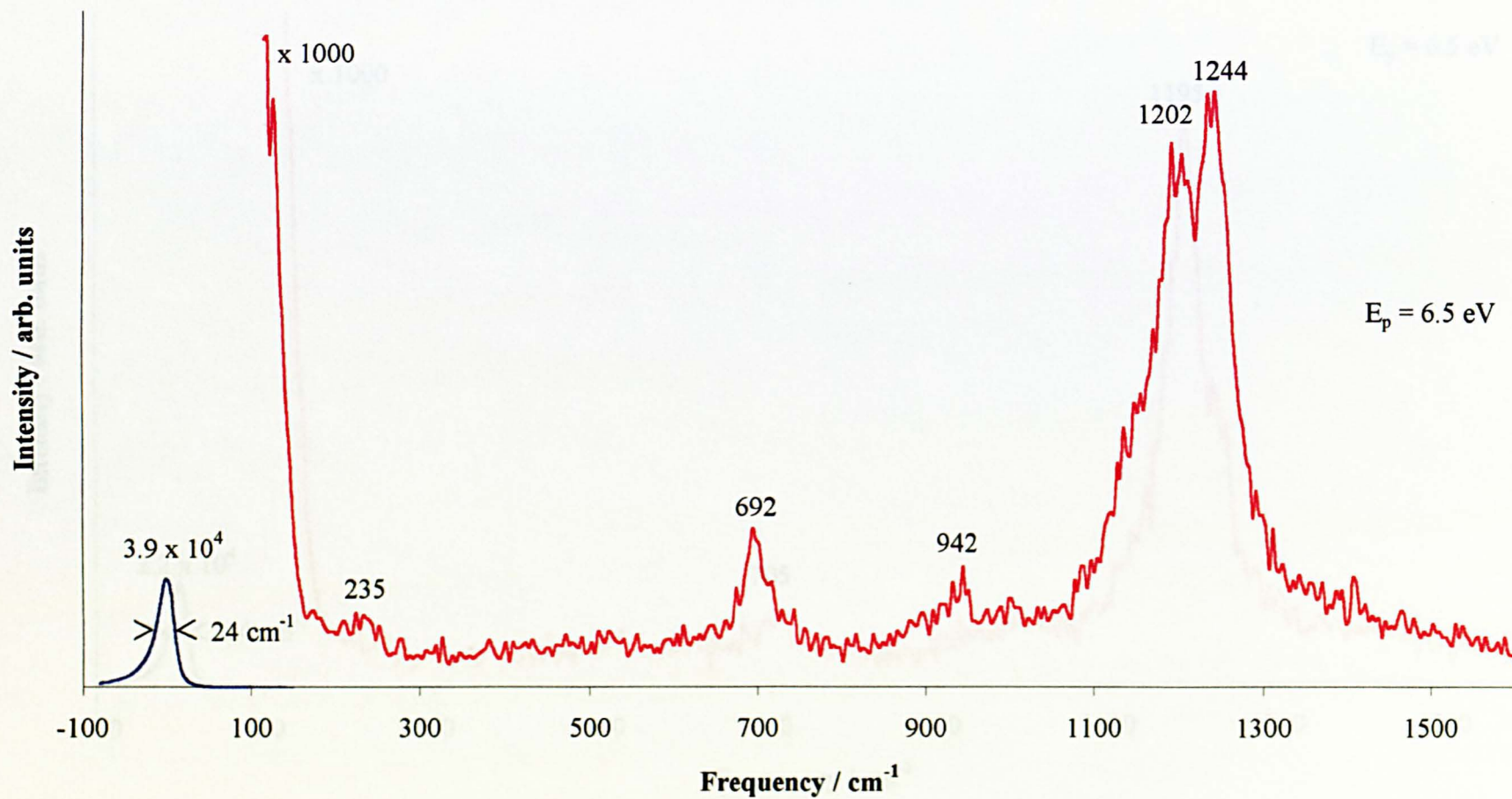


Figure 3.8 The EEL Spectrum Recorded Following Exposure of 10 L 3,3,3-trifluoropropene to the Pt(111) Crystal at 360 K and Subsequent Annealing to 730 K

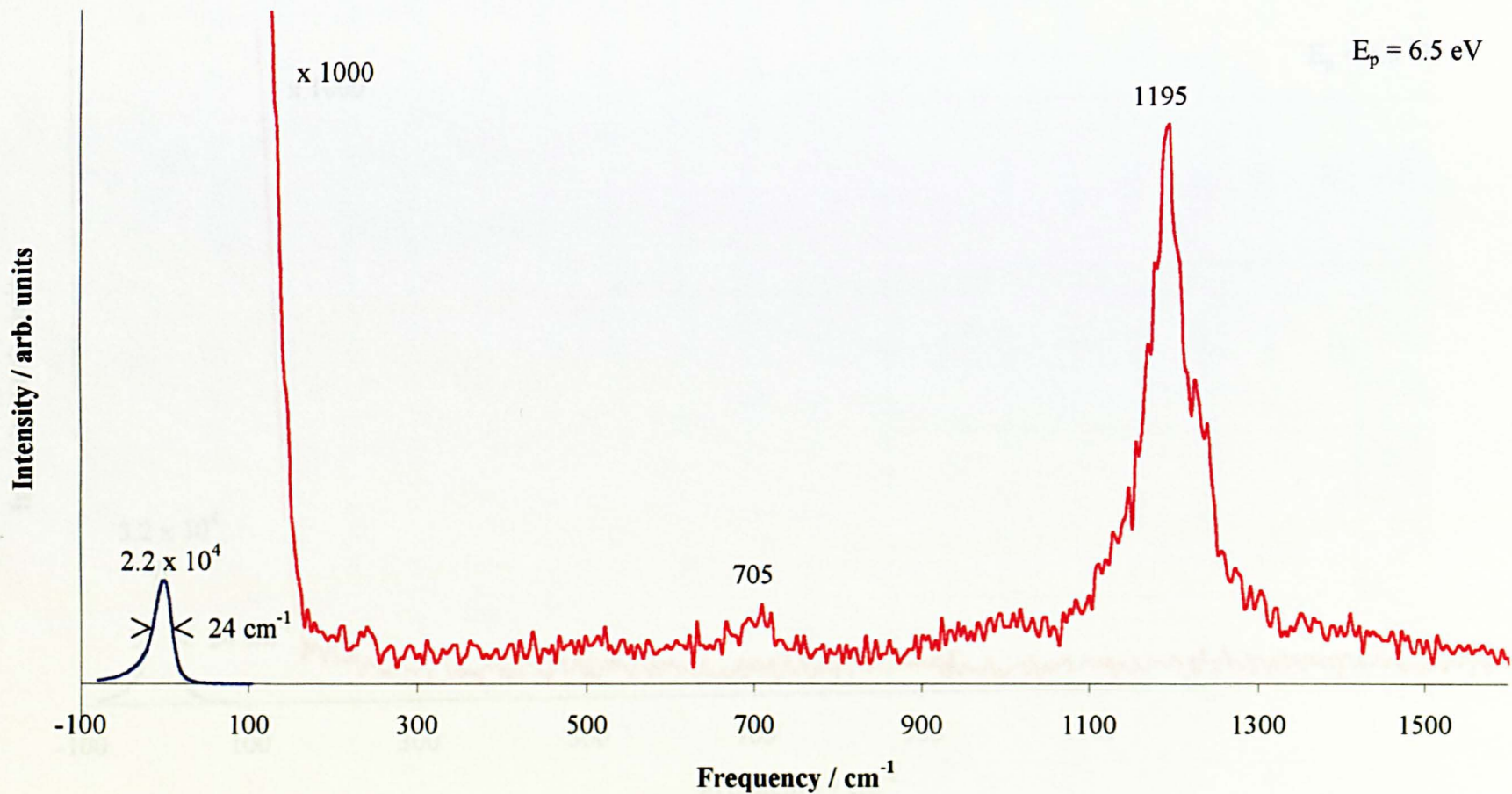


Figure 3.9 The EEL Spectrum Recorded Following Exposure of 10 L 3,3,3-trifluoropropene to the Pt(111) Crystal at 360 K and Subsequent Annealing to 873 K

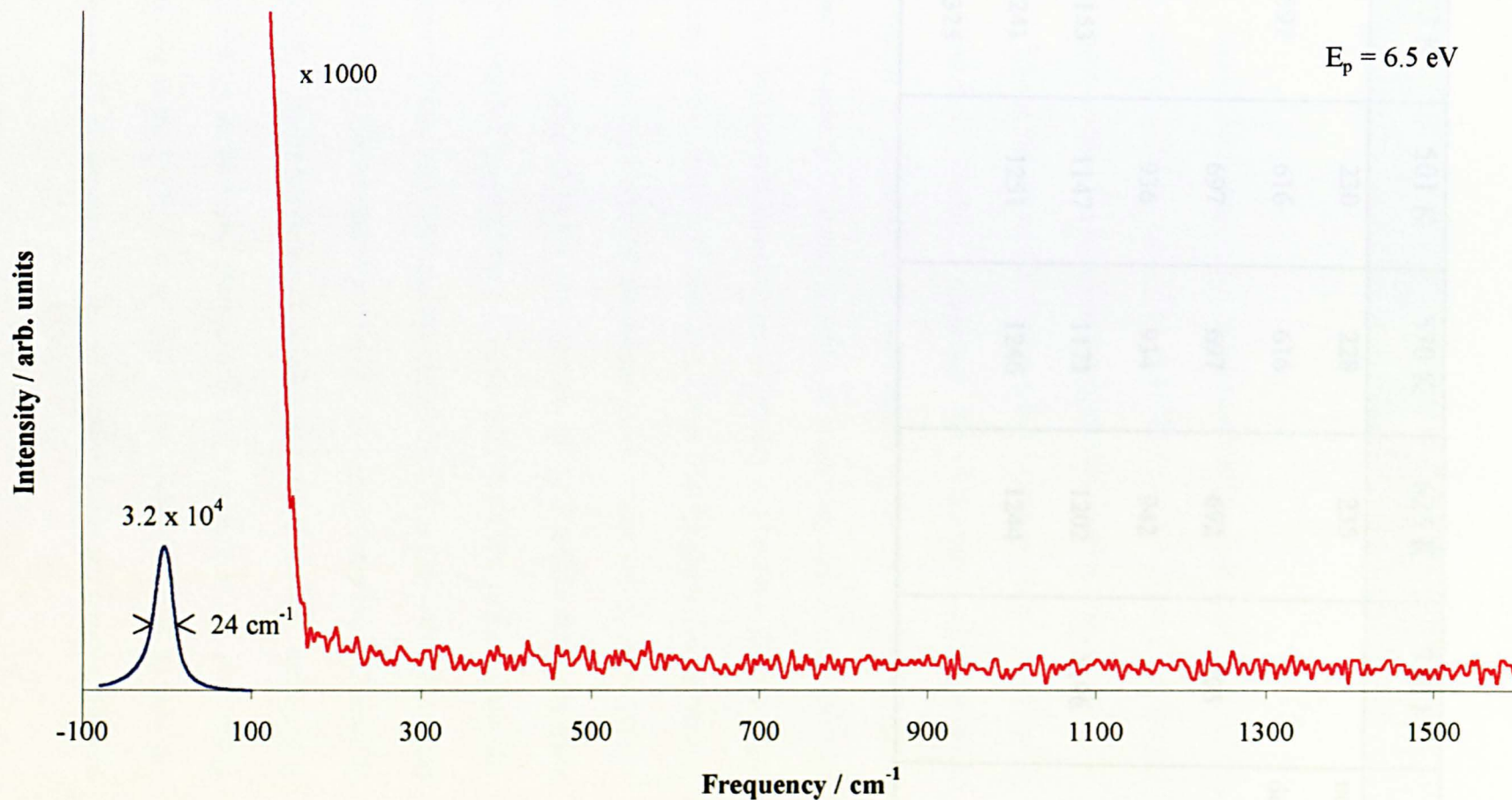


Table 3.2 Vibrational frequencies (cm^{-1}) for the different bands observed at increasing annealing temperatures for 3,3,3-trifluoropropene

473 K	501 K	570 K	625 K	730 K	873 K
	230	228	235		no bands detected
597	616	616			
	697	697	692	705	
	936	934	942		
1153	1147	1171	1202	1196	
1241	1251	1246	1244		
1325					

Figure 3.10 shows the RAIR spectra of 10 L exposure of 3,3,3-trifluoropropene on Pt (111) at 360 K. Bands are seen at 1397, 1334, 1205 and 1105 cm^{-1} .

3.4 Discussion

The vibrational spectrum of the result of propene adsorption at 360 K has been recorded previously on Pt (111) by EELS [3] and RAIRS [4] and has been assigned in terms of a propylidyne species. This is shown in fig. 3.11. The symmetry of this fragment if the metal surface is regarded as a flat plane is C_s . Under C_s symmetry, the vibrational modes are either symmetric A' or asymmetric A'' with respect to the mirror plane. If the symmetry is strictly C_s , then according to the metal surface selection rule only the A' modes will be observed. A'' modes will become allowed if the symmetry is not strictly C_s , but C_1 . Table 3.3 indicates the symmetry assignment for each type of vibrational mode under the C_s point group. Assignments (table 3.1) for the reaction of 3,3,3-trifluoropropene have been in terms of a propylidyne species with previous studies given for comparison (table 3.4). The assignment of the CF_3 group was made using frequencies for 3,3,3-trifluoropropene in the vapour state [9] and data for $\text{CF}_3\text{CH}_2\text{OH} / \text{Ag} (110)$ (tables 3.5 and 3.6) [10]. The (110) surface is a low symmetry surface and therefore is not expected to be particularly comparable to the (111) surface. Due to the greater mass of fluorine the CF_3 modes will be expected to appear at much lower frequencies than the

Figure 3.10 The RAIRS Spectrum Recorded Following Exposure of 10 L of 3,3,3-trifluoropropene to the Pt (111) Crystal at 360 K

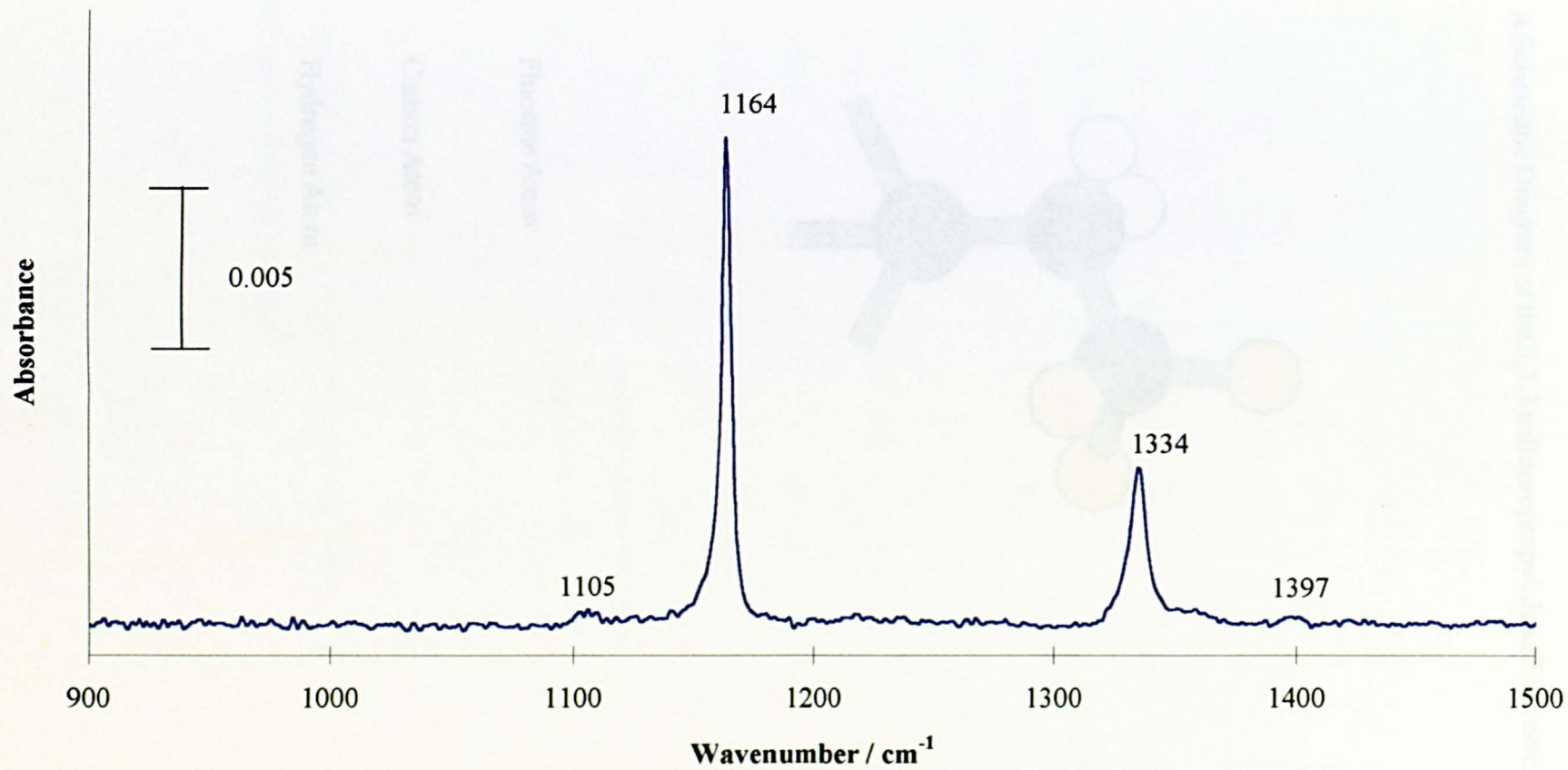


Table 3.3 The symmetry assignment for the vibrational modes of
3,3,3-trifluoropropylidyne

Description of mode	Symmetry under the C_s point group
ν CF ₃ (a)	$\underline{A}' + A''$
ν CH ₂ (a)	A''
ν CF ₃ (s)	\underline{A}'
ν CH ₂ (s)	\underline{A}'
δ CF ₃ (a)	$\underline{A}' + A''$
δ CH ₂ (s)	\underline{A}'
δ CF ₃ (s)	\underline{A}'
ν CC	\underline{A}'
ω CH ₂	\underline{A}'
ρ CF ₃	$\underline{A}' + A''$
ρ CH ₂	A''

ν = stretch

(a) = antisymmetric

δ = deformation

(s) = symmetric

ω = wag

ρ = rock

A' = totally symmetric mode with respect to the mirror plane

A'' = antisymmetric mode with respect to the mirror plane

Table 3.4 Assignment of the observed IR and EELS bands from propene adsorbed on Pt (111)

Pt (111) EELS at 300 K (cm^{-1})[3]	Pt (111) RAIRS at 340 K (cm^{-1})[4]	Assignments
ca 2980	2961	ν CH ₃ (as)
ca. 2920	2921	ν CH ₂ (s) ^a
	2865	ν CH ₃ (s)
1465	1450	δ CH ₃ (as)
	1407	δ CH ₂ (scissors)
1295	1303	ω CH ₂
1115	1103	ν CC
	1055	ρ CH ₃ (A'')
1055	1039	ρ CH ₃
940	929	ν CC
825	remaining modes below	ρ CH ₃
440	cut-off of detector	ν M-C
250		δ CCC (s)

^a This is a rather higher value than anticipated for propylidyne; it might alternatively be the overtone 2 δ (CH₃) as for that species in Fermi resonance with ν (CH₃) s, with ν (CH₂) s coincident with ν (CH₃) s at 2865 cm^{-1} .

ν = stretch

(a) = antisymmetric

δ = deformation

(s) = symmetric

ω = wag

ρ = rock

A'' = antisymmetric mode with respect to the mirror plane

Table 3.5 The fundamental frequencies for 3,3,3-trifluoropropene in the vapour state

CH ₂ =CHCF ₃ (vapour state) cm ⁻¹ [9]	Assignment
3124	CH ₂ stretch (a')
3067	CH stretch (a')
3024	CH ₂ stretch (a')
1669	C=C stretch (a')
1443	CH ₂ bend (a')
1306 ^a	CH bend (a')
1286	CF ₃ stretch (a')
1173 (1166) ^a	CF ₃ stretch (a'')
1173 (1139) ^a	CF ₃ stretch (a'')
1024	CH ₂ rock (a')
980	trans-CH wag (a'')
964	CH ₂ wag (a'')
811	C-C stretch (a')
718	CF ₃ deformation (a')
635	C=C twist (a'')
552	CF ₃ deformation (a', a'')
431	C=C-C bend (a')
318	CF ₃ rock (a', a'')
.....	CF ₃ torsion (a'')

^a Bands observed in CS₂ solution

Table 3.6 EELS data for 3,3,3-trifluoropropanol adsorbed on Ag (110) at monolayer coverage

Vibrational frequency (cm^{-1}) [10]	Assignment
~ 3300	ν OH
2980	ν CH ₂
1410	δ CH ₂
1265	ν CF ₃ (as)
1180	ν CF ₃ (s)
1065	ν CO
940	ρ CH ₂
850	ν CC
670	γ OH
670	δ CF ₃
540	δ CF ₃

CH₃ modes in propylidyne. The other modes are expected to appear at similar frequencies to those of propylidyne, although the inductive effects of the fluorine would be expected to shift the frequencies of these modes to lower wavenumbers (due to a weakening of the CH and CC bonds).

The ν (as) CF₃ mode dominates the spectrum at 1157 cm⁻¹. This is because the dynamic dipole moment of this group is oriented almost perpendicular to the surface. The corresponding ν (s) CF₃ occurs at 1332 cm⁻¹ from group frequency considerations. The symmetric CH₂ stretch has been assigned to the band at 2936 cm⁻¹ in accordance with [4]. The alternative assignment of 2 δ (as) CH₃ which has been suggested is not of consequence here. The band at 2982 cm⁻¹ has been assigned to the antisymmetric CH₂ stretch. This band has A^{||} symmetry and it is not expected to occur. However it is seen in an off-specular geometry where impact scattering dominates.

The CF deformation region is also assigned on group frequency grounds. The 695 and 601 cm⁻¹ bands are the symmetric and antisymmetric CF₃ deformations respectively and the 1392 cm⁻¹ peak is the CH₂ scissors mode, δ (s) CH₂. The bands at 1105 and 828 cm⁻¹ are assigned to the two ν C-C modes. The band at 266 cm⁻¹ is assigned to the symmetric C-C-C deformation mode in comparison with [3]. From the same data, the 470 cm⁻¹ band is assigned to the M-C stretch. Rocks are assigned to bands at 525 and 400 cm⁻¹ (ρ CF₃) and 357 (ρ CH₂). The band at 172 cm⁻¹ has been assigned to a surface phonon allowed due to the presence of the alkylidyne

layer, as no vibrational modes of the 3,3,3-trifluoropropylidyne species are expected to appear at this low frequency.

The feature at 2317 cm^{-1} is assigned to the double excitation of $\nu(\text{as})\text{CF}_3$ at 1157 cm^{-1} . If there is a 1% probability of an electron (either incoming or outgoing) exciting a particular vibrational mode of a species adsorbed on the surface, then there is a $(1\%)^2$ probability of exciting the same vibration twice. This is known as double excitation and occurs at exactly twice the fundamental frequency.

The decomposition of propylidyne on Pt (111) is not clearly understood as to whether the features observed arise from a C_3 carbon skeleton or from C_1 or C_2 fragments [3]. It is thought that fragmentation results in CH and C_2H fragments. The bands observed from annealing 3,3,3-trifluoropropylidyne have been assigned in terms of CF_3 and CF_2 species. The adsorption of these CF_x species have been studied by EELS on Pt (111) [11]. Adsorbed CF_3 is obtained either from the thermal dissociation of CF_3I or the photochemical dissociation from CF_3Br . They were assigned from comparison to CF_3 ligands in transition metal complexes [12]. In the same study the molecular adsorption of CF_3I and CF_3Br have been reported. These have been assigned from a comparison of the gas phase values [13] (table 3.7). In fig. 3.5 at 501 K most of the bands seen can be assigned to vibrational modes of CF_3 under the C_{3v} point group (see table 3.2). These are 1251 cm^{-1} (CF_3 symmetric stretch), 697 cm^{-1} (δCF_3 symmetric) and 230 cm^{-1} (Pt-C stretch). In comparison to the observed adsorbed CF_3 symmetric stretch [11] the same mode in the above

Table 3.7 Vibrational assignment of adsorbed CF₃I and CF₃Br [11] and comparison with assigned data from the spectra recorded from annealing 3,3,3-trifluoropropylidyne to 501 K

Assignment under C _{3v} point group	CF ₃ I adsorbed [11]	CF ₃ Br adsorbed [11]	CF ₃ Mn(CO) ₅ [12]	CF ₃ adsorbed [11]	Data from 501 K [This work]
ν CF ₃ (s)	1060	1130	1063	1060	1251
δ CF ₃ (s)	745	785	700	745	697
ν C-X	not observed	330			
ν CF ₃ (as)	1190	1235	1045	n.o	1147 ^a
δ CF ₃ (as)	540	505	555	n.o	616 ^a
C-X bend	not observed	n.o	n.o	n.o	
Pt-C stretch				270	230

^a Modes originating from 3,3,3-trifluoropropylidyne that has not decomposed.

assignment has a higher frequency, this could be due to the influence of other surface species. The modes at 1147 cm^{-1} and 616 cm^{-1} are assigned to the CF_3 asymmetric stretch and the $\delta\text{ CF}_3$ asymmetric associated with 3,3,3-trifluoropropylidyne. The remaining mode at 936 is probably due to C_2 fragments. At a temperature of 625 K there is evidence for the decomposition of the CF_3 group. From the study of CF_x species it is observed that there are two pathways that the reaction can follow, desorption of CF_3 radicals into the gas phase at high temperatures with a desorption rate maximum near 640 K , or decomposition with a loss peak observed at vibrational frequency of 1210 cm^{-1} . This has been assigned to the symmetric stretch of the CF_2 group. Therefore the features at 730 K have been assigned as 1196 cm^{-1} (CF_2 symmetric stretch) and 705 cm^{-1} ($\delta\text{ CF}_2$ symmetric). From the study above CF_2 radicals have been shown to desorb at temperatures above 750 K [11, 14]. From the spectra in fig. 3.9 it is clear that this species has either desorbed or decomposed to form a carbon covered surface at 873 K . Direct adsorption of 3,3,3-trifluoropropene at 730 K resulted in a spectrum with no features. It was expected that a layer of CF_2 would be formed giving rise to the same features as observed above. This indicates that more than one route exists and direct desorption of CF_3 competes more effectively than decomposition to CF_2 . Therefore direct desorption is favoured at higher temperatures.

Figure 3.12 The Proposed Decomposition Scheme of 3,3,3-trifluoropropylidyne on Annealing

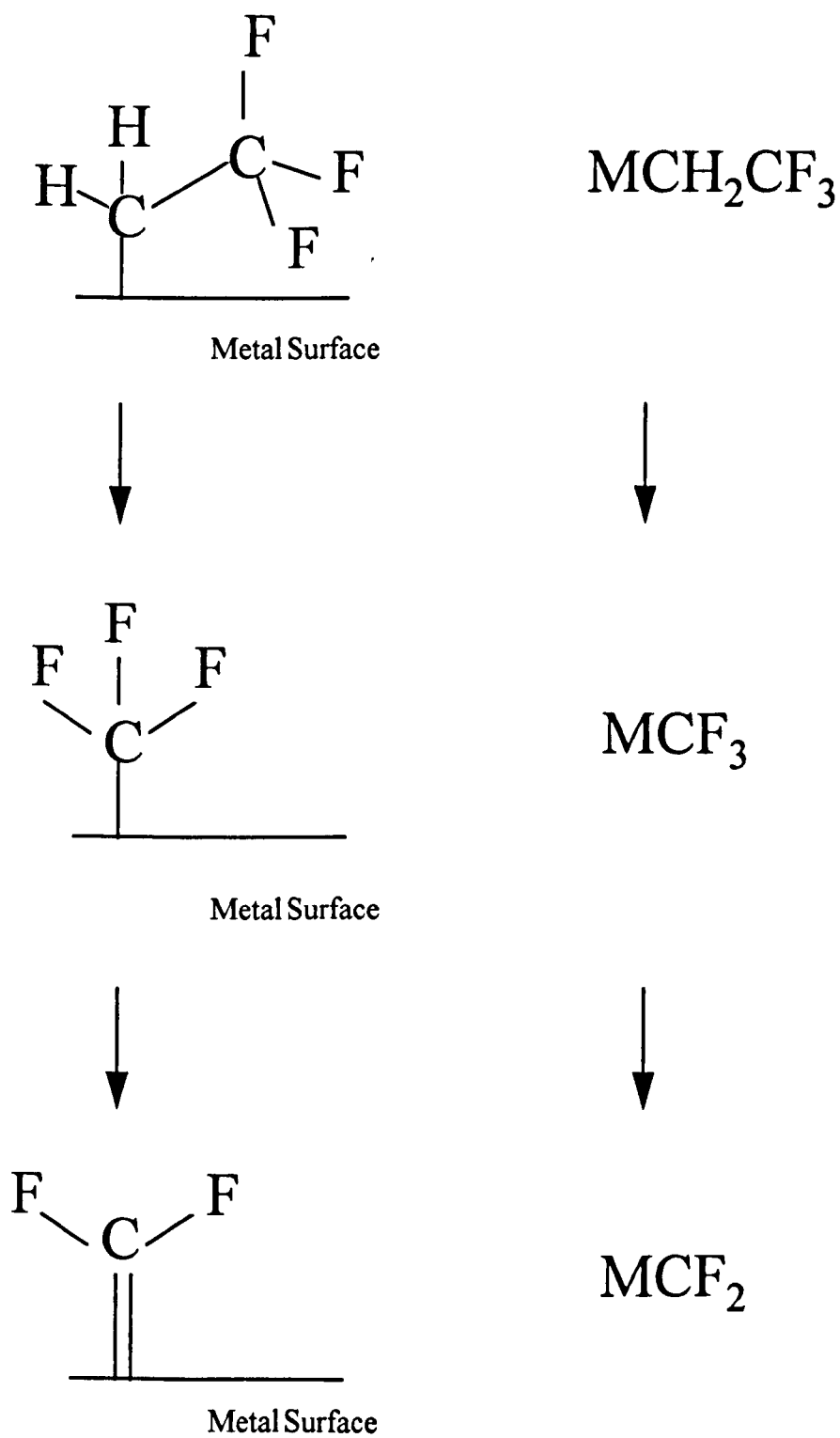


Figure 3.12 shows the decomposition scheme of 3,3,3-trifluoropropylidene. Above two main products are detailed, first the formation of CF_3 and then the subsequent decomposition to form CF_2 .

3.5 Comparison of EELS and RAIRS Intensities

The intensities observed in both of these vibrational spectroscopic techniques can be compared by relating the EELS relative intensity to the perpendicular dynamic dipole moment of the vibrational mode. Both News [15] and Ibach and Mills [16] have given equations which take into account the fact that the low energy loss peaks are relatively accentuated due to the narrow angular range of the lobe of dipole-scattered electrons which leads to more efficient collection by the analyser. The dipole moment achieved is an effective one including any image charge and screening effects.

News [15] derived the expression relating loss intensity to the dynamic dipole moment in EEL spectroscopy. It is given in atomic units, by Equation 3.1.

$$\frac{I_i}{I_0} = \frac{\pi n_s \mu^2}{E} \cos \alpha \left[(t^2 - 2)Y + (t^2 + 2) \ln X \right] \quad \text{Equation 3.1}$$

where n_s is the surface coverage, assuming a coverage of $\theta=0.25$ [17, 18], μ is the dynamic dipole moment, α is the angle of incidence = 60° , E is the energy of incident electrons = $6.5 \text{ eV} = 0.239$ atomic units.

The term $\cos\alpha[(t^2-2)Y+(t^2+2)\ln X]$ takes account of the angular spread of the dipole scattered electrons. The parameters t , X and Y are defined as follows,

$$t = \tan \alpha$$

$$Y = \frac{\Theta_1^2}{\Theta_1^2 + \Theta_0^2}$$

$$X = 1 + \left(\frac{\Theta_1}{\Theta_0}\right)^2$$

where Θ_1 is the semi-vertical acceptance angle of the analyser = 52.4 mrad. and $\Theta_0 = \omega_0/2E$ where ω_0 , is the loss energy = 144.6 meV ($\times 10^{-3} \times 8065 \text{ cm}^{-1}$).

Ibach and Mills [16] tabulate a parameter $F_s(\theta_c)$ which serves the same purpose with $(1-2\Theta_0)^{1/2}F_s(\theta_c)/\cos \alpha$ being equivalent to the above terms in the Newns model.

$$\theta_c \text{ is defined as } \left(\frac{\Theta_1}{\Theta_0}\right).$$

From the above equation we estimate a dynamic dipole moment of 0.49 D, given $I/I_0 = 0.038$. (The contribution estimated from a band identified in the RAIR spectrum at 1105 cm^{-1} has been deducted). Given the dynamic dipole moment from the EELS spectrum we can estimate the integrated absorbance of the corresponding band in a RAIRS spectrum.

The integrated absorbance in the RAIRS experiment is given by equation 3.2.

$$A = \int \ln\left(\frac{R_0}{R}\right) d\bar{\nu} = \frac{4\pi^2 \sin \alpha \tan \alpha \bar{\nu}}{c\hbar} \mu^2 \quad \text{Equation 3.2}$$

where A is the integrated absorbance (cm^{-1}), $\bar{\nu}$ is the wavenumber, c is the velocity of light (cm s^{-1}), α is the angle of incidence $=85^\circ$, n_s is the coverage (cm^{-2}) and μ is given in cgs units.

This is a modification of an expression given by Canning and Chesters [19] which applies to p-polarised light and gives an effective dynamic dipole moment including image dipole effects and the screening arising from the electronic polarisability of the adsorbed molecule.

Insertion of the value of $\mu = 0.49$ D calculated from the EELS result gives an integrated absorbance of 1.29 cm^{-1} . For the RAIRS band at 1164 cm^{-1} , half width $\sim 5 \text{ cm}^{-1}$ the integrated absorbance yields a peak absorbance of 0.2585 which corresponds to a 23% band. The band reported in fig. 3.10 has a value of 3.5 % transmittance.

Similarly for the RAIRS band at 1334 cm^{-1} , (which has an $I/I_0 = 0.013$) a value of $\mu = 0.305$ D calculated from the EELS result gives an integrated absorbance of 0.576 cm^{-1} . A band of half width 8 cm^{-1} yields a peak absorbance of 0.072 which corresponds to a 7% band. The band reported in fig. 3.10 has a value of 1.1 % transmittance.

The ratio of the intensities of the bands predicted agrees well with an approximate ratio of 3:1 from the RAIR spectrum, although the values themselves are 7 times larger. The discrepancy between the RAIRS and EELS intensities was unexpected as similar comparisons for carbon monoxide and hydrocarbon adsorbates have given agreement within ± 50

%. The ratio of the relative intensities (I/I_0) calculated for the symmetric deformation mode of the CH_3 group of ethylidyne (*ca.* 1339 cm^{-1}) to the elastic peak measured by the previous spectrometer ELS 22 [20] and the new ErEELS 31 spectrometer [21] was approximately 1:1. This was to check the accuracy of the acceptance angle of the new spectrometer. It is concluded that bands in the same region as the calculation above should give similar results to those achieved with the ELS 22 spectrometer, that is within $\pm 50\%$.

This may be resolved in the future with further understanding of the ErEELS 31 spectrometer, but at the moment a reason for the large discrepancy is not apparent.

3.6 Conclusions

This work has confirmed that 3,3,3-trifluoropropene reacts to form 3,3,3-trifluoropropylidyne at 360 K. Thus a route to modelling a CF_3 terminated amphiphile has been established.

The dynamic range and improved resolution of the EELS technique has enabled a more complete assignment of the surface vibrational species and subsequent decomposition path including intermediates. This has been accomplished by resolving bands that are too weak to be observed in the infrared over a wide spectral range which has resulted in a more complex spectrum than the RAIRS results.

Access to the low wavenumber region and the improved resolution of the new EEL spectrometer provide evidence of a phonon mode on Pt (111).

The sensitivity of the technique reveals unique features, for example the double excitation band.

3.7 References

- [1] S.R. Cohen, R. Naaman and J. Sagiv, *Phys. Rev. Letts.*, **58** (1987) 1208
- [2] S.R. Cohen, R. Naaman and J. Sagiv, *J. Chem. Phys.*, **88** (1988) 2757
- [3] N.R. Avery and N. Sheppard, *Proc. R. Soc. Lond.*, **A405** (1986) 1-25
- [4] M.A. Chesters, C.D. La Cruz, P. Gardner, E.M. McCash, P. Pudney, G. Shahid and N. Sheppard, *J. Chem. Soc. Faraday Trans.*, **86** (1990) 2757-2763
- [5] S. Andersson, B.N.J. Persson, M. Persson and N.D. Lang, *Phys. Rev. Letts.*, **52** (1984) 2073
- [6] J.A. Stroscio, M. Persson, S.R. Bare and W. Ho, *Phys. Rev. Letts.*, **54** (1985) 1428
- [7] Ch. Wöll, *Appl. Phys. A*, **53** (1991) 377-387
- [8] A. Savitzky and M.J.E. Golay in *Anal. Chem.*, **36** (1964) 160, described by G. Beech in 'Fortran IV in Chemistry', 239, (Wiley Chichester 1975)
- [9] G.A. Crowder and N. Smyrl, *J. Chem. Phys.*, **53** (1970) 4102
- [10] Q. Dai and A.J. Gellman, *J. Phys. Chem.*, **95** (1991) 9443-9448

- [11] D.D. Armentrout and V.H. Grassian, *Langmuir*, 10 (1994) 2071-2076
- [12] F.A. Cotton and R.M. Wing, *J. Organomet. Chem.*, 9 (1967) 511
- [13] P.R. McGee, F.F. Cleveland, A.G. Meister, C.E. Decker, S.I. Miller, *J. Chem. Phys.*, 21 (1953) 242
- [14] Z.M. Liu, X.L. Zhou, J. Kiss, J.M. White, *Surf. Sci.*, 286 (1993) 233
- [15] D. Newns in: 'Vibrational Spectroscopy of Adsorbates', Ed. R.F. Willis, (Springer-Verlag, 1980), pp 7-22
- [16] H. Ibach and D.L. Mills, 'Electron Energy Loss Spectroscopy and Surface Vibrations', (Academic Press, New York, 1982).
- [17] I.V. Mitchell, W.N. Lennard, K. Griffiths, G.R. Massoumi and J.W. Hupertz, *Surf. Sci.*, 256 (1991) L598
- [18] K. Griffiths, W.N. Lennard, I.V. Mitchell, P.R. Norton, G. Pirug and H.P. Bonzel, *Surf. Sci.*, 284 (1983) L389
- The coverage of the 3,3,3-trifluoropropylidyne layer is assumed to be the same coverage as ethylidyne in references [17,18]
- [19] N.D.S. Canning and M.A. Chesters, *J. of Electron. Spectrosc. and Related Phenom.* 29 (1983) 69-76
- [20] Y.H. Saoud PhD Thesis UEA 1991
- [21] E.C. Hargreaves, unpublished results

Chapter Four

The Adsorption of CO on Cu (111) using Synchrotron Radiation RAIRS

4.1 Introduction : Extending the Spectral Range of RAIRS

4.2 Far-infrared RAIRS

4.3 Background

4.3.1 The Vibrational Motions of Adsorbates at Surfaces

4.3.2 Carbon monoxide : A Simple Adsorbate

4.4. Synchrotron Radiation RAIRS Studies

4.4.1 The Detection of Parallel Modes : Experimental Evidence and the 'Anti-absorption' Feature

4.5 A Mechanism to Describe the 'Anti-absorption' Feature

4.6 Experimental

4.6.1 Data Manipulation

4.6.2 Experiment I. Incident Angle of 87°

4.6.3 Experiment II. Incident Angle of 20°

4.7 Discussion

**4.8 Alternative Mechanisms to Describe the Observation of
Parallel Modes**

4.9 Summary

4.10 Conclusions

4.11 References

4.1 Introduction : Extending the spectral range of RAIRS

A number of approaches have been taken to overcome the obstacle that the low intensity of blackbody sources in the region from 600-200 cm^{-1} presents for RAIRS experiments. One approach has been to use emission infrared spectroscopy. Chiang *et al* [1] used a liquid-helium-temperature grating spectrometer with a Si:Sb photoconductive detector to observe the carbon-metal stretch for CO/Ni (100). In the same way Tobin *et al* [2] have recorded the carbon-metal stretch for CO/Pt(111). Brown *et al* [3] have developed a high sensitivity emission spectrometer which incorporates a liquid-helium-cooled FTIR spectrometer, a liquid-helium-cooled path and a Cd-doped Ge bolometer. As the liquid-helium-cooled path will cut down the stray light problems encountered by Chiang *et al* [1], it is expected to give a greater degree of sensitivity. Recently, instrumental developments in RAIRS using standard sources have enabled several groups to extend the spectral range down to 440 cm^{-1} . In particular measurements of the *on-top* carbon-metal stretch vibration for CO on Pt (111) have been reported by Hoge *et al* [4] using a Cu:Ge photoconductive detector. Malik *et al* [5] have detected the same mode on Pt (111) using a liquid helium cooled bolometer. Persson *et al* [6] and Ryberg [7] have also studied this mode. The Pt-CO stretch vibration of *bridge-bonded* CO on Pt (111) is the most recent study to be reported by Engström *et al* [8], using a Cu:Ge detector. Wang *et al* [9] have recorded the O/Ag vibration at 351 cm^{-1} on polycrystalline silver foils using a Si

bolometer detector. Peng *et al* [10] used an evacuated FTIR and a He-cooled detector to record the O-Ag symmetric stretch at 335 cm^{-1} for O/Ag (110). The noise associated with thermal fluctuations and instabilities (extrinsic to the source) and the low intensity of black-body sources in this region used for these experiments have so far limited the ultimate signal-to-noise achievable.

An alternative approach is to use a source which is intense in the low wavenumber region. Tunable solid-state dye lasers have been used by Bermudez *et al* [11] to record the Al-O stretching modes of oxygen on Al (111). Surface (580 cm^{-1}) and sub-surface (890 cm^{-1}) Al-O stretching modes at sub-monolayer coverage have been observed. Hoffman *et al* [12] used a pulsed tunable dye laser with a Raman scattering cell to record the RAIR spectrum of CO adsorbed on Ru (001) in the 2050 cm^{-1} region. The disadvantages of using lasers are mainly due to the fact that each laser can only be tuned over a few hundred wavenumbers, necessitating the use of a series of lasers tunable over the entire wavenumber range. Laser stability has limited the signal-to-noise performance and it is hoped that improvements in electronics and experimental set-up will enhance the levels attainable in the future.

4.2 Far-infrared RAIRS

Synchrotron radiation can be used for research in the regions of the spectrum which have lacked sufficiently brilliant sources [13]. Synchrotron

radiation is a strong source of electromagnetic radiation which has a continuous spectrum extending from the IR to the X-ray region. One of the regions that has conventionally lacked source intensity is on the borders of both the mid and far IR regions, 1000-200 cm^{-1} .

The standard source of radiant energy for IR spectrometers is the Globar, whose energy distribution is that of a conventional blackbody source. The emitted energy distribution, $\rho(\nu)$ of a blackbody is given by the Planck distribution, equation 4.1.

$$\rho(\nu) = \frac{8\pi h \nu^3}{c^3} (\exp \frac{h\nu}{kT} - 1)^{-1} \quad \text{Eqn 4.1}$$

Fig 4.1 shows how the output of a blackbody varies with increasing temperature and wavenumber. A section of this graph including only the wavenumbers of interest has been expanded fig 4.2 [14]. It is apparent that at lower wavenumbers the intensity of a blackbody is greatly reduced. To increase this intensity to sufficiently high values the black body would have to reach incredibly high temperatures ($> 90\,000\text{ K}$) which are not physically feasible.

Synchrotron radiation is generated in a sweeping searchlight pattern. The small beam dimensions and high degree of collimation result in extreme source 'brilliance' and polarisation in the plane of the orbit. (Brilliance is defined as the number of photons emitted per second per unit frequency interval per unit area of source per unit solid angle).

The frequency at which the synchrotron will begin to offer an intensity advantage over a blackbody source is dependent on the

Figure 4.1 Curves for the Energy Density [energy per unit volume per unit frequency interval ($\text{J m}^{-3} \text{ s}$)] of a Blackbody Source at Various Temperatures [14]

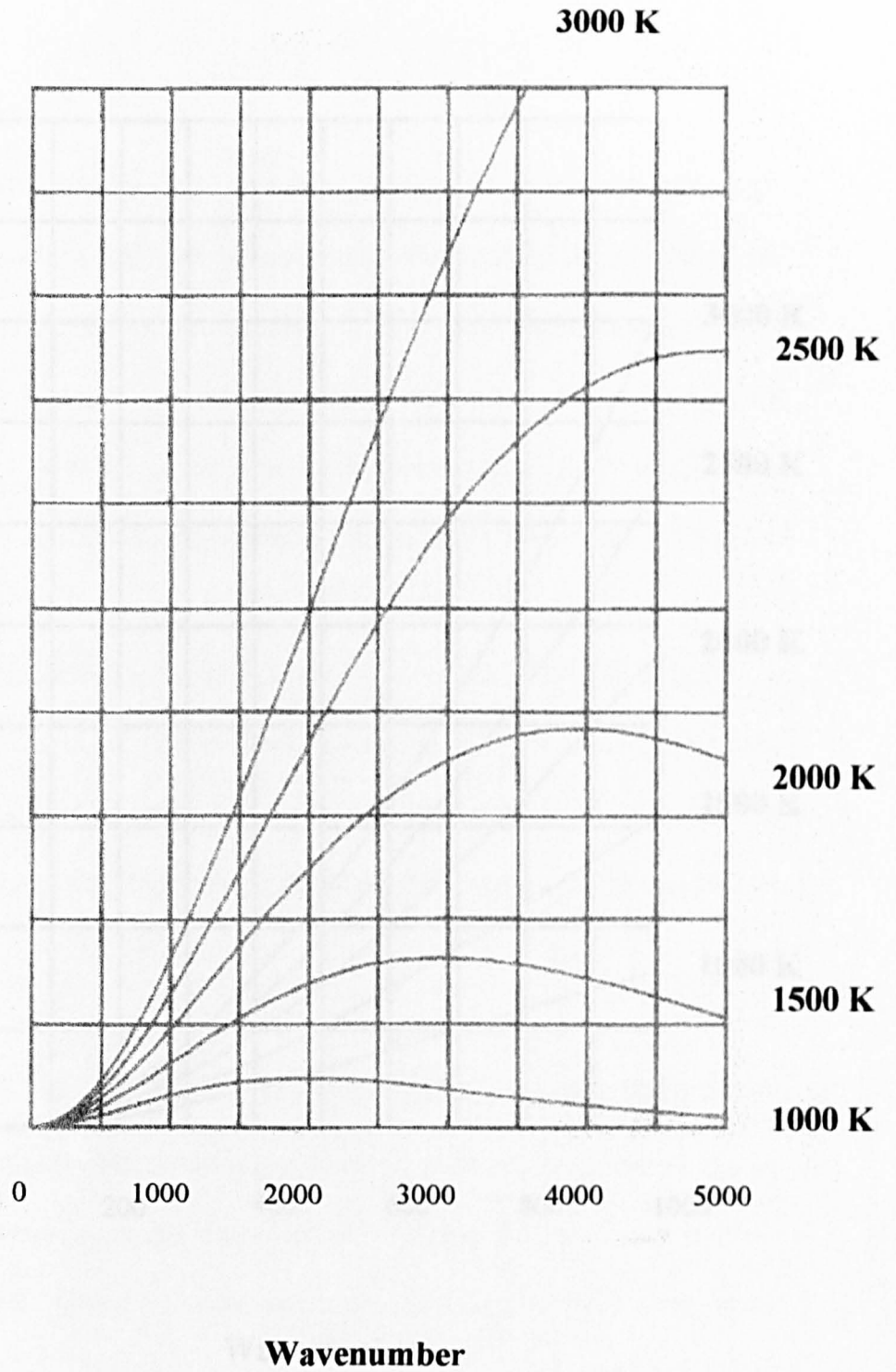
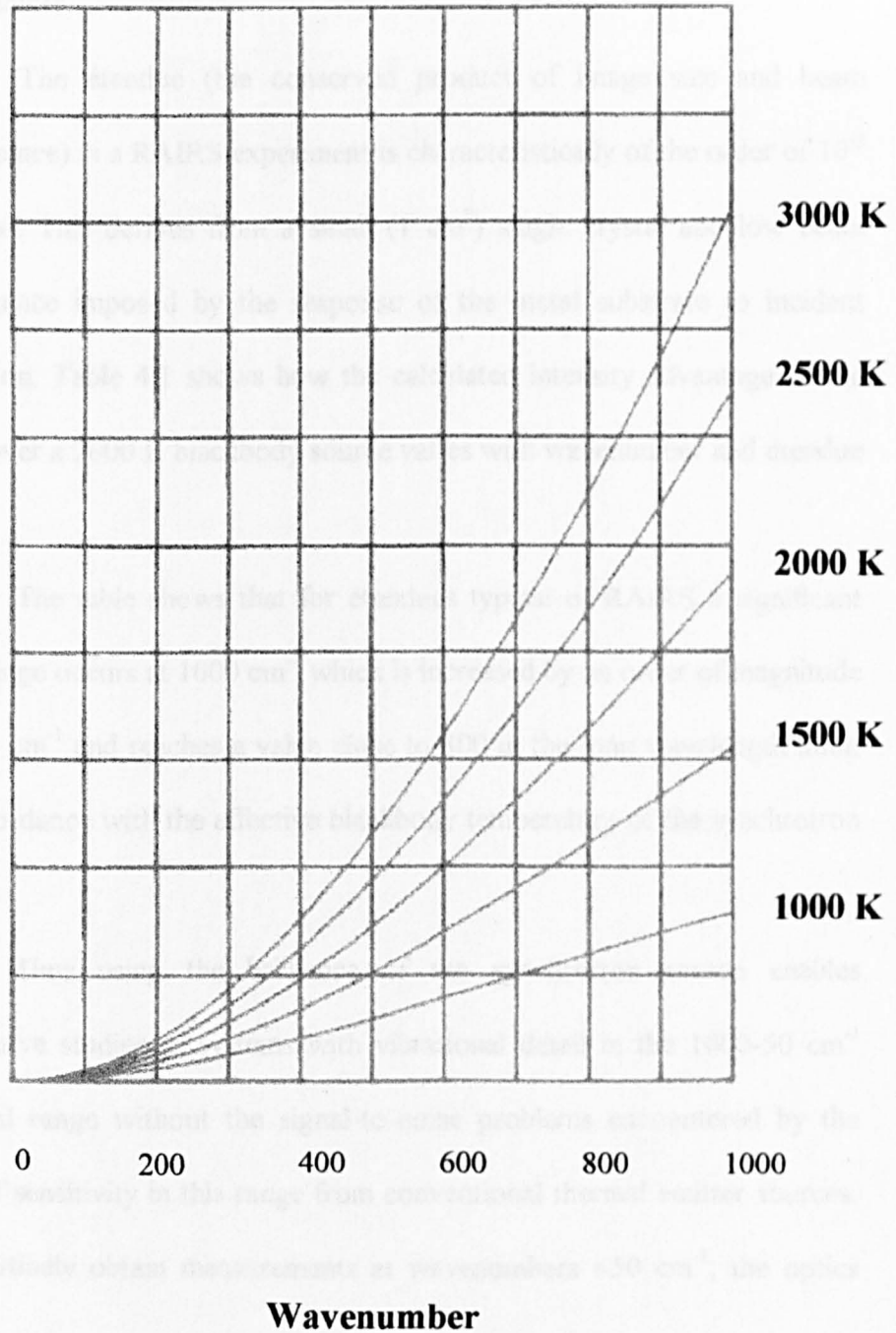


Figure 4.2 The Energy Densities of a Blackbody Source ($\text{J m}^{-3} \text{ s}$) for Increasing Temperatures in the region $< 1000 \text{ cm}^{-1}$ [14]

x 5



dimensions of the limiting aperture in the optical system. When the effective aperture size (spectrometer throughput) is large then the power output of the synchrotron only exceeds that of a blackbody at very long wavelengths. However if the limiting aperture is made smaller, then the intensity advantage of synchrotron radiation is realised at higher frequencies.

The étendue (the conserved product of image size and beam divergence) in a RAIRS experiment is characteristically of the order of 10^{-2} mm² sr. This derives from a small (1 cm²) single crystal and low beam divergence imposed by the response of the metal substrate to incident radiation. Table 4.1 shows how the calculated intensity advantage of the SRS over a 2000 K blackbody source varies with wavenumber and étendue [15].

The table shows that for étendues typical of RAIRS a significant advantage occurs at 1000 cm⁻¹ which is increased by an order of magnitude at 330 cm⁻¹ and reaches a value close to 300 in the long wavelength limit, in accordance with the effective blackbody temperature of the synchrotron source.

Thus using the brilliance of the synchrotron source enables qualitative studies of systems with vibrational detail in the 1000-50 cm⁻¹ spectral range without the signal-to-noise problems encountered by the lack of sensitivity in this range from conventional thermal emitter sources. To routinely obtain measurements at wavenumbers <50 cm⁻¹, the optics

Table 4.1 Relative Intensity of the Daresbury SRS in Comparison with a 2000 K Blackbody as a Function of Wavenumber and Experimental Étendue [15].

Étendue / mm ² sr	Wavenumber / cm ⁻¹					
	3300	1000	330	100	33	10
10 ⁰	0.01	0.05	0.34	3.4	29	230
10 ⁻¹	0.12	0.48	3.4	34	290	
10 ⁻²	1.2	4.8	34	340		
1.6 x 10 ⁻³	7.8	30	200			
3.5 x 10 ⁻⁴	36	138				
10 ⁻⁴	120					

4.3 Background

4.3.1 The Vibrational Motion of Adorbates at Surfaces

A polyatomic molecule in the gas phase has three Cartesian coordinate vectors assigned to each of the N atoms in the molecule, resulting in 3N degrees of freedom for an N-atom species. For a non-linear species, three are translations, three are rotations and 3N-6 are vibrations. For a linear species, there are only two degrees of rotational freedom as rotation

would need to be re-designed to continually refocus the beam due to the diffractive spreading of the synchrotron beam at such low wavenumbers.

This region contains most of the molecule-substrate vibrations and hence information about the chemical bond between the adsorbed molecule and the metal substrate. It is of particular importance for atomic adsorbates such as O, C, N and Cl, where the substrate-adsorbate bond is the only bond present. The stretching modes of heavy atoms (halogens and organometallics) employed in semiconductor doping and device fabrication, surface phonons and the coupling interactions with adsorbed species together with deformation modes, including frustrated rotations and translations are all areas that have been investigated with EELS in this spectral range. RAIRS studies offer the possibility of advancing the understanding in these areas with higher resolution and higher pressure measurements.

4.3 Background

4.3.1 The Vibrational Motions of Adsorbates at Surfaces

A polyatomic molecule in the gas phase has three Cartesian coordinate vectors assigned to each of the N atoms in the molecule, resulting in $3N$ degrees of freedom for an N -atom species. For a non-linear species, three are translations, three are rotations and $3N-6$ are vibrations. For a linear species, there are only two degrees of rotational freedom as rotation

of the nuclei about the axis of the molecule is impossible as they all lie on the axis, therefore there are $3N-5$ vibrations. The dipole active vibrations require a non-zero dipole moment change associated with the vibration [16-18].

In the case of the adsorbed molecule, the number of vibrational modes is determined by the number of internal modes ($3N-6$) together with the number of frustrated rotational and translational modes. These modes are determined by the symmetry of the adsorption site. This is illustrated below for the case of CO on Cu (100) in fig. 4.3.

There is one internal mode, the C-O stretching vibration ν_1 , and five external modes, the frustrated translation perpendicular to the surface ν_2 (M-CO stretch), the 2-fold degenerate frustrated rotation ν_3 , (M-CO bend) and the 2-fold degenerate frustrated translation parallel to the surface ν_4 . 'Frustrated' refers to the restricted motion of the mode when it is bonded to the surface. If the molecules are adsorbed in the linear on-top site then according to the metal surface selection rule only the modes with a dipole change perpendicular to the surface or modes with A_1 symmetry should be observed. This means that ν_1 and ν_2 are allowed and ν_3 and ν_4 are forbidden.

4.3.2 Carbon monoxide : A Simple Adsorbate

Carbon monoxide (CO) has been widely employed as a probe molecule in studies to characterize the metal substrate [19]. Specifically,

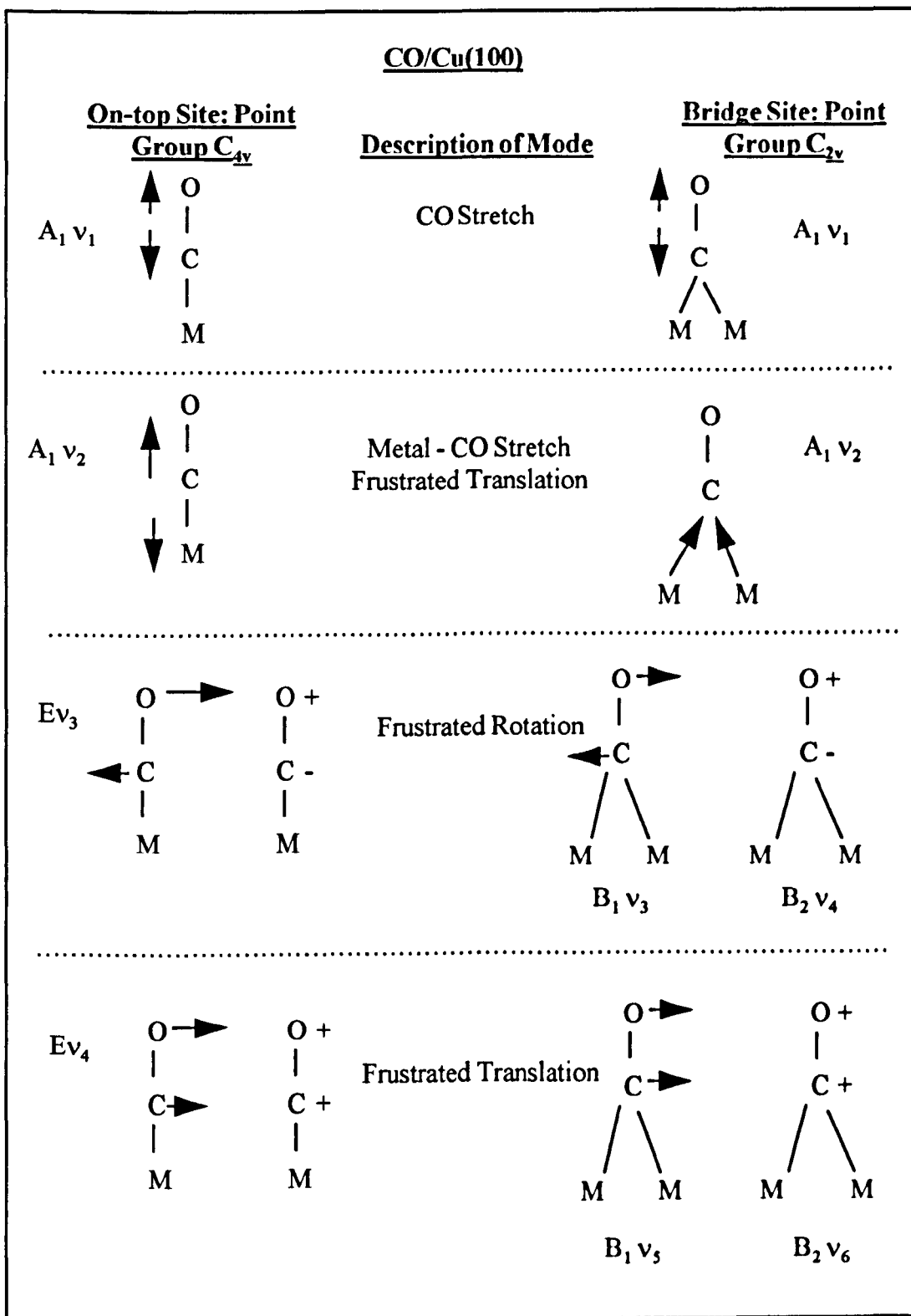


Figure 4.3. The Normal Mode Vibrations for CO Adsorbed on a Metal (M) in an On-top site with Four-fold Rotational Symmetry (Left side) and in a Bridge site with Two-fold Rotational Symmetry (Right side).

carbon monoxide has a very high absorption coefficient associated with the C-O stretching mode and the vibrational frequency is sensitive to the nature of the adsorption site on the surface. In the days when sensitivity was a major problem it was therefore particularly easy to study.

The reason for the sensitivity is due to the type of bonding interaction involved at the metal's surface. A molecular orbital description developed by Blyholder [20] of the chemical interaction is shown in fig. 4.4.

CO is a π acid ligand whose bonding is interpreted in terms of a synergic interaction between σ donation from the 5σ molecular orbital of CO into the metal and π backdonation from the metal to the $2\pi^*$ molecular orbital of CO. The bonding is strong with transition metals as the drift of the π electron density from the metal to carbon tends to make the ligand more negative and so increases its σ -donor power. Back donation, however, into antibonding CO orbitals weakens the CO bond. The interatomic CO distance increases resulting in a decrease in the C-O force constant and there is a decrease in the infrared frequency. Hence the greater number of metal atoms the CO is bonded to, the greater the backdonation contribution and the lower the stretching frequency becomes. Sheppard *et al* [20] have detailed the frequencies associated with different adsorption sites from a comparison of the observed band frequencies with those obtained in vibrational studies of carbonyl compounds. Fig. 4.5 shows how the frequency of the CO stretching vibration varies for different adsorption sites.

Figure 4.4 A molecular orbital representation of the M-CO bonding [20]

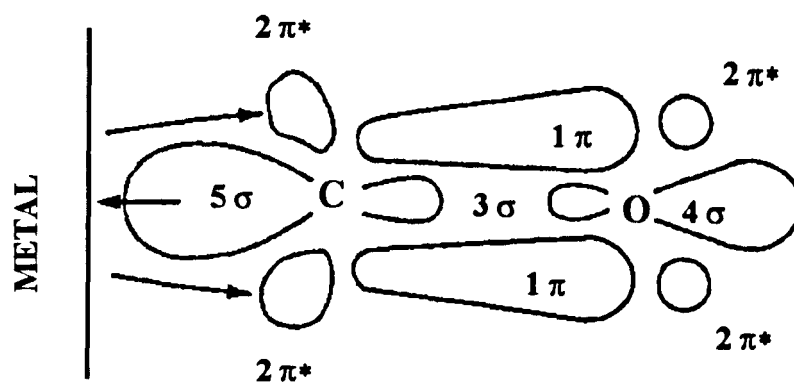
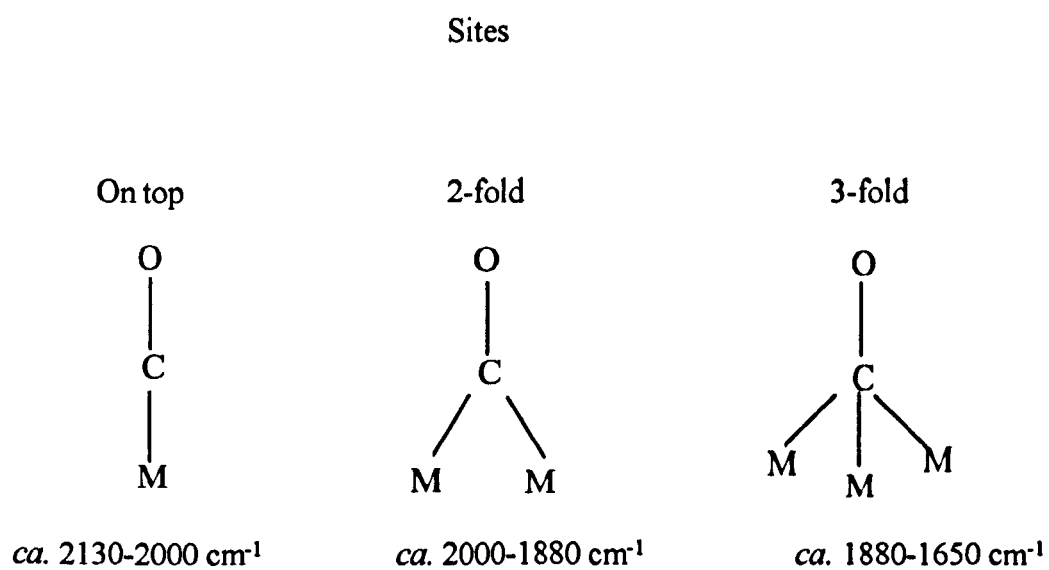


Fig. 4.5 The Change in the C-O Stretching Frequency Associated with Different Adsorption Sites [20]



RAIRS can therefore determine the adsorption site and the symmetry of the surface molecule. Furthermore, if the adsorbed overlayer is ordered and CO adsorption is site specific (i.e. it prefers one of the above configurations) then Low Energy Electron Diffraction (LEED) can be used as a complementary technique in determining the bonding configuration of the adsorbate. The use of LEED allows us to relate the vibrational spectra to the structure of the CO adlayer, especially at different CO coverages when the type of site occupied and thus the vibrational frequency may change [16-18]. However, caution is needed and invariably data from other techniques can sometimes lead to a re-interpretation of the nature of the bonding site.

It is possible due to the spectral range of EELS to observe low frequency modes, though due to the poor resolution of this technique they may be poorly resolved or even unresolved features. The importance of the RAIRS technique in detecting low frequency modes would mean better resolution measurements in comparison to EELS, and the exploitation of the selection rules governing each technique and the possibility of high pressure measurements.

4.4. Synchrotron Radiation RAIRS Studies

The bulk of the work involving synchrotron radiation as a source for the RAIRS experiment has been carried out at the National Synchrotron Light Source (NSLS) at Brookhaven. Hirschmugl *et al* have

measured the low frequency spectrum of CO on Cu (100) and Cu (111) [22-25]. They observed the metal-carbon stretch of the on-top CO at 345 cm^{-1} on Cu (100) and 347 cm^{-1} on Cu (111), as expected for a stretch that has a dynamic dipole perpendicular to the surface. An 'anti-absorption' feature was also present at 285 cm^{-1} on Cu (100) and 277 cm^{-1} on Cu (111). These features were unexpected. They assigned this anti-absorption feature to the frustrated rotation mode of the CO molecule with the aid of isotopic substitution experiments. This feature was accompanied by a broad-band absorption. The frustrated rotation has a dynamic dipole moment parallel to the surface and according to the metal surface selection rule is not expected to interact with the electric field generated by the infrared radiation. Similar features have also been observed for the frustrated rotation of NO on Cu (111) at 328 cm^{-1} by Hirschmugl *et al* [24]. Lamont *et al* [26] have recorded the spectrum of hydrogen on Cu (111) and an 'anti-absorption' band at 770 cm^{-1} has been assigned to the dipole forbidden frustrated translation modes of H atoms adsorbed in three-fold hollow sites.

The appearance of the dipole forbidden modes and broad-band absorptions have received significant attention in order to explain their origin. Volkitin and Persson [27] have developed a theory in which the anti-absorption peaks as well as the background changes induced by adsorbates are related, mediated by the current generated by the metal conduction electrons induced by a finite parallel electric field component in an indirect interaction.

The development of this theory from the experimental data is discussed below.

4.4.1 The Detection of Parallel Modes : Experimental Evidence and the 'Anti-absorption' Feature

Hirschmugl *et al* [23] noted that the hindered rotational at 285 cm^{-1} for CO/Cu (100) has been observed in specular EELS data by Andersson [28], but only for the compressed overlayer of CO having a coverage of $\Theta = 0.57$. EELS measurements of Uvdal *et al* [29] show a feature between 34 and 36 meV ($275\text{-}290\text{ cm}^{-1}$) only with the appearance of a $c(7\sqrt{2}\times\sqrt{2})\text{-R}45^\circ$ pattern, i.e. for a compression above $\Theta = 0.5$ ML. It was assumed that the dipole activity was related to the site symmetry of the $7\sqrt{2}\times\sqrt{2}$ cell. Hirschmugl *et al* [23] conducted measurements at a series of coverages, and observed that the mode is present through the entire coverage range, so it could not be related to the compression structure. Raval *et al* [30] have reported a band at 293 cm^{-1} for CO/Cu (111) in specular EELS measurements. LEED showed these EELS spectra to cover a range which begins near the $(\sqrt{3}\times\sqrt{3})\text{ R}30^\circ$ structure and extends to the $(1.5\times 1.5)\text{ R}18^\circ$ structure, i.e. at a coverage range of $\Theta = 0.33\text{-}0.44$. They assigned this to the frustrated rotation of the adsorbed molecule which would become dipole active if the CO was in a tilted configuration. Again, measurements by Hirschmugl *et al* [23] found the anti-absorption resonance at a range of coverages. In addition the modes on both surfaces were checked by

Hirschmugl *et al* [23] in order to determine which site was occupied. This was accomplished by examining the C-O stretching region. This confirmed that the CO was positioned on-top. In the case of CO/Cu(111) the anti-absorption resonance grows linearly with the occupancy of atop sites, but does not increase further in intensity as the bridge sites become occupied.

They argue that together with the CO experiments, the recent experiments of NO/Cu(111) (in which the NO bonds *via* the N atom) where the adsorption site of the NO is not clearly defined, the presence of an anti-absorption feature indicates that the infrared activity of the mode must be due to a general mechanism. They rule out a defect site C-metal mode by isotopic substitution and that an electro-polished crystal surface utilised in subsequent experiments resulted in a sharper feature [31,32].

4.5 A Mechanism to Describe the ‘Anti-absorption’ Feature

The emphasis of the following discussion and subsequent experiments is on the involvement of the parallel electric field in a mechanism differing from that leading to the metal surface selection rule which arises from the field perpendicular to the surface.

An incident p-polarized beam with electric vector amplitude E_p^0 gives rise to a component $E_{p\perp}$ (incident) perpendicular to the surface and a component $E_{p\parallel}$ (incident) parallel to the surface. The phase change for the p-polarized radiation varies strongly with the angle of incidence. The phase

change remains small until at high angles of incidence it changes rapidly to 180° .

At small angles of incidence the parallel components of the incident and reflected (E_p^i) beams are large, similar in magnitude but opposite in direction giving a small parallel field $E_{p\parallel}$. The perpendicular components combine constructively, at small angles of incidence the perpendicular field $E_{p\perp}$ is small but increases as the angle of incidence increases towards a maximum before the increasing phase difference eventually causes mutual cancellation and therefore falls to zero at grazing incidence. The resultant fields $E_{p\parallel}$ and $E_{p\perp}$ may be depicted as the major and minor semi-axes of an elliptical standing wave this is illustrated in fig. 4.6. At the optimum angle of incidence, when the amplitude of $E_{p\perp}$ is almost twice the magnitude of the incident field amplitude E_p^0 the significant field is perpendicular to the surface. This can interact with vibrational modes of adsorbates that have a component of the dynamic dipole moment oriented in the same direction. This is the phenomenon which leads to 'the metal surface selection rule' [33-35].

At the optimum angle of incidence for the metal surface selection rule mechanism ($\sim 87^\circ$) the amplitude of the parallel field is almost completely suppressed due to the destructive interference of the incoming and outgoing waves resulting in a node at the surface. It is not completely suppressed because the wave penetrates a distance into the surface. A collective parallel drift motion of the electrons just inside the metal surface is induced. Interaction of parallel vibrational modes of adsorbates with this

Figure 4.6 a The Resultant Normal and Tangential Components of the Surface Field of P-polarised Radiation

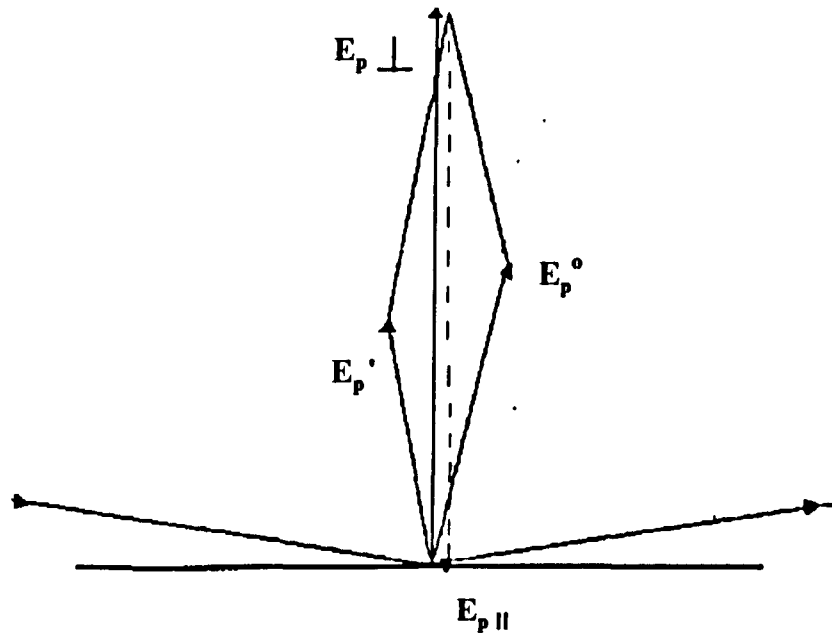
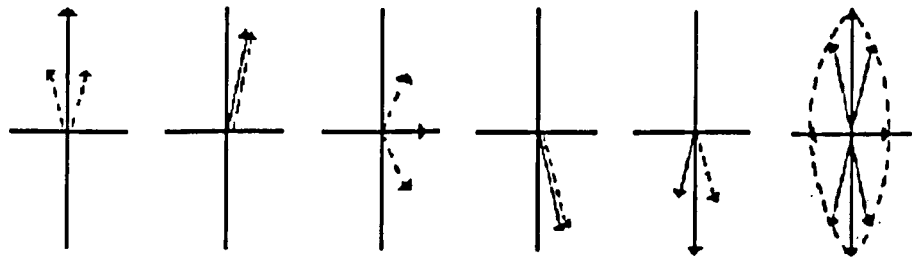


Figure 4.6 b The Sum of the Incident and Reflected E Vectors shown in a) for a Reflection Phase Shift of 90°



current density can produce a change in the reflectivity of the surface. This change, associated with modes not excited by the metal surface selection rule mechanism (*e.g.* frustrated rotations) can be seen as an anti-absorption feature in the RAIRS spectrum.

The theoretical treatment of a thin metallic film with a layer of adsorbed molecules has been treated by McIntyre and Aspnes, fig. 4.7 [36]. This results in expressions for the reflectivity change ΔR at an adsorbate covered surface. ΔR is the difference of the reflectivity of the clean surface (R_0) and the reflectivity of a layer of adsorbed molecules on a metal surface (R). The ratio of ΔR to R_0 gives the absorbance of an absorption band (A) in a RAIRS spectrum. Eqn. 4.2.

$$\frac{R_0 - R}{R} = \frac{\Delta R}{R_0} = A \quad \text{Eqn. 4.2}$$

This occurs when ΔR is small and $\ln\left(\frac{R_0 - R}{R}\right) \cong \frac{\Delta R}{R_0}$. A 'dip' is seen in the reflectance spectrum at those energies which correspond to vibrational excitations of the adsorbed molecule. This is the case for the metal surface selection rule mechanism involving the perpendicular field. See fig. 4.8.

The change in reflectivity resulting from an interaction involving the parallel field is due to a different mechanism. The parallel electric field of the incident infrared beam will induce a current in the metallic film due to the collective drift motion of the electrons. The electrons experience a resistance in their motion when they are inelastically scattered. The presence of the adsorbed layer of molecules results in an increase of the

Figure 4.7 Three Phase Model for Reflection of Light at a Surface Covered with an Adsorbed Layer [35]

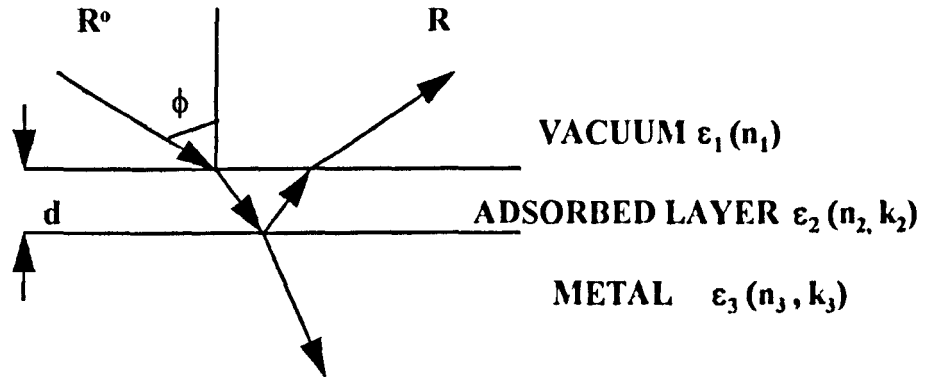
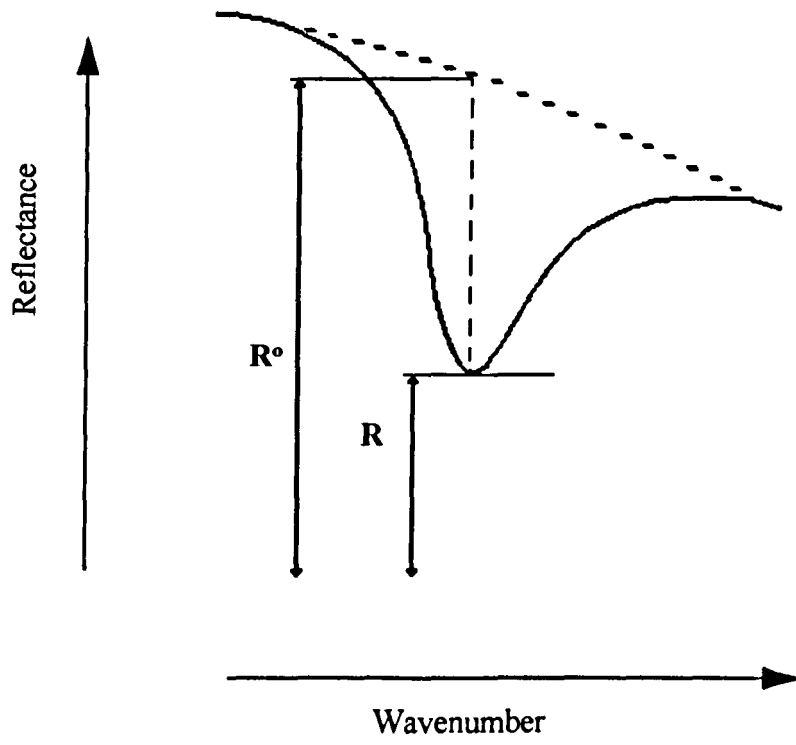


Figure 4.8 Definition of $\Delta R / R^0$



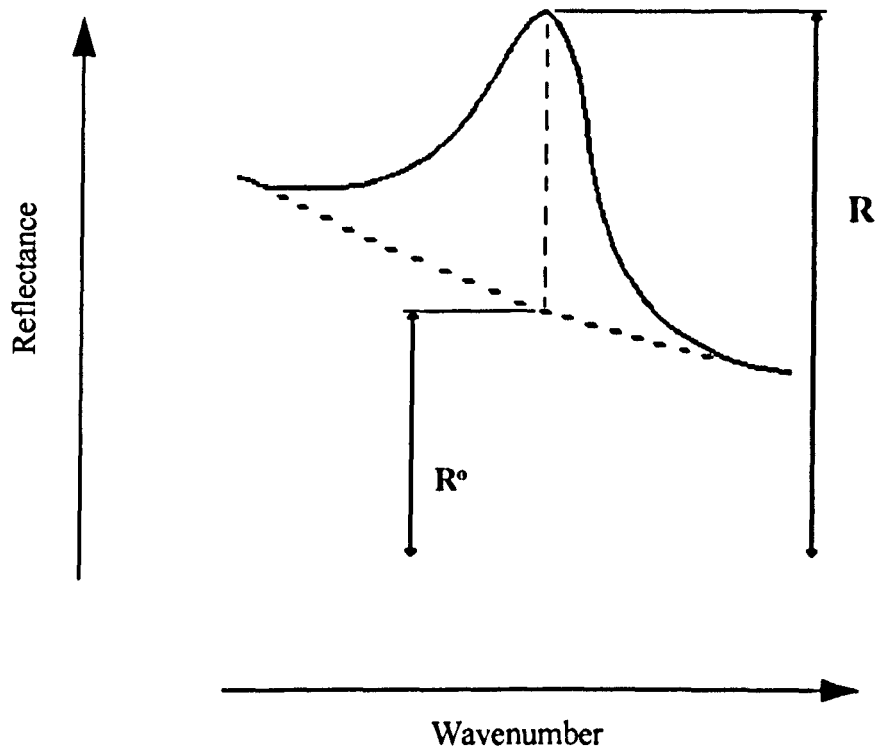
$$\Delta R = R^0 - R$$

resistance the electrons experience and hence in a uniform background absorption which depends upon the number of adsorbed molecules. The electrons are scattered off the nuclei of the adsorbed molecules and as the resistance increases thus the conductivity decreases and as the metal reflectivity depends directly on the conductivity the overall effect is a decrease in the reflectivity and hence a broadband absorption is observed.

If a parallel vibrational mode of an adsorbate on the metal surface (*e.g.* a frustrated rotation), has the same frequency parallel to the surface as the collective parallel drift motion of the electrons just inside the metal surface, the motions can indirectly couple to one another at this resonant frequency. The additional resistance incurred by the electrons due to the adsorbate disappears. Therefore the conductivity (and the reflectivity) returns to the value it had in the absence of the adsorbate. This results in an anti-absorption band, so called as the reflectivity increases. See fig. 4.9.

The incoming parallel field is the dominating field for this interaction. At the angle of incidence (87°) used for RAIRS the component of this field is small compared to the perpendicular field, but is still large enough for the occurrence of an anti-absorption band. At near-normal angles of incidence the ratio of the incoming parallel electric field $E_{p\parallel}$ to that of the incoming perpendicular electric field $E_{p\perp}$ will be significantly increased (this is the amplitude before the interaction with the metal surface). This fact formed the basis of the experiment used to explore the involvement of the parallel electric field.

Figure 4.9 An Increase in the Reflectance Resulting in an Anti-absorption band



4.6 Experimental

The experiment of Hirschmugl *et al* [23], of CO adsorbed on Cu(111) was carried out using incoming light at two different angles of incidence. These were : I) 87° , typical of a RAIRS experiment and II) 20° , a near-normal angle.

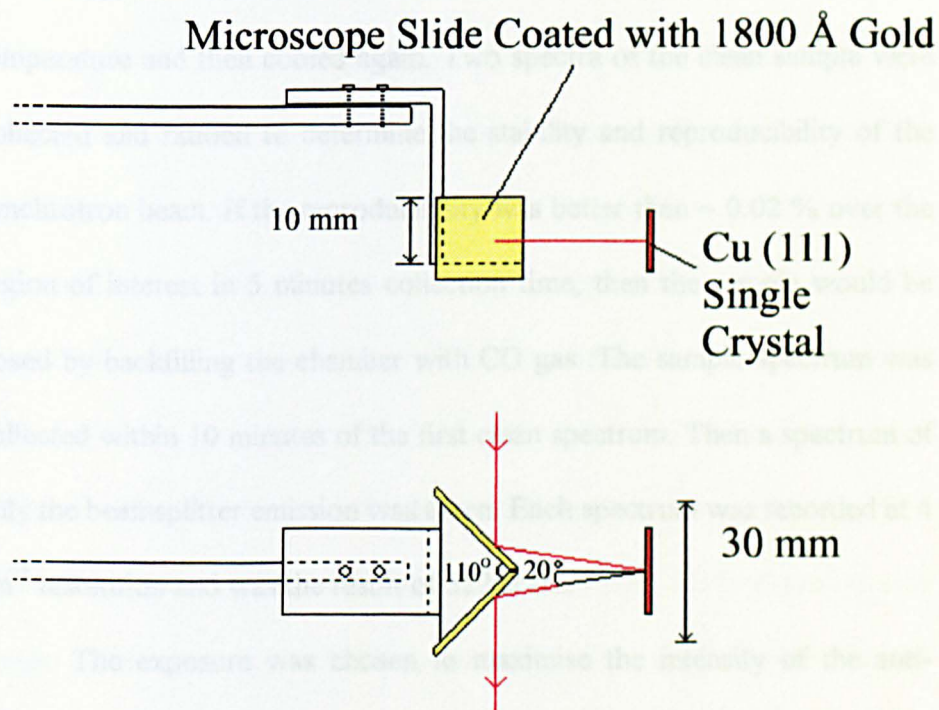
In order to accomplish the task of reflecting the light off the sample at normal incidence, a drive was designed by Chesters [37]. This is shown in fig. 4.10. In theory the straight through beam is reflected off an isosceles triangle to which mirrors are attached, onto the sample. The reflected light is reflected back off the triangle and continues on a straight through path. The angle of the incident light on the crystal was designed to be 20° and the distance from the parallel path of the light to the sample was 23 mm. In practice this distance was 10 mm as the crystal position was moved to the limit of the x direction travel. This limited the increase in the amount of available light which was expected from this configuration.

The mirror arrangement consisted of a piece of 10 mm thick aluminium shaped into an isosceles triangle with a vertex angle of 110° and a base length of 30 mm, to which two pieces of microscope coverslip (coated with c. 1800 \AA of gold film in an evaporating chamber) were attached. This piece was screwed onto an L-shaped copper strip which was attached *via* two screws to a UHV linear drive (Caburn-MDC) which had an overall travel of 50.8 mm. The copper section was necessary

leave the part through which the wire carried the 100 V current was
water than the level at which the experimenters light impinged on the crystal.

The Cu (111) crystal cleaning procedure has been described in

Figure 4.10 A Schematic Diagram of the Drive used to Reflect the Light off the
Sample at Near-normal Incidence



since the port through which the drive entered the UHV chamber was higher than the level at which the synchrotron light impinges on the crystal.

The Cu (111) crystal cleaning procedure has been described in section 2.7.5. Following annealing, the crystal was cooled to 120 K. The LEED pattern of the cleaned surface showed a hexagonal mesh after cooling and Auger spectroscopy did not detect any impurities. To minimize the background absorption of CO, the crystal was flashed to room temperature and then cooled again. Two spectra of the clean sample were collected and ratioed to determine the stability and reproducibility of the synchrotron beam. If the reproducibility was better than $\sim 0.02\%$ over the region of interest in 5 minutes collection time, then the sample would be dosed by backfilling the chamber with CO gas. The sample spectrum was collected within 10 minutes of the first clean spectrum. Then a spectrum of only the beamsplitter emission was taken. Each spectrum was recorded at 4 cm^{-1} resolution and was the result of 512 scans.

The exposure was chosen to maximise the intensity of the anti-absorption band. From the Hirschmugl data [23] this occurred at the 0.3 monolayer $\sqrt{3}\times\sqrt{3}$ R30° structure. LEED measurements were therefore essential in obtaining this structure and to maximise the anti-absorption mode. Unfortunately due to technical and electrical problems, LEED measurements could not be carried out as hoped. Thus a series of exposures helped to define an appropriate dose in the RAIRS (87°) experiment, where the intensity of the Metal-Carbon (M-C) stretching band

was maximised. This dose was then used in all subsequent experiments and 'near-normal' incidence experiments for comparison.

4.6.1 Data Manipulation

The noise on the background and sample spectra contained regular oscillating elements confirmed by the presence of sidebands in the interferograms. Fig. 4.11. The origin of these features is uncertain. It is thought that the sidebands either side of the centreburst at 1774 and 794 data points (the maximum occurs at 1284 data points) result from the bolometer and the ones at intervals at approximately 3293, 5310 and 7326 data points are due to interference from the Brewster mounted diamond window. OMNIC software from Nicolet was used to remove these sidebands. The sequence of the data manipulation was as follows. The Beamsplitter spectrum (fig. 4.12) was subtracted from the background and sample interferograms. Two points either side of the sideband were picked on the same level to coincide when the oscillations had died off and the region was replaced by a straight line. The exact same region was replaced by a straight line in the sample spectrum. Both spectra were normalised for a 1 A ring beam current and ratioed together. A triangular apodization function was used and a zero filling factor of 1 level. The noise level after manipulation was 0.005 (experiment I) and 0.025 (experiment II).

Figure 4.11.a Sidebands Displayed for the Interferograms in Experiment I

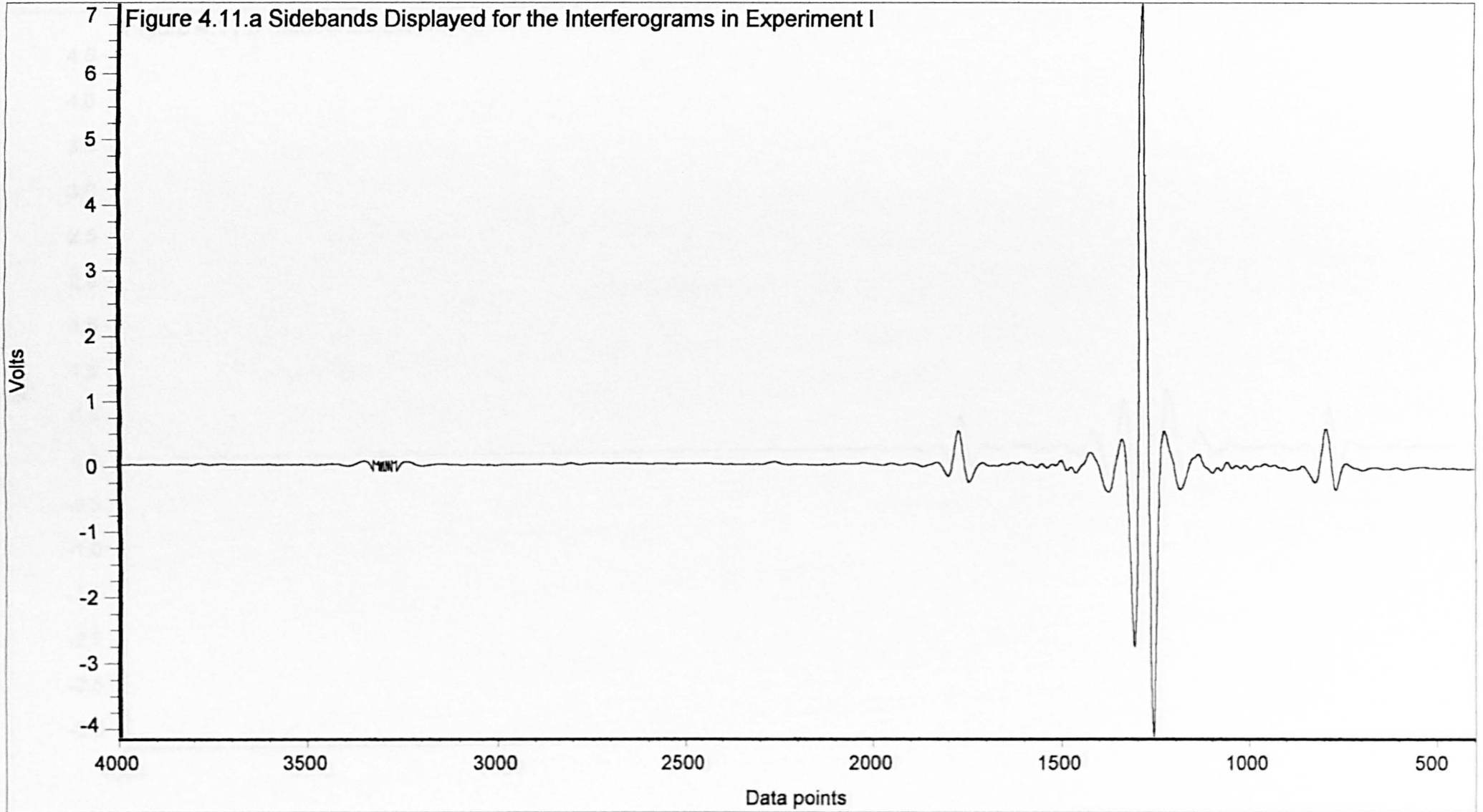


Figure 4.11.b Sidebands Displayed for the Interferograms in Experiment II

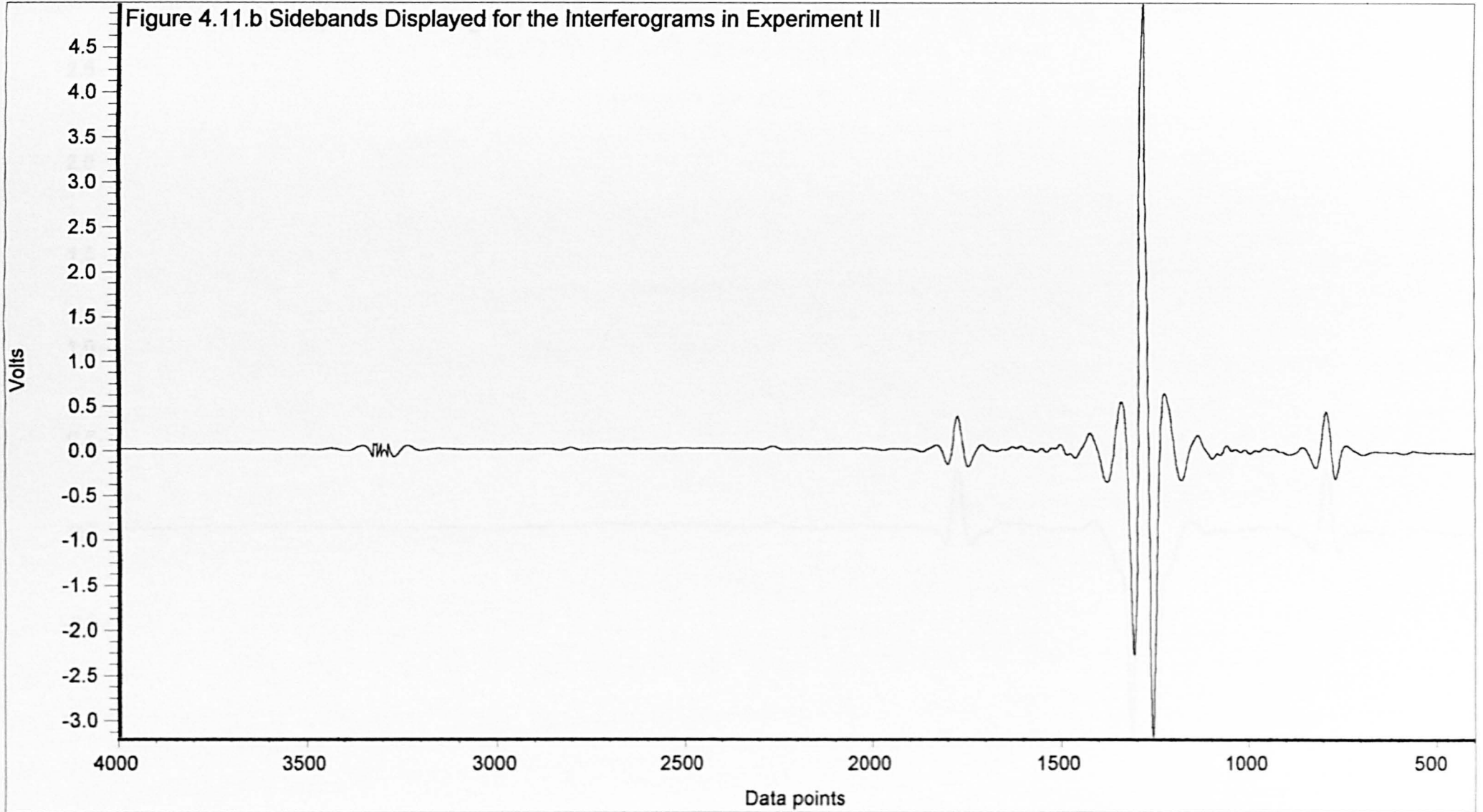


Figure 4.12 Beamsplitter Interferogram

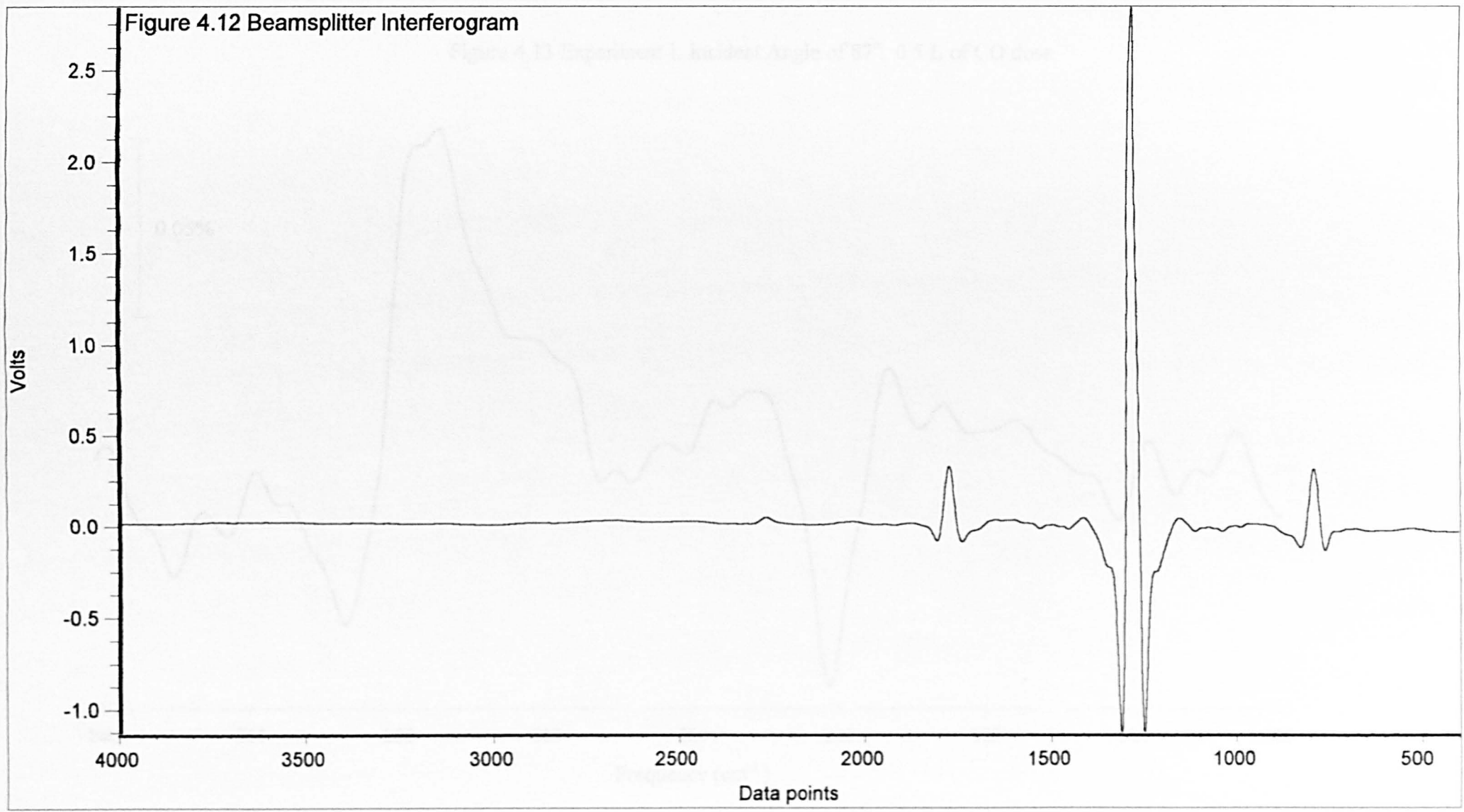


Figure 4.13 Experiment I. Incident Angle of 87°. 0.5 L of CO dose

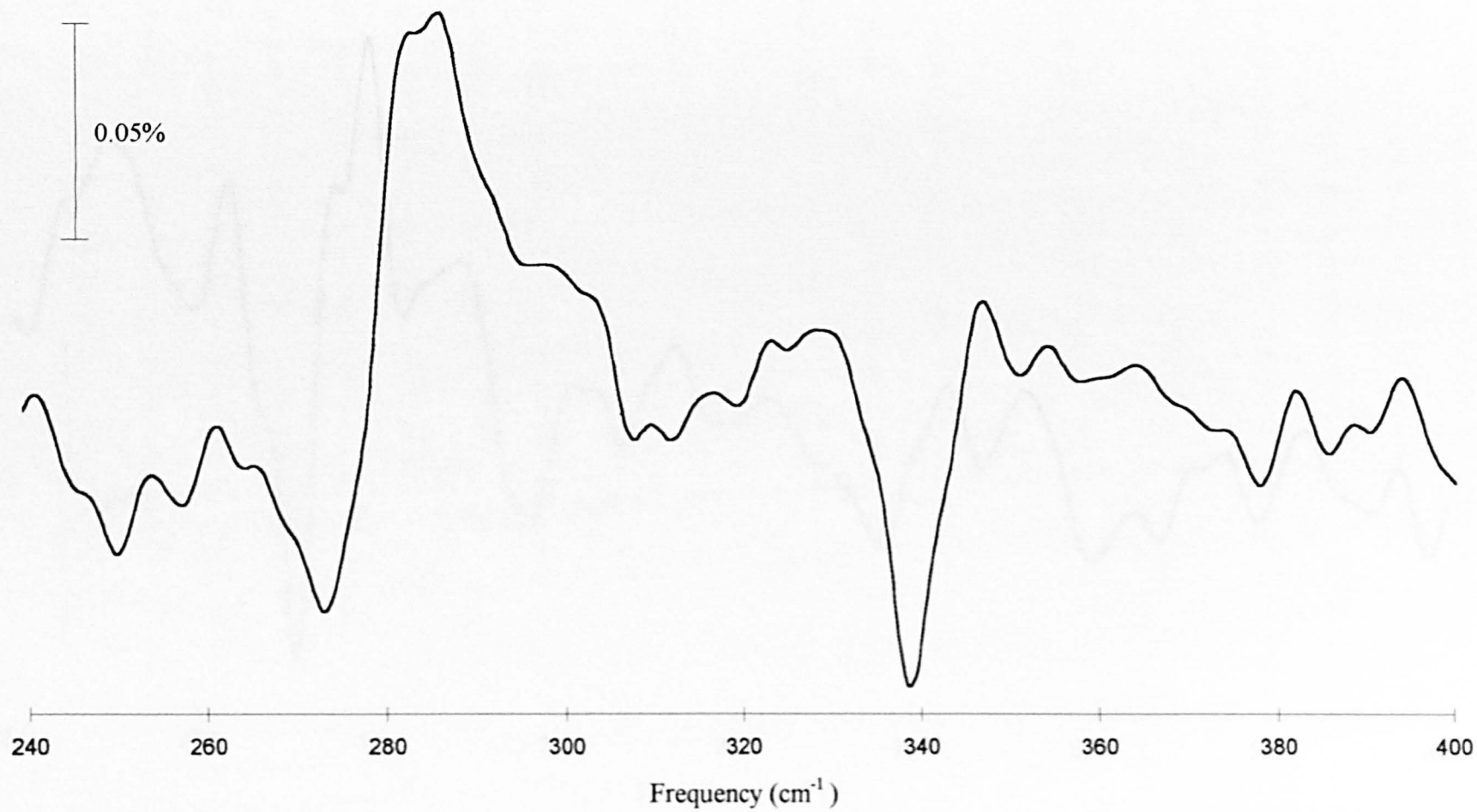
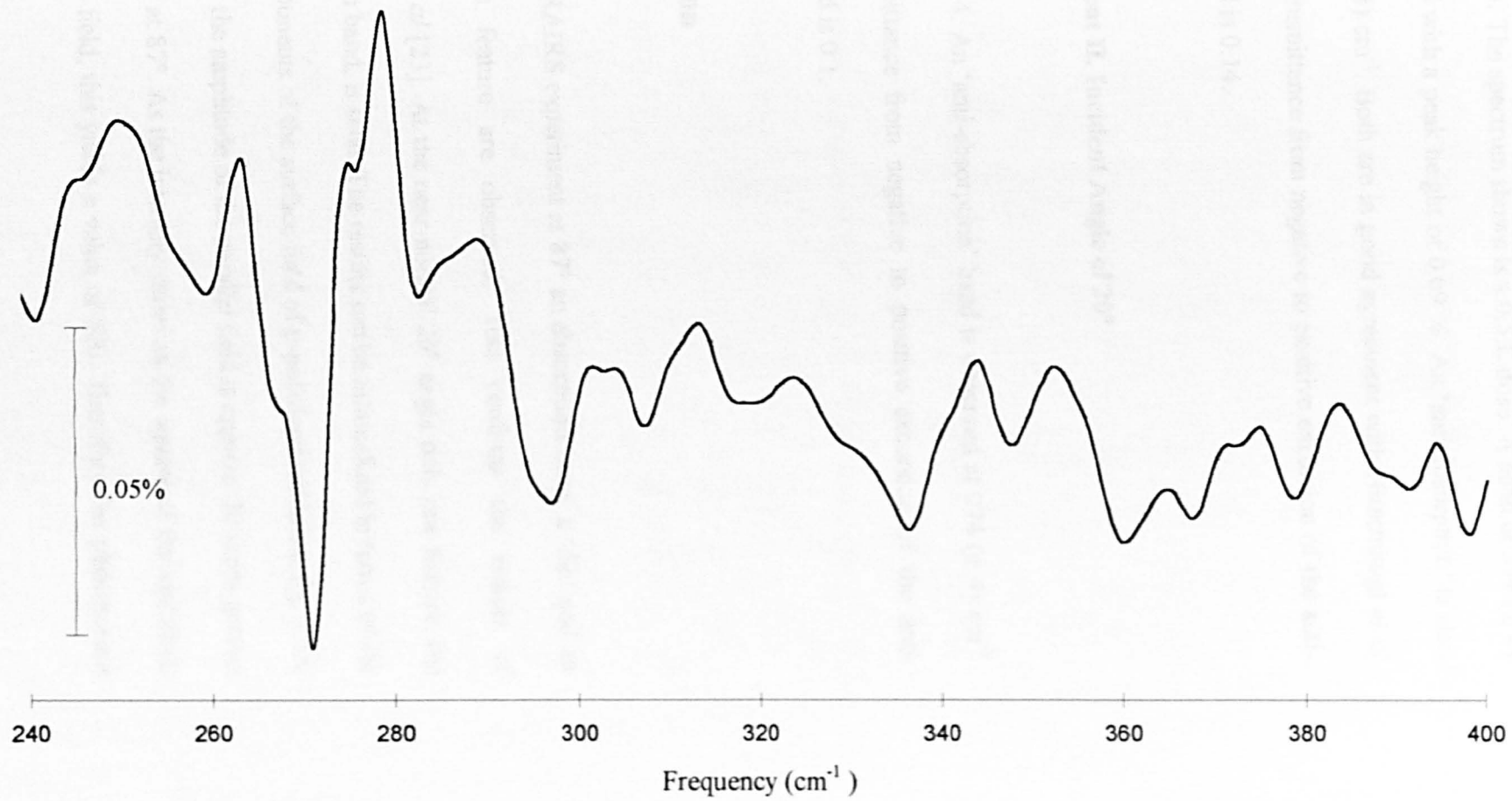


Figure 4.14 Experiment II. Incident Angle of 20° . 0.5 L of CO dose



4.6.2 Experiment I. Incident Angle of 87°

Fig. 4.13. The spectrum shown is a 0.5 L dose. A band at 339 (± 4) cm^{-1} is observed with a peak height of 0.09 %. An 'anti-absorption' is also seen at 278 (± 4) cm^{-1} . Both are in good agreement with Hirschmugl *et al* [23]. The % transmittance from negative to positive excursion of the anti-absorption band is 0.14.

4.6.3 Experiment II. Incident Angle of 20°

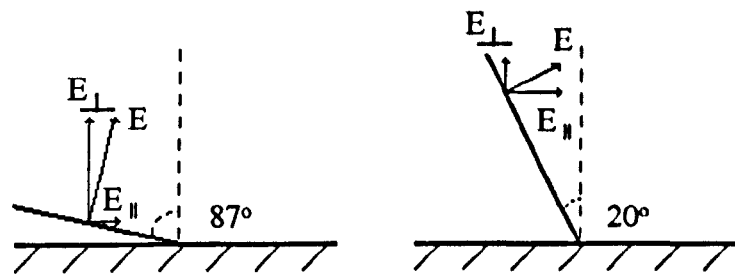
Fig. 4.14. An 'anti-absorption' band is observed at 274 (± 4) cm^{-1} . The % transmittance from negative to positive excursion of the anti-absorption band is 0.1.

4.7 Discussion

In the RAIRS experiment at 87° an absorption band, a 'dip' and an anti-absorption feature are observed. This confirms the results of Hirschmugl *et al* [23]. At the near-normal 20° angle only one feature, the anti-absorption band, is seen. The results can be rationalized in terms of the resultant components of the surface field of p-polarized radiation, fig. 4.15.

At 20° the amplitude of the parallel field is approx. 20 times greater than the value at 87°. As the intensity varies as the square of the amplitude of the electric field, this yields a value of 400. Therefore the phenomenon

Figure 4.15 The Resultant Components of the Surface Field of P-polarised Radiation



I Incident Angle of 87°

$$E_{\parallel} = E \cos 87^\circ$$

$$E_{\perp} = E \sin 87^\circ$$

$$E_{\parallel} / E_{\perp} = \cot 87^\circ$$

II Incident Angle of 20°

$$E_{\parallel} = E \cos 20^\circ$$

$$E_{\perp} = E \sin 20^\circ$$

$$E_{\parallel} / E_{\perp} = \cot 20^\circ$$

induced by the parallel electric field resulting in an anti-absorption band has an enhanced probability of occurring. The amplitude of the perpendicular field at 20° is approx. 3 times smaller than the value at 87° , thus the intensity is approx. 9 times smaller. Therefore the excitation of any mode of the surface adlayer that has a component of the dynamic dipole moment perpendicular to the surface is reduced.

In simple terms as the calculation above suggests, a large effect resulting in an intense anti-absorption band should be observed. The spectrum reported though, shows loss of the perpendicular band but no enhancement of the anti-absorption band.

The parallel field indirectly induces a collective drift motion of the electrons just inside the metal surface. The presence of the CO adsorbate on the surface results in a reduction in the reflectivity as the resistance the electrons experience increases. The level of reflectivity is restored at the resonant energy of the frustrated rotation mode of the CO parallel to the surface as the coupling of this mode with the parallel motion of the electrons removes the extra resistivity they experience due to the CO adsorbate. It is not clear how this effect might scale with the amplitude of the parallel electric vector.

The intensity is also proportional to the pathlength of the infrared radiation through the adsorbing layer as $1/\cos\theta$ [38]. At 20° the interaction with the adsorbate is reduced approximately by a factor of 18. Therefore the intensity multiplication factor expressed above would be reduced by this factor. The results above show that the anti-absorption band is

approximately the same size for both angles. If the phenomenon induced by the parallel electric field scaled with the square of the field, an anti-absorption band 20 times greater is expected. However, if it scales with the field, an anti-absorption band of similar size is expected. Therefore it appears that this phenomenon is dependent on the amplitude of the parallel electric field.

If the pathlength at 20° is reduced by a factor of 18 and this is combined with the reduction in perpendicular field intensity at 20° (9 times less intense) then the sensitivity of this field is reduced by an approximate factor of 160. Therefore, as the absence of the absorption band at 20° confirms, the interaction of the perpendicular field with the metal-carbon stretch of the on-top CO (perpendicular dipole moment) is negligible with this reduced sensitivity.

Overall this experiment confirms the involvement of the parallel electric field.

4.8 Alternative Mechanisms to Describe the Observation of Parallel Modes

Anti-absorption resonance's have been predicted to occur for all dipole forbidden vibrations if there is a non-negligible coupling between the adsorbate vibrational mode and the metal conduction electrons [39].

Anti-absorption lineshapes have been observed by Chabal *et al* for H and D on W(100) [40] and Mo (100) [41]. In these cases they have not been attributed to parallel adsorbate vibrations but from the coupling of sharp vibrational modes with a broad continuum of electron-hole pairs excited to just above the Fermi level. This resonant interaction results in a modulation of the continuum and an anti-absorption lineshape of the mode. The H/W (100) and H/Mo (100) systems are complicated with adsorbate induced surface reconstructions and complex band structure.

A Fermi-resonance mechanism where parallel vibrational modes may become dipole active through coupling to the Pt-CO stretch have recently been postulated for a doublet of peaks at 370 cm^{-1} and 378 cm^{-1} for CO adsorbed in the bridge site of Pt (111) by Engström *et al* [8]. The difference combination mode of the frustrated rotation (133 cm^{-1}) and the frustrated translation (510 cm^{-1}), both B_2 modes, is located at $\sim 377\text{ cm}^{-1}$ and therefore, because the difference between this resonance and the stretch (370 cm^{-1}) is small, they can couple. This has not been observed for the on-top bonded molecules.

In the same study by Engström *et al* [8] they did not observe any anti-absorption bands, in contrast to the CO, NO and H on different copper surfaces. Similarly no observation of an anti-absorption band was made for CO on Ni (100) at room temperature by Lin *et al* [42].

4.9 Summary

From the evidence there are two important criteria for the observation of an anti-absorption resonance. The vibrational mode must generate a motion parallel to the surface and the atom generating this motion must be 'dipping into' the sea of valence electrons. Thus parallel vibrational modes which have the same frequency as the collective parallel drift motion of the electrons just inside the metal surface can indirectly couple to this motion. The additional resistance incurred by the inelastic scattering of the electrons off the nuclei of the adsorbed molecules disappears resulting in an anti-absorption band. If the position of the atom is too high then there is no effect as the 'obstacles' (the nuclei) to the paths of the electrons are removed. This explains why anti-absorption bands are not more widely seen in RAIRS studies.

Low frequency parallel vibrational modes of adsorbates on the surface include frustrated translations and rotations. Light atoms would generate a large amplitude of motion parallel to the surface, indeed the highest frequency anti-absorption band reported is that for hydrogen by Lamont *et al* [26]. They have measured dipole forbidden parallel translational modes which give rise to anti-absorption peaks for H and D atoms adsorbed on Cu (111). The anti-absorption peak for H occurred at 770 cm^{-1} . Remarkably, the parallel modes are ~ 8 times more intense than the dipole allowed perpendicular modes.

It is clear that to maximize the incoming parallel field of the incoming wave, taking into the account the adsorbing species when determining the intensity, an angle dependent study would have to be undertaken. A range of metals and surfaces should be included and data on properties of these surfaces *e.g.* resistivity and reflectivity should be obtained.

The anti-absorption band resulting from a parallel field is not observed in an EELS experiment as the force lines associated with the incoming electrical field are distorted such that they are terminated perpendicular to the metal surface as a result of the metal conduction electrons. Therefore the incoming field is perpendicular. This is in contrast to the RAIRS experiment where a component parallel to the surface exists when examining the incoming wave.

4.10 Conclusions

The experimental work in this chapter has involved changing the angle of incidence of the typical RAIRS experiment of 87° to 20° . This enabled the ratio of the incoming vectors of the parallel electric field to the perpendicular electric field to increase. This resulted in no absorption band at 339 cm^{-1} and an anti-absorption band at 274 cm^{-1} of similar magnitude to that reported at 87° . This work has confirmed the involvement of the parallel field in an alternative mechanism resulting in the appearance of

anti-absorption bands. It is also postulated that this phenomenon scales with the amplitude of the parallel electric field.

4.11 References

- [1] S. Chiang, R.G. Tobin, P.L. Richards and P.A. Thiel, *Phys. Rev. Letts.* 52 (1984) 648
- [2] R.G. Tobin and P.L. Richards, *Surf. Sci.* 179 (1987) 387
- [3] W.A. Brown, R.K. Sharma, P. Gardner, D.A. King and D.H. Martin, *Surf. Sci.* 331-333 (1995) 1323
- [4] D. Hoge, M. Tushaus, E. Schweizer and A.M. Bradshaw, *Chem. Phys. Letts.* 151 (1988) 230
- [5] I.J. Malik and M. Trenary, *Surf. Sci.* 214 (1989) L239
- [6] B.N.J. Persson and R. Ryberg, *Phys. Rev. B.* 40 (1989) 10273
- [7] R. Ryberg, *J. Electron Spectrosc. Relat. Phenom.* 54/55, (1990) 65
- [8] U. Engström and R. Ryberg, *Phys. Rev. Letts.* 78 (1997) 1944
- [9] X.D. Wang and R.G. Greenler, *Surf. Sci.* 226 (1990) L51
- [10] M.R. Peng and J.E. Reutt-Robey, *Surf. Sci.* 336 (1995) L755
- [11] V.M. Bermudez, R.L. Rubimowitz and J.E. Butler, *J. Vac. Sci. Tech.* A6 (1988) 717
- [12] F.M. Hoffman, N.J. Levinos, B.N. Perry and P. Rabinowitz, *Phys. Rev. B* 33 (1986) 4309
- [13] G. Margaritondo, *Introduction to Synchrotron Radiation*, (Oxford University Press, 1988)

- [14] P. Hollins, University of Reading. With kind permission.
- [15] D.A Slater, P. Hollins, M.A. Chesters, J.Pritchard, D.H Martin, M. Surman, D.A. Shaw and I. Munro, Rev. Sci. Instrum. 63 (1992) 1547
- [16] F.M. Hoffmann, Surf. Sci. Reports 3, 1982, 107
- [17] B.E. Hayden in Methods of Surface Characterisation (Eds. J.T. Yates and T.E. Madey) Vol 1, Plenum, New york, 1987, 267
- [18] N.V. Richardson and N. Sheppard in Methods of Surface Characterisation (Eds. J.T. Yates and T.E. Madey) Vol 1, Plenum, New York, 1987, 1
- [19] P. Hollins, Surf. Sci. Reports 16, (1992) 51-94
- [20] G. Blyholder, J. Chem. Phys. 68 (1964) 2772
- [21] N. Sheppard and T.T. Nguyen, Adv. Infrared Raman Spectroscopy 5 (1978) 67
- [22] C.J. Hirschmugl, G.P. Williams, F.M. Hoffmann and Y.J. Chabal, Phys. Rev. Letts. 65 (1990) 480
- [23] C.J. Hirschmugl, G.P. Williams, F.M. Hoffmann and Y.J. Chabal, J. Elect. Spect. Rel. Phenom. 54/55 (1990) 109
- [24] C.J. Hirschmugl, P. Dumas, Y.J. Chabal, F.M. Hoffmann, M. Suhren and G.P. Williams, J. Elect. Spect. Rel. Phenom. 64/65 (1993) 67
- [25] C. J. Hirschmugl, G.P. Williams, B.N.J. Persson and A.I. Volokitin, Surf. Sci. 317 (1994) L1141-L1146
- [26] C.L.A. Lamont, B.N.J. Persson and G.P. Williams, Chem. Phys. Letts. 243 (1995) 429
- [27] A.I. Volokitin and B.N.J. Persson, Phys. Rev. B 52 (1995) 2899

- [28] S. Andersson, Surf. Sci. 89 (1989) 477-485
- [29] P. Uvdal, P.A. Karlsson, C. Nyberg, S. Andersson and N.V. Richardson, Surf. Sci. 202 (1988) 167-182
- [30] R.Raval, S.F. Parker, M.E. Pemble, P. Hollins, J. Pritchard and M.A. Chesters, Surf. Sci. 203 (1988) 353-377
- [31] F. M. Hoffmann and G.P. Williams, Springer Ser. Surf. Sci. 35 (1995) 263
- [32] C. J. Hirschmugl, Thesis
- [33] H.A. Pearce and N. Sheppard, Surf. Sci. 59 (1976) 205
- [34] R.G. Greenler, J. Chem. Phys. 44 (1966) 310
- [35] P. Hollins and J. Pritchard, Prog. Surf. Sci. 19 (1985) 275
- [36] J.D.E. Mc Intyre, D.E. Aspnes, Surf. Sci. 24 (1971) 417
- [37] Prof. M.A. Chesters, University of Nottingham
- [38] J. Pritchard in 'Chemical Physics of Solids and their Surfaces', (Eds. M.W. Roberst and J.M. Thomas), Specialist Periodical Reports, The Chemical Society, London, 1978
- [39] B.N.J. Persson and A.I. Volokitin, Surf. Sci., 310 (1994) 314-336
- [40] J.E. Reutt, Y.J. Chabal and S.B. Christman, 44 (1987) 325-332
- [41] J.E. Reutt, Y.J. Chabal and S.B. Christman, Phys. Rev. B, 38 (1988) 3112
- [42] K.C. Lin, R.G. Tobin, P. Dumas, C.J. Hirschmugl, G.P. Williams, Phys. Rev. B, 48 (1993) 2791

Chapter Five

The Adsorption of Hydrogen on Pt (111)

5.1 Introduction

5.1.1 Previous Studies of Hydrogen Adsorption on Pt (111) Based on EELS

5.2 The Adsorption of Hydrogen on (111) Surfaces : A Comparison

5.3 Experimental

5.3.1 Off-specular Study

5.3.2 Coverage Dependence Study

5.4 Discussion

5.5 Summary

5.6 Conclusions

5.7 References

5.1 Introduction

The bonding of hydrogen to the surface of transition metals has received a significant amount of attention over the last few decades [1]. Heterogeneous catalysis has been an area where reactions involving hydrogen as either a reactant or product molecule have motivated the study of the hydrogen-surface interaction. The Haber-Bosch synthesis of ammonia, hydrogenolysis of long chain alkanes or solidification of unsaturated fatty acids are just a few of the industrially important reactions utilizing the technique of heterogeneous catalysis.

The enigma of hydrogen lies in its ability to baffle the experimental scientist. Possessing only a single valence electron, hydrogen should be the simplest chemically reacting adsorbate. It has proved to be one of considerable complexity.

The small size of the hydrogen atom leads to the possibility of several types of adsorbed hydrogen occupying different surface sites. The vibrational spectroscopic technique of Electron Energy Loss Spectroscopy is particularly suitable for studying hydrogen adsorption for a number of reasons. The level of sensitivity it presents together with the capability of measuring impact excited modes over an extensive spectral range has enabled this method to be used as the basis for identification of the type of hydrogen chemisorption and adsorption site.

Platinum is widely known as a key component in the '3-way automotive catalyst' for car exhaust fumes. It is hoped that an improved

understanding of the reactions taking place on the metal surface could benefit the kinetics of the catalysis and economic use of this expensive metal. In the petrochemical industry, platinum, both as a metal and a supported catalyst, Pt/SiO₂, is used to adsorb hydrogen and to 'crack' hydrocarbons. Therefore there is great interest in the adsorption process, adsorption site and subsequent reactions using surface sensitive techniques.

The work undertaken in this chapter attempts to rationalise previous work and in addition provide further data on the adsorption of hydrogen on platinum (111).

5.1.1 Previous Studies of Hydrogen Adsorption on Pt (111) Based on EELS

The hydrogen on Pt (111) adsorption system has been studied both experimentally and theoretically. It is known that hydrogen adsorption is dissociative [1], but no definite agreement has been reached as to the assignment of the vibrational bands observed.

One of the models used to predict and interpret EEL spectra of hydrogen on metal surfaces is the nearest neighbour central force constant model (NNCFC) [2,3]. This model allows calculations of the adsorbate geometry from the observed ν_{sym} and ν_{asym} frequencies of multiply coordinate species. The model has been experimentally confirmed for the M-H bond stretching frequencies of μ_2 -bridged metal hydrides [4] but

controversy exists in the application of this model. The details will be discussed further in section 5.4.

Baro *et al* [3] used the NNCFC model in their interpretation of the reported EEL spectra. They recorded the hydrogen on Pt (111) spectra at 90 K and at a hydrogen coverage of $\Theta_{\text{max}} = 0.7$ [5], both on and off-specular. Hydrogen did not form an ordered LEED pattern. Two vibrational bands were observed at 550 cm^{-1} (400 cm^{-1} with deuterium) and 1230 cm^{-1} (900 cm^{-1} with deuterium) and were assigned to the modes perpendicular (ν_{\perp}) and parallel (ν_{\parallel}) to the surface respectively based on a perceived dipole contribution of the band at 550 cm^{-1} . They concluded that the hydrogen atom occupied the threefold hollow site.

Feibelman *et al* [6] have argued that the spectrum recorded by Baro [3] was incorrectly interpreted. They criticize the experimental details and the model used to support the assignments. At the adsorption temperature of 90 K a He diffraction study has shown that a disordered hydrogen layer was produced, with the probability of hydrogen occupying more than one site [7].

The second problem with the experiments is impurity contamination. The CO peaks grow in proportion to the H exposure. The total CO coverage was estimated to be less than 0.01 monolayer but the dipole strength of the CO is so large that this contribution obscures the hydrogen contribution to the specular EEL spectrum. The feature Baro [3] identify as the dipole active H-Pt mode falls in the same region as the CO-Pt stretching mode. Even though Baro [3] subtracted an estimated

contribution of this mode, Feibelman [6] suggest that because the calculation of a dynamic effective charge for the symmetric stretch is small that the dipole scattering contribution might be comparable in amplitude to the impact scattering and therefore this mode might not stand out in a specular spectrum. They can find no reason for the breadth of the feature at 550 cm^{-1} , but believe there is no contribution from a fundamental mode of 3-fold H in this energy range.

They offer an alternative solution. They identify a weak feature around 800 cm^{-1} which 'with some imagination' can be seen to move to higher energy with increasing coverage, merging into the broad loss feature from 880 to 1360 cm^{-1} at saturation. They identify this as the anti-symmetric mode, as the same mode for H/Ru displays the same coverage dependence, while the symmetric mode is nearly coverage independent.

They also dispute the validity of the NNCFC model and the geometric calculations for use in assigning the hydrogen adsorption site. Their main objection is that it leads to unreasonable bond lengths and incorrect mode assignments. They have calculated a symmetric stretch of 1339 cm^{-1} and an anti-symmetric stretch of 919 cm^{-1} by linearized augmented plane wave (LAPW) calculations to obtain reasonable bond lengths. To support their predictions they cite a study of hydrogen on Pt by inelastic neutron diffraction [8]. This was performed on Pt black powder and offers a variety of adsorption sites. Six sharp loss features are identified. Two of them, at 936 cm^{-1} and 1298 cm^{-1} are close to their calculated frequencies.

Richter *et al* [9] have also studied H on Pt (111) with EEL spectroscopy at 80 K. The saturated coverage at this temperature based on He diffraction measurements is 1 monolayer (ML) [7]. They identify features at 540, 903 and 1234 cm^{-1} which were assigned to the modes ν_{asym} , ν_{sym} and an unresolved band of the overtone $\nu_{\text{asym } 0 \rightarrow 2}$ and a combination mode $\nu_{\text{asym}} + \nu_{\text{sym}}$. This was based on the angle and the primary electron energy dependence of the loss intensities which confirmed the dipole activity of ν_{sym} which is the only fundamental of A_1 symmetry. They also question the validity of the NNCFC model as their assignments agree with the LAPW model prediction of $\nu_{\text{asym}} < \nu_{\text{sym}}$. Their assignment of the modes was also based on INS spectra for H on Pt black by Rush *et al* [10] which display three losses at 525, 940 and 1330 cm^{-1} with the loss at 525 cm^{-1} showing approximately twice the intensity of that at 940 cm^{-1} . They agree that He diffraction experiments have established that at 160 K, hydrogen forms a well ordered (1x1) layer with all the hydrogen in identical 3-fold hollows [7]. They state that thermal energy atom scattering experiments have established that in the absence of water contamination an ordered layer exists at 80 K [11]. The assignment to one site being responsible for all three losses is suggested from the presence of a well-ordered (1x1) structure in their study. They resolve the adsorption site of hydrogen to be that of a 3-fold hollow.

5.2 The Adsorption of Hydrogen on (111) Surfaces : A Comparison

Conrad *et al* [12] obtained two dominant loss features at 822 cm^{-1} and 1136 cm^{-1} which were measured in a 10° off-specular direction for hydrogen adsorbed on Ru (0001). Slight frequency shifts were observed as the hydrogen coverage increased. The symmetrical threefold site was proposed, a non-symmetric threefold or twofold bridge site being excluded because of the number of bands observed. The terminally bonded hydrogen on top of Ru was excluded because this site should lead to a much higher frequency. A distinction between fcc and hcp sites on the basis of EELS measurements alone was not possible. The frequencies 822 and 1136 cm^{-1} were assigned to the modes parallel (ν_{\parallel}) and perpendicular (ν_{\perp}) to the surface respectively. Here compared to H/Pt (111) of Baro [3] the reverse order of assignment is made.

On Pd (111) two fundamental losses are reported by Conrad *et al* [13] under off-specular conditions at 773 and 998 cm^{-1} . They were assigned as the parallel, (ν_{\parallel}) and the perpendicular, (ν_{\perp}) modes respectively of hydrogen bonded in a threefold hollow site.

5.3 Experimental

Experiments were undertaken to obtain better quality spectra and the new generation EELS spectrometer was used in the pursuit of this

task. This enabled the signal to noise ratio to be maximized due to the new features of the advanced design. In addition the presence of contaminant features could be identified.

EEL spectra of hydrogen adsorbed on Pt (111) were recorded at 160 K. To minimize the amount of CO contamination the crystal was flashed at regular intervals during the cooling procedure and prior to dosing. Both on and off-specular measurements were undertaken. The resolution was between 5-8 meV. This resolution was chosen to maximize the intensity in the elastic peak and consequently the loss spectrum. The scan over 310 meV was measured in 0.49 meV steps with a gate time of 3 seconds/step; in this way one complete spectrum could be recorded in approximately 30 minutes. The hydrogen was dosed on by backfilling the chamber, the dose was chosen to saturate the surface and maximize the loss peaks.

Fig. 5.1 Shows the EEL spectrum in the specular direction of 200 L of hydrogen adsorbed on Pt (111). A loss feature at approximately 540 (± 10) cm^{-1} is observed together with a broad band feature which has maxima at 996 (± 10) cm^{-1} and 1185 (± 10) cm^{-1} . The relative intensities of the loss features in the specular direction are very weak as the result of the very small dipole moment associated with hydrogen vibrations and the fact that the H-Pt electronegativity difference is negligible. In the corresponding off-specular spectrum, fig. 5.2, the 534 (± 10) cm^{-1} loss is observed and the two maxima of the broad band feature are more distinct with peaks at 993 (± 10) cm^{-1} and 1188 (± 10) cm^{-1} . The ratio of the

Figure 5.1 200 L of H₂ adsorbed on Pt(111) recorded on-specular at 160 K

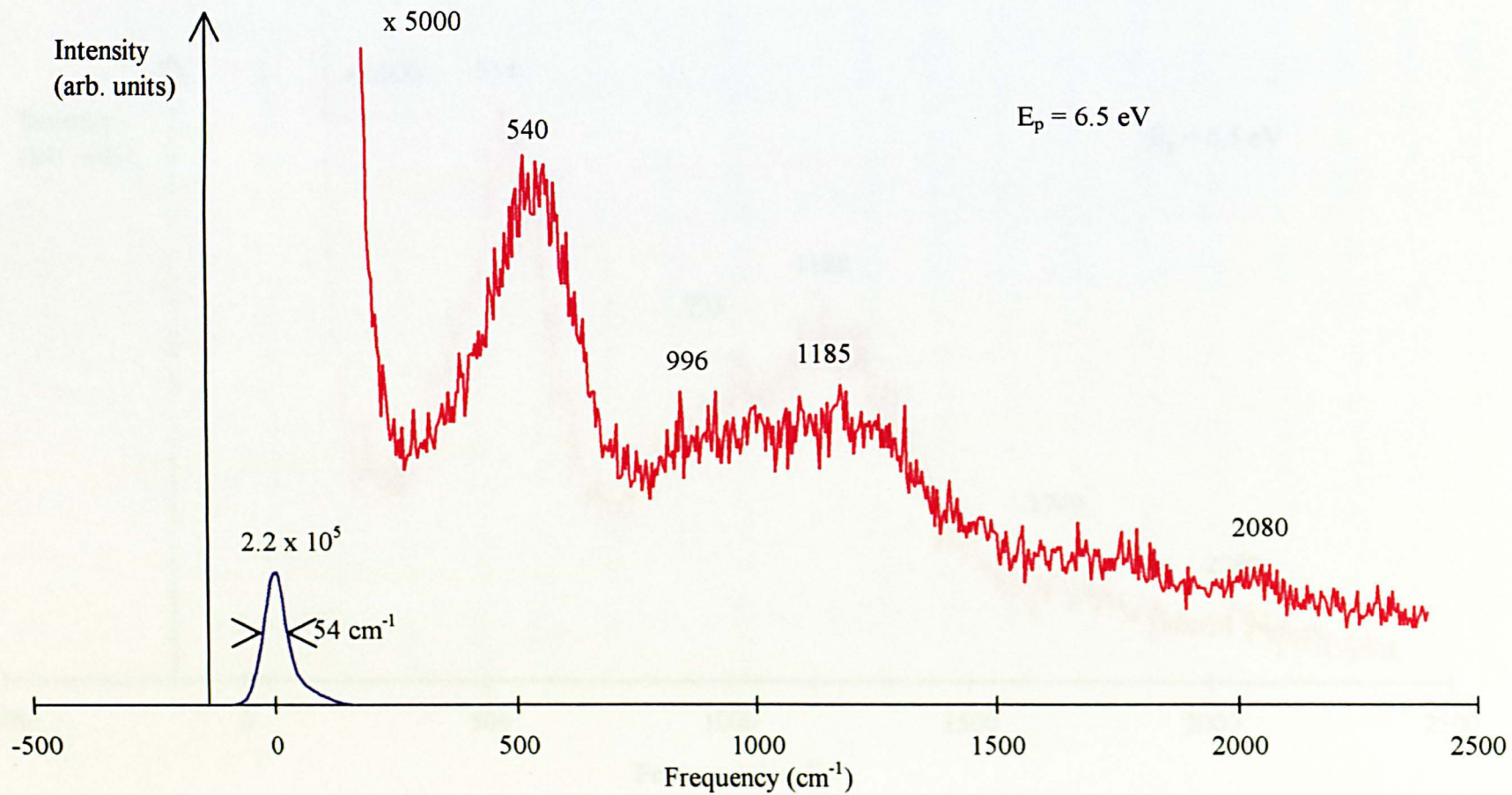
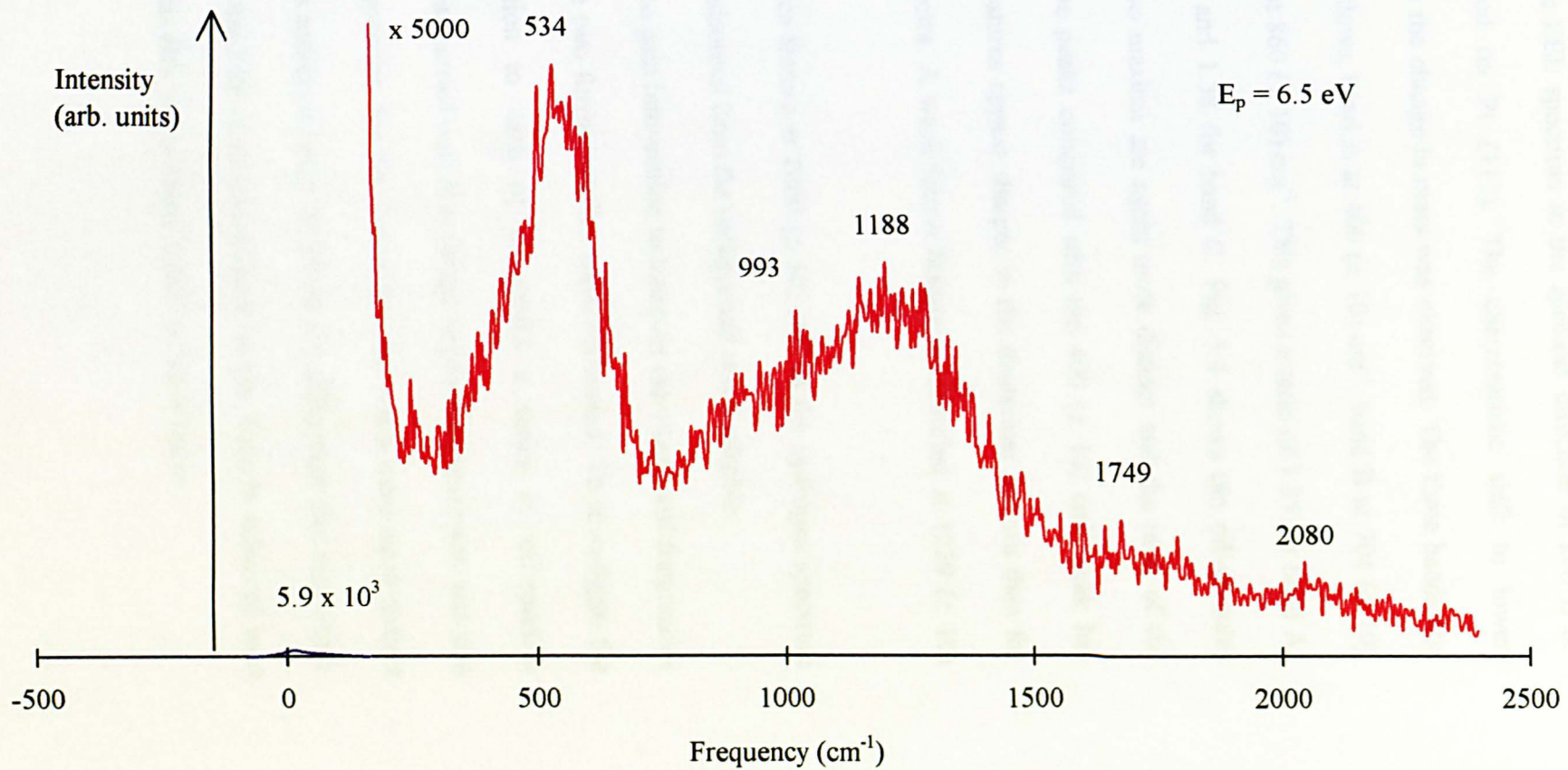


Figure 5.2 200 L of H₂ adsorbed on Pt(111) recorded 10° off-specular at 160 K



intensities of these peaks compared with the $534 (\pm 10) \text{ cm}^{-1}$ peak has increased. A weak fourth feature is identified at $1749 (\pm 10) \text{ cm}^{-1}$.

Fig. 5.3 shows the EEL spectrum in the specular direction of 200 L of deuterium adsorbed on Pt (111). The characteristic shift to lower frequencies due to the change in mass was observed. The three bands are now located as follows, band A at $400 (\pm 10) \text{ cm}^{-1}$, band B at $704 (\pm 10) \text{ cm}^{-1}$ and band C at $860 (\pm 10) \text{ cm}^{-1}$. This gives a ratio of 1.35 for band A, 1.41 for band B and 1.38 for band C. Fig. 5.4 shows the off-specular spectrum. The two maxima are again more distinct and the ratio of the intensities of these peaks compared with the $400 (\pm 10) \text{ cm}^{-1}$ peak has increased. The features appear sharper in the deuterium spectra than for the hydrogen spectra. A weak fourth feature is identified at $1239 (\pm 10) \text{ cm}^{-1}$.

The surface feature at $2080 (\pm 10) \text{ cm}^{-1}$ in the hydrogen spectrum show the CO coadsorbed from the background was negligible.

In order to gain information to interpret the vibrational frequencies and bonding site two further studies were performed. To investigate the dipole contribution to each of the peaks a series of off-specular measurements was carried out. A coverage dependent experiment was also undertaken off-specular, for the reason that the peaks were more distinct off-specular thus making it easier to follow any differences that may occur. Deuterium was used for these experiments as the features achieved were sharper, again this aids in the interpretation of the features.

Figure 5.3 200 L of D₂ adsorbed on Pt(111) recorded on-specular at 160 K

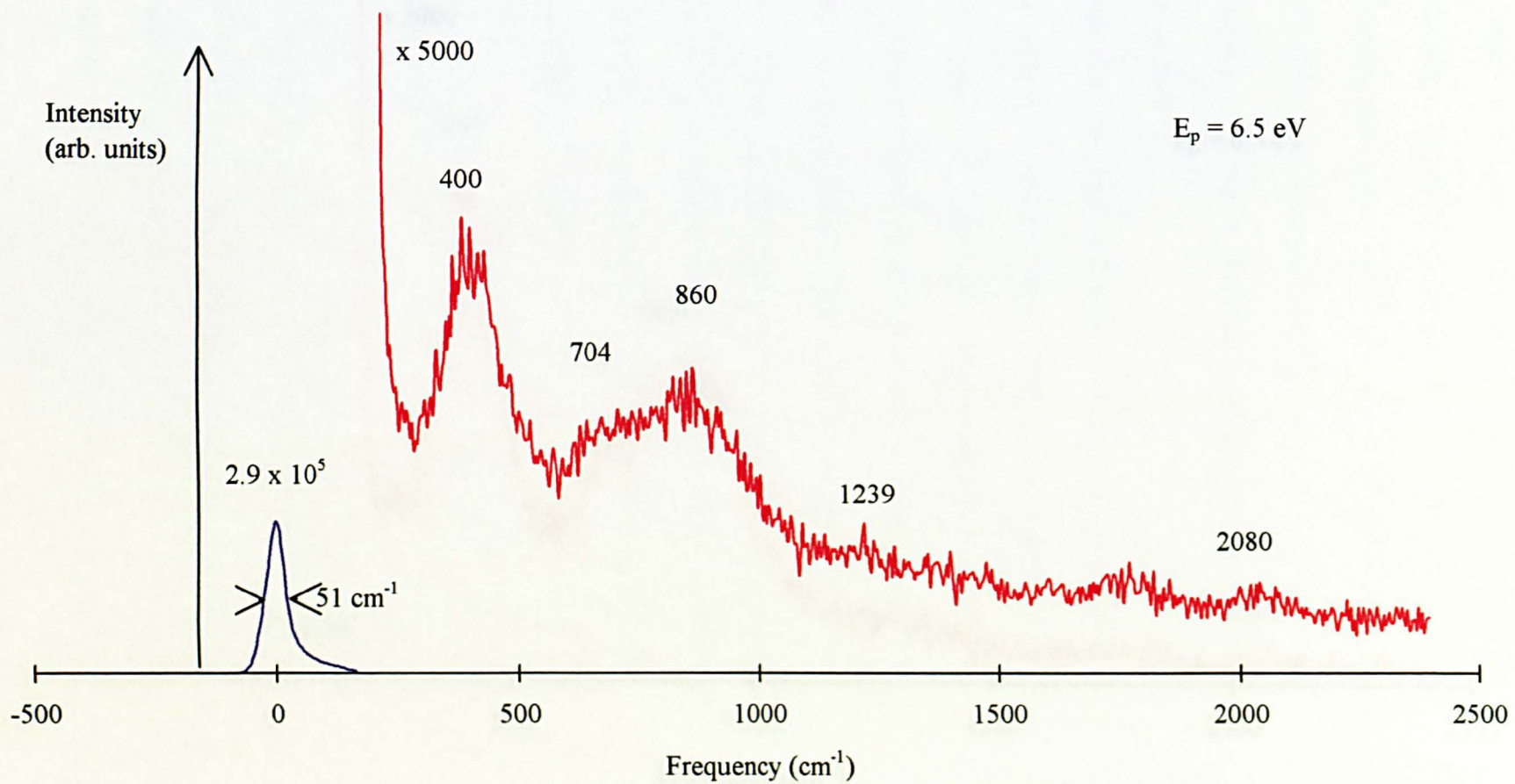
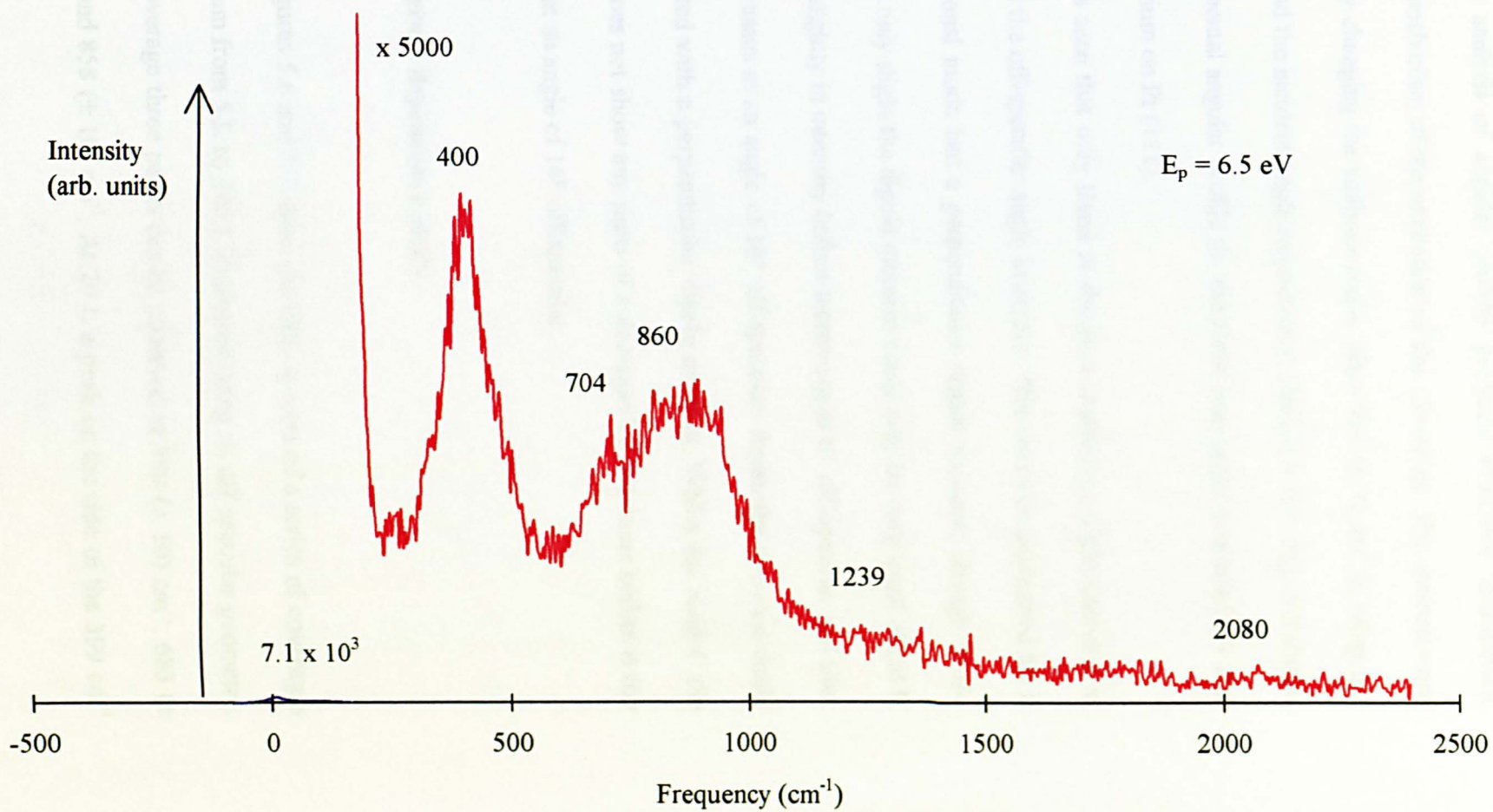


Figure 5.4 200 L of D₂ adsorbed on Pt(111) recorded 10° off-specular at 160 K



5.3.1 Off specular study

The analysis of angular profiles provides additional information about the mechanism of the excitation of the vibrations. The spectra were recorded by changing the analyser angle, $\Delta\theta_r = \theta_r - \theta_i$, θ_r and θ_i being the reflected and the incident angle respectively. Here $\theta_i = 60^\circ$. Fig. 5.5 shows the experimental angular profile for the three loss peaks measured for 200 L of deuterium on Pt (111).

It is seen that only Band A shows a continuous slight decrease in intensity as the off-specular angle increases. This could be accounted for if this vibrational mode had a perpendicular dipole moment, though as the decrease is only slight the dipole moment could only be very small. Band B decreases slightly in intensity before increasing at 6° off-specular and then finally decreases at an angle of 16° off-specular. Again the decrease could be associated with a perpendicular dipole moment. Whilst for band C the intensity does not show any signs of a decrease but increases before it too decreases at an angle of 16° off-specular.

5.3.2 Coverage dependence study

Figures 5.6 and 5.7 show the EEL spectra of a series of coverages of deuterium from 5 L to 240 L measured using an off-specular geometry. At low coverage three peaks can be observed at $399 (\pm 10) \text{ cm}^{-1}$, $683 (\pm 10) \text{ cm}^{-1}$ and $858 (\pm 10) \text{ cm}^{-1}$. At 20 L a peak on the side of the 399 cm^{-1}

Figure 5.5.a Angular Profile for the Elastic peak observed for 200 L of D_2 /Pt (111)

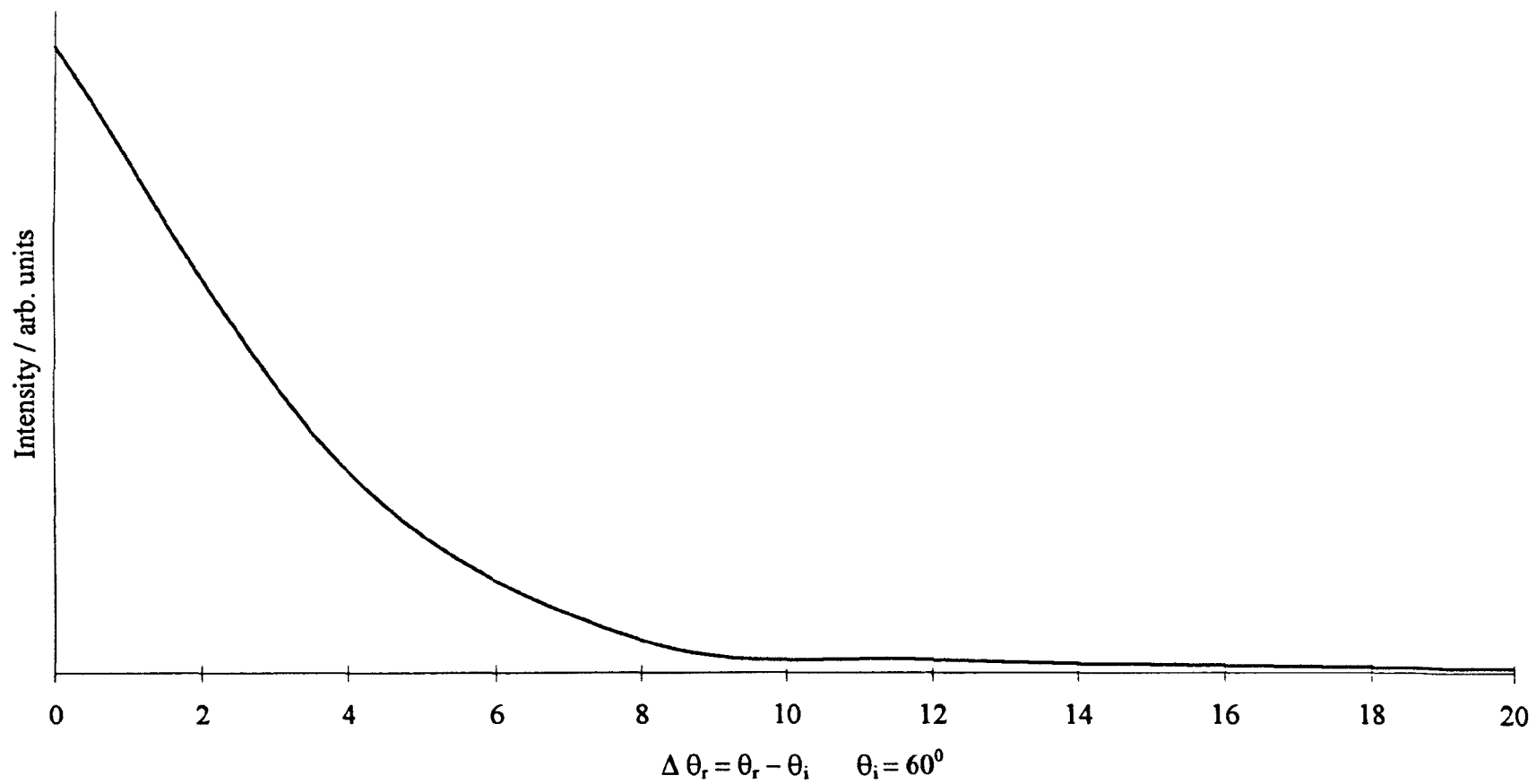


Figure 5.5.b Angular profile for the 3 loss peaks observed for 200 L of D_2 / Pt (111)

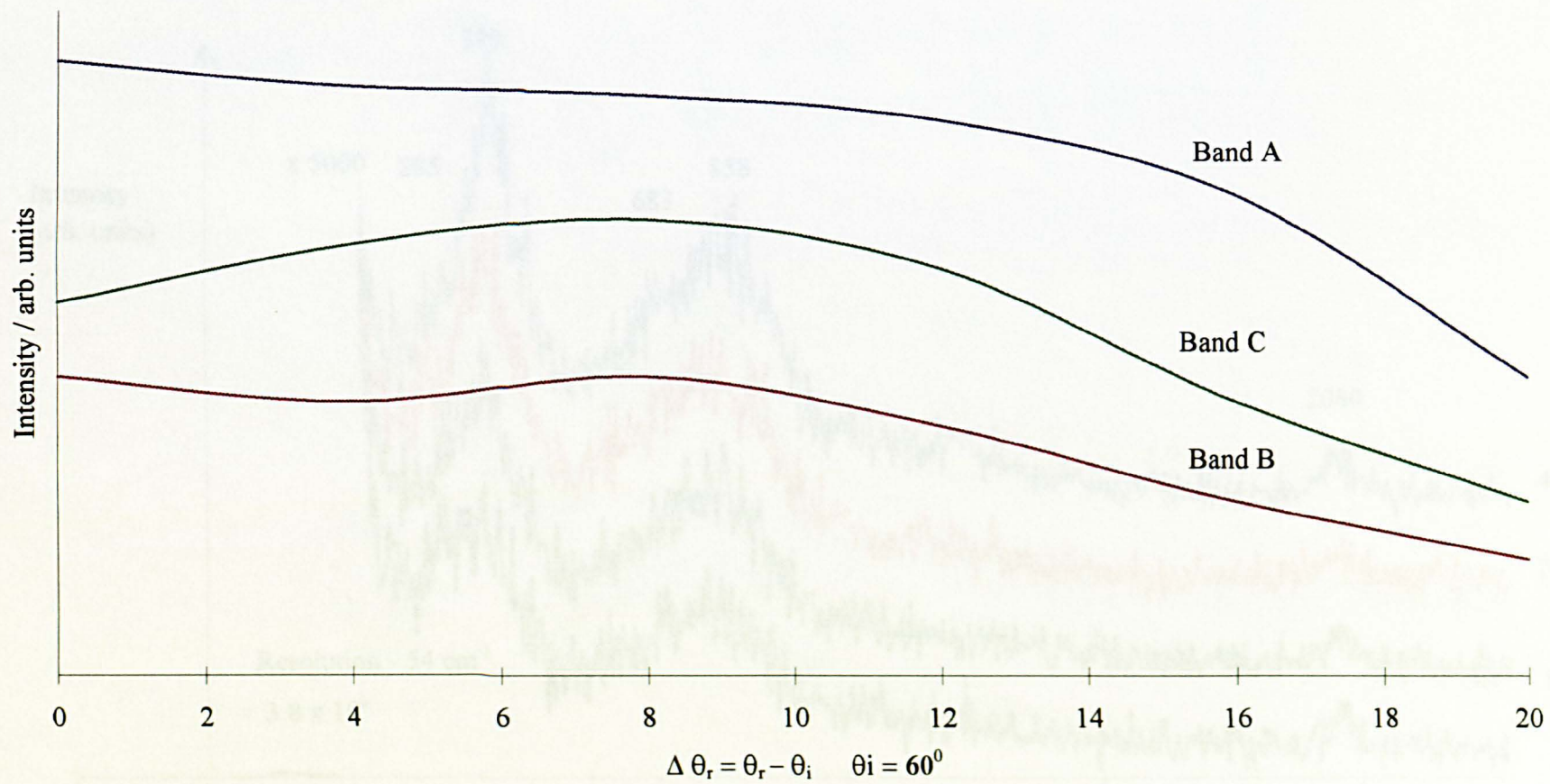


Figure 5.6 A Coverage Dependence Study of Deuterium Recorded at 12° Off-specular
5 L to 40 L

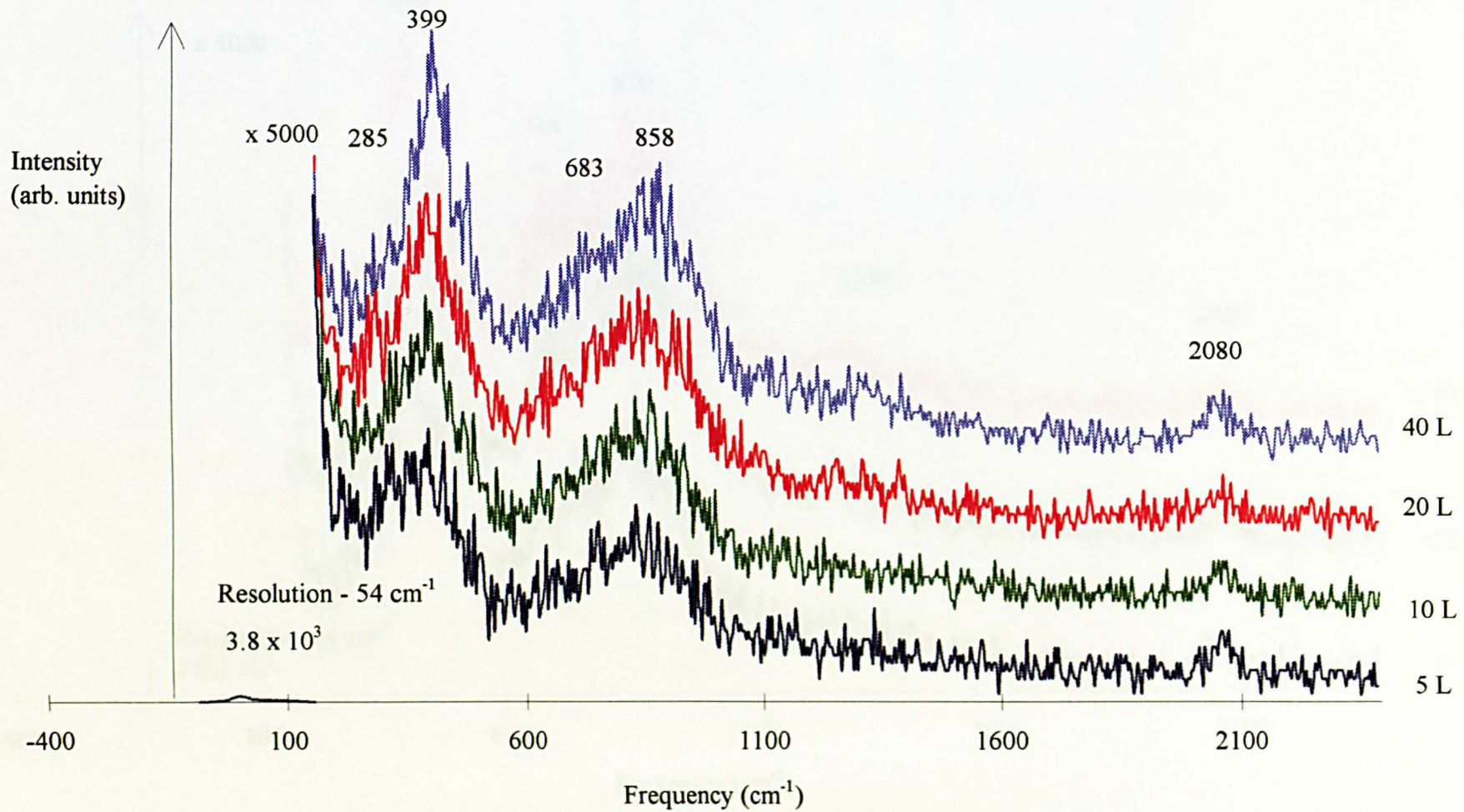
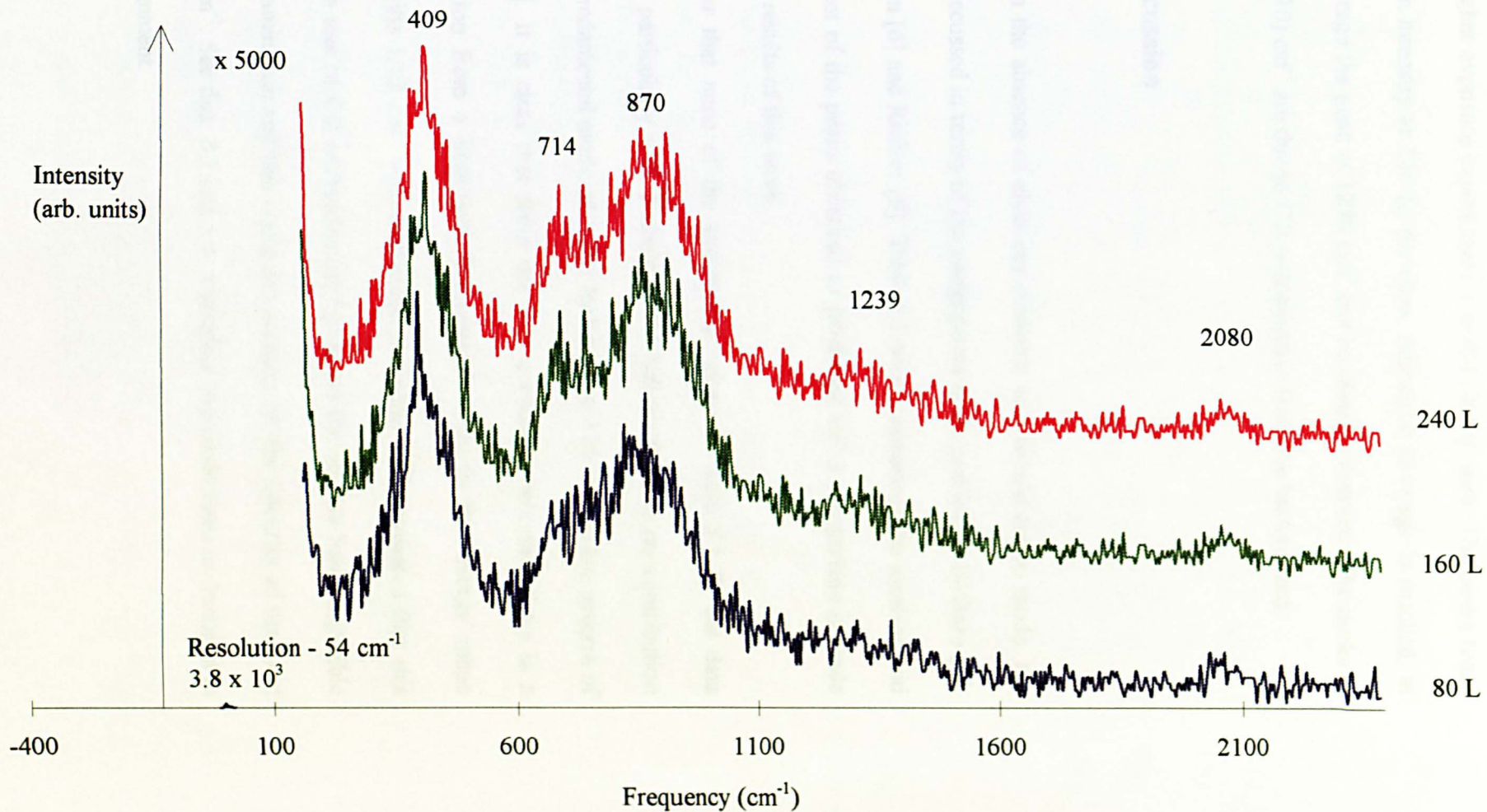


Figure 5.7 A Coverage Dependence Study of Deuterium Recorded at 12° Off-specular
80 - 240 L



peak can be seen at $285 (\pm 10) \text{ cm}^{-1}$. The same peak is still present at 40 L but in higher exposure experiments it is not clearly seen. The peaks reach maximum intensity at 160 L, therefore saturation coverage is reached, at this coverage the peak at 1239 cm^{-1} can be clearly observed. The peaks at $2080 (\pm 10) \text{ cm}^{-1}$ are due to CO coadsorption from the background.

5.4 Discussion

In the absence of clear-cut evidence of a dipole active mode, the data is discussed in terms of the assignments made previously by Baro [3], Feibelman [6] and Richter [9]. Table 5.1 below summarises the location and assignment of the peaks observed or predicted and a comparison is made from the results of this work.

It is clear that none of the assignments given in table 5.1 fit the data obtained particularly well. Feibelman [6] believe there is no contribution from a fundamental mode of 3-fold hydrogen at 550 cm^{-1} in the spectra of Baro [3]. It is clear that from the data presented here that there is a contribution from a hydrogen fundamental mode in this energy range which shifts $1/\sqrt{2} \text{ cm}^{-1}$ with deuterium. Feibelman [6] suggested that this band was due to CO contamination but again the spectra have negligible CO contamination and this could not account for the intensity of the band at 540 cm^{-1} . See figs. 5.1 and 5.2. Therefore this mode must be included in any assignment.

Table 5.1 The Interpretation of Observed and Calculated Bands

Bands observed (cm⁻¹) [3]	Assignment [3]	Bands calculated from LAPW [6]	Assignment [6]	Bands observed (cm⁻¹) [9]	Assignment [9]	Bands observed (cm⁻¹) [This work]
550	ν_s			540	ν_{as}	540
		919	ν_{as}	903	ν_s	996
1230	ν_{as}			1234	$\nu_{as} + \nu_s /$ $\nu_{as\ 0 \rightarrow 2}$	1185
		1339	ν_s			1749

The bands reported by Baro [3] and Richter [9] have similar frequencies, but the assignment is determined by a predicted dipole contribution to the symmetric stretch and reference to a theoretical model. Baro interprets his results using the NNCFC model and Richter a LAPW model. The NNCFC model is explained below together with the reasons why alternative models are preferred.

The NNCFC model is based on simple geometric considerations and is deduced from several assumptions, these are:

1. The hydrogen-platinum vibration is a harmonic oscillator with central, nearest neighbour forces.
2. The contribution of bending force constants are neglected. (The force constants for each site are assumed to be different).

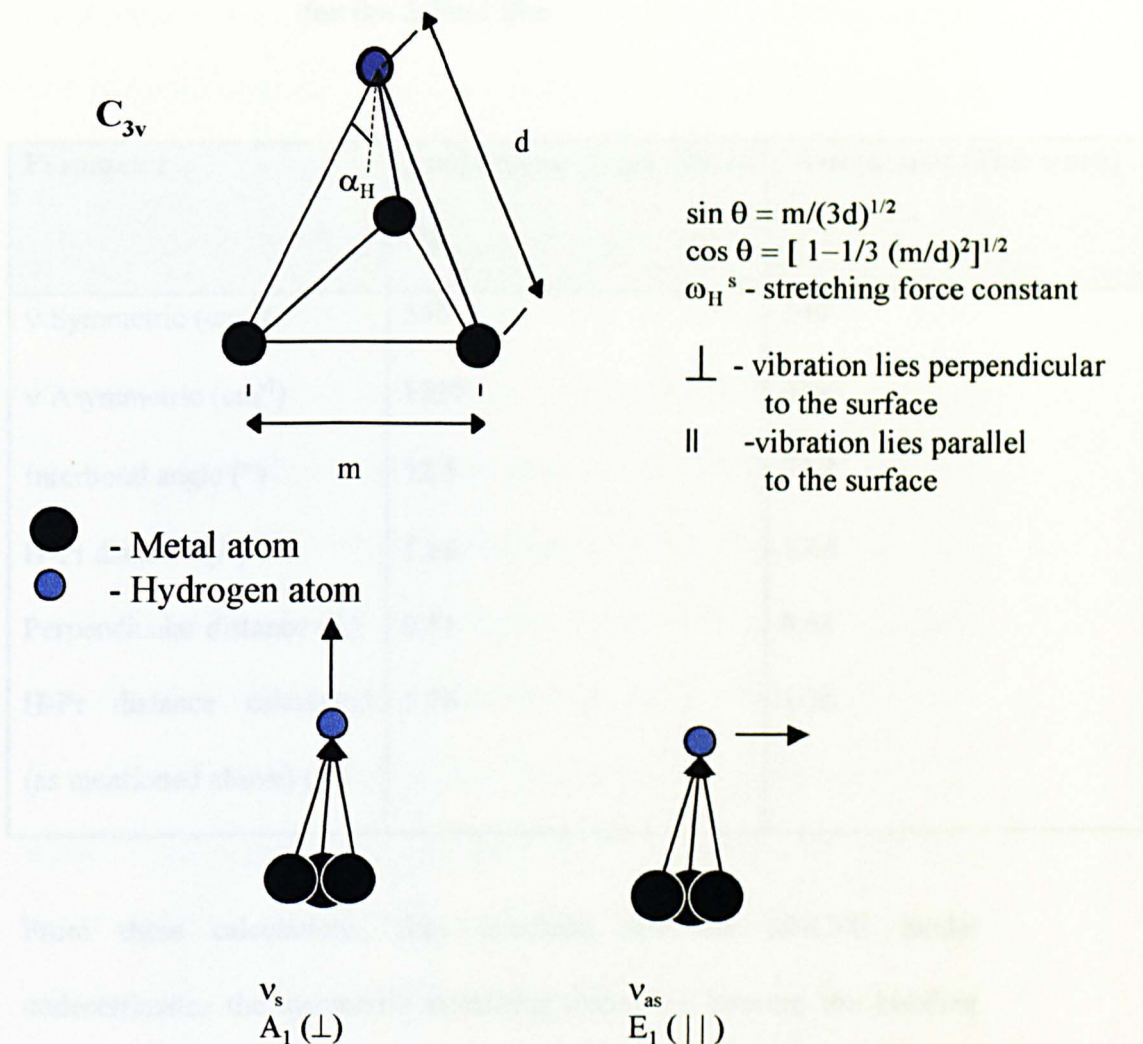
3. The metal substrate atoms are infinitely massive.

In fig.5.8 the expected vibrations for the three-fold site on the (111) surface are documented together with expressions deduced from the NNCFC model [2] for each site. All vibrations, perpendicular and parallel to the surface are given as both can be observed in impact scattering. From these vibrations an apex angle can be calculated and thus a H-Pt distance and a perpendicular distance of the hydrogen atom to the plane of platinum atoms. Table 5.2 shows the results of these calculations for this work and for that of Baro [3]. As the assignment is based on the NNCFC model, experiments have shown that the data obtained is comparable to that derived from cluster hydrides [14]. As this information is not readily available for Pt, it is compared with the sum of the metallic Pt radius (1.385 Å) and the atomic radius of hydrogen (0.37 Å) which is equal to 1.76 Å.

It can be seen that using the same interpretation for our results gives the same values reported by Baro [3] and this gives good agreement with the H-Pt value calculated from their respective radii. However the bands at 996 and 1749 cm^{-1} are not accounted for.

Richter [9] assigned the observed bands from a predicted dipole moment of the band at 903 cm^{-1} and the predictions from LAPW calculations from Feibelman [6] that the antisymmetric stretching frequency is higher than the symmetric stretching frequency. This model performs total energy calculations for (1x1) hydrogen adlayers on Pt (111) using a thin slab model for the metal surface.

Figure 5.8 Diagram Showing the Expected Vibrations from a 3-fold Bridging Site together with the Derivation of the Interbond Angle from the NNCFC Model



Vibration	Mode	Frequency
Symmetric stretch	$A_1 (\perp)$	$(3)^{1/2} \omega_H^s \cos \alpha_H^s$
Asymmetric stretch	$E ()$	$(3/2)^{1/2} \omega_H^s \sin \alpha_H^s$

$$\frac{(3/2)^{1/2} \omega_H^s \sin \alpha_H^s}{(3)^{1/2} \omega_H^s \cos \alpha_H^s} = 1/(2)^{1/2} \tan \alpha_H$$

$$\tan \alpha_H = \frac{(2)^{1/2} \text{ asymmetric stretching frequency}}{\text{symmetric stretching frequency}}$$

$\alpha_H = \text{Apex Angle}$

**Table 5.2 Interpretation of the Observed Bands Using the NNCFC Model
for the 3-Fold Site**

Parameter	Assignment from Baro [3]	Assignment [This work]
ν Symmetric (cm^{-1})	550	540
ν Asymmetric (cm^{-1})	1230	1185
Interbond angle ($^\circ$)	72.5	72.2
H-Pt distance (\AA)	1.68	1.68
Perpendicular distance (\AA)	0.51	0.51
H-Pt distance calculated (as mentioned above) (\AA)	1.76	1.76

From these calculations, they conclude that the NNCFC model underestimates the symmetric stretching frequency because the bonding involving the delocalised electrons of the substrate is largely non-directional, and that bending force constants are important. Therefore this leads to incorrect conclusions about the identity and geometry of the H-metal bond (for example they calculate a perpendicular distance of 0.95 \AA).

The assignment of the band at 540 cm^{-1} to the antisymmetric stretching frequency by Richter [9] is not convincing. They did not find dipole activity associated with the band at 540 cm^{-1} as Baro [3] did and the intensity of this peak is also weaker. They suggest that the dipole activity was due to H_2O contamination and that at low coverages the most

intense loss in EEL spectra is the Pt-OH₂ stretch at 544 cm⁻¹ [15]. The calculations of this band by LAPW have estimated it to be 919 cm⁻¹ and the antisymmetric stretches of known hydride compounds are higher in frequency, as in the case of Baro [3] where the antisymmetric is predicted to be higher than the symmetric frequency in order to calculate the H-Pt distance from the interbond angle. They assign the band at 1234 cm⁻¹ to an unresolved band of the overtone $\nu_{\text{asym}} 0 \rightarrow 2$ and a combination mode $\nu_{\text{asym}} + \nu_{\text{sym}}$. Neglecting anharmonicity these should occur at 1080 cm⁻¹ and 1443 cm⁻¹, neither of which is in good agreement with 1234 cm⁻¹.

Therefore because of the unsatisfactory assignments expressed above, an alternative assignment is considered, the two-fold site.

The NNCFC model has been successfully in its application to μ_2 -bridged metal hydrides to predict the M-H-M interbond angle and H-M bond length [4, 14]. One of the most extensively studied systems is the adsorption of hydrogen on the W(100) face [16].

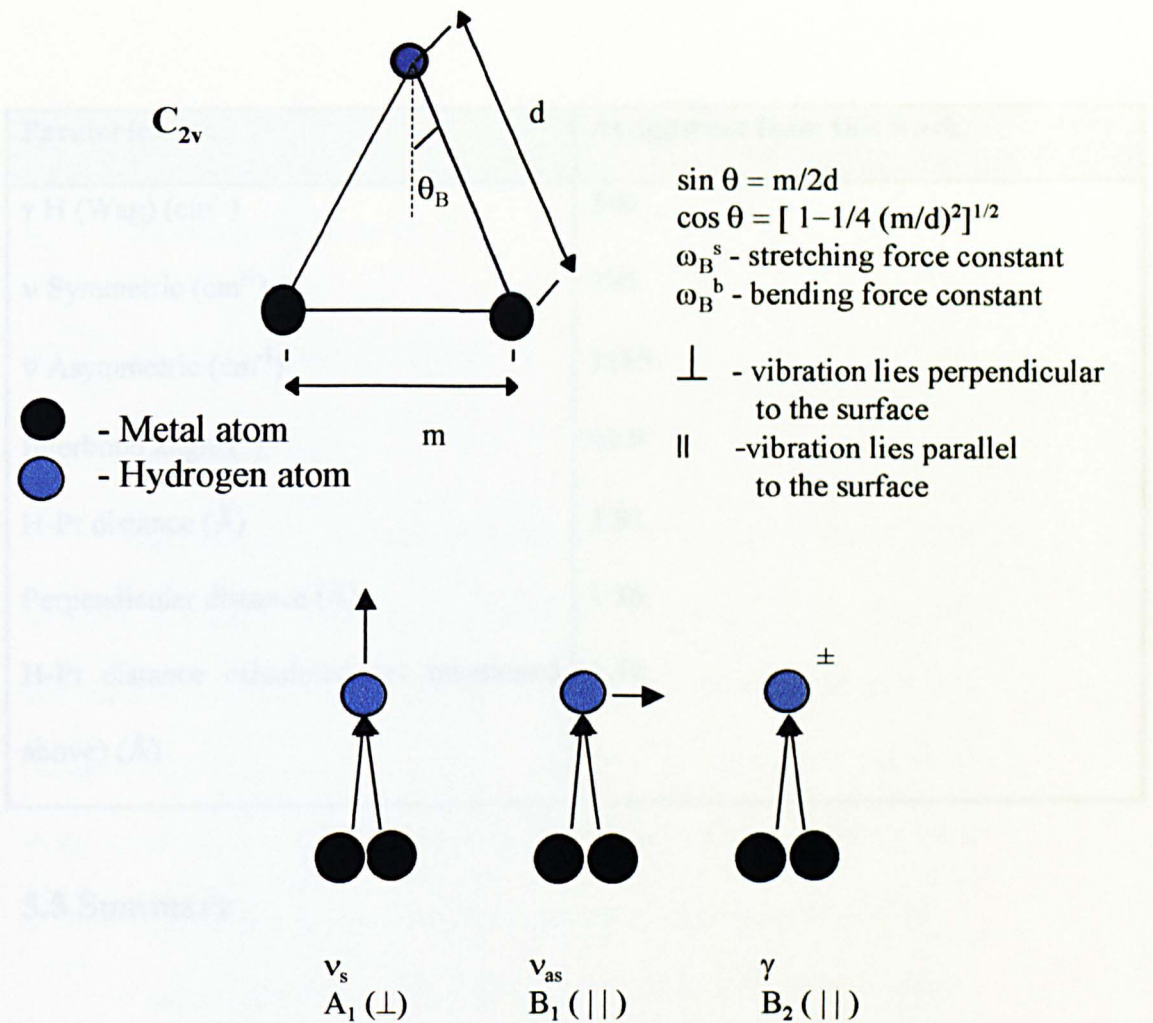
Ho *et al* [16] have reported the symmetric stretch at 1049 cm⁻¹ and the asymmetric stretch at 1291 cm⁻¹ for hydrogen in a μ_2 -bridging site. From cluster compound data a typical W-H distance of 1.9 Å is used to calculate a M-H-M bond angle of 112° (undistorted bridge, assuming pairs of atoms are separated by 3.16 Å). Using the simple model predicted by the NNCFC model and the symmetric and asymmetric stretching frequencies as above, an angle of 102° is predicted and a W-H bond length of 2.03 Å. Deviation is due to the neglect of an angle bending force

constant. In the same spectra a band at 645 cm^{-1} is assigned to the wag mode and a band at 2098 cm^{-1} to the overtone of the symmetric stretch.

In fig. 5.9 the expected vibrations for the two-fold site on the (111) surface are documented together with expressions deduced from the NNCFC model [2, 14] for each site. All vibrations, perpendicular and parallel to the surface are given as both can be observed in impact scattering. From these vibrations an interbond angle can be calculated and thus a H-Pt distance and a perpendicular distance of the hydrogen atom to the plane of platinum atoms. Table 5.3 shows the results of these calculations for this work. Again, as the assignment is based on the NNCFC model, experiments have shown that the data obtained is comparable to that derived from cluster hydrides [14]. As this information is not readily available for Pt, it is compared with the sum of the metallic Pt radius (1.385 \AA) and the atomic radius of hydrogen (0.37 \AA) which is equal to 1.76 \AA .

It can be seen that the 2-fold site gives good agreement with the bands observed. The band at 1749 cm^{-1} is assigned to the combination mode of the wag and the antisymmetric stretching frequencies.

Figure 5.9 Diagram Showing the Expected Vibrations from a 2-fold Bridging Site together with the Derivation of the Interbond Angle from the NNCFC Model



Vibration	Mode	Frequency
Symmetric stretch	$A_1 (\perp)$	$\omega_B^s \cos \theta_B$
Asymmetric stretch	$B_1 (\parallel)$	$\omega_B^s \sin \theta_B$
'Wag' - Bend	$B_2 (\parallel)$	$\omega_B^b < \omega_B^s$

$$\frac{\omega_B^s \sin \theta_B}{\omega_B^s \cos \theta_B} = \tan \theta_B = \frac{\text{asymmetric stretching frequency}}{\text{symmetric stretching frequency}}$$

$$\text{Interbond angle} = 2 \times \theta_B$$

Table 5.3 Interpretation of the Observed Bands using the NNCFC**Model for the 2-Fold Site**

Parameter	Assignment from this work
γ H (Wag) (cm^{-1})	540
ν Symmetric (cm^{-1})	996
ν Asymmetric (cm^{-1})	1185
Interbond angle ($^{\circ}$)	99.9
H-Pt distance (\AA)	1.81
Perpendicular distance (\AA)	1.16
H-Pt distance calculated (as mentioned above) (\AA)	1.76

5.5 Summary

Depending on the primary energy used in the experiment, the small amount of dipole contribution may be totally obscured by impact scattering. One experiment to increase the observation of the amount of dipole contribution uses the fact that dipole scattering is directly related to elastic peak intensity. At lower primary energies therefore dipole scattering predominates in the specular direction. At low primary energies the equation giving the ratio of impact to dipolar intensities is given by Eqn. 5.1 [17].

$$\frac{I_{\text{impact}}}{I_{\text{dipolar}}} \cong 10^{-4} |R_I|^{-2} \left(\frac{\hbar \omega_0}{e^*} \right)^2 \quad \text{Equation 5.1}$$

e^* - effective charge

R_I - crystal reflectivity given by $|R_I|^2 = \frac{I(\text{LEED}_{(0,0)} \text{ Beam})}{I(\text{incident})}$

$\hbar = \frac{h}{2\pi}$ where h is Plancks constant

ω_0 - loss frequency

Therefore if an energy is found where the $I(0,0)$ has a large intensity, the dipole scattering is maximized. Richter [9] found that this was the case at a primary energy of 6 eV. The spectra reported here of a better quality than those reported in reference [9]. Therefore the same study would have to be undertaken at 6 eV primary energy. In this way it is hoped that the dipole character of ν_{sym} may be indisputably confirmed.

Chabal [18] studied the RAIR spectrum of the Pt (111) - H system. A single hydrogen vibrational feature at 1254 cm^{-1} was observed. They state that the likely assignment is the symmetric stretching mode due to the strict surface dipole selection rules for RAIRS. This does not compare well with the EELS data. The band in this region of the spectrum has not exhibited the decrease in intensity expected for the off-specular spectrum for a mode that possesses a perpendicular dipole moment and none of the authors have attributed this band to the symmetric stretching mode.

Primet *et al* have observed a weakly bound state of hydrogen on Pt/Al₂O₃ and on Pt/MgO [19, 20]. A single IR peak (2120 cm^{-1}), that does

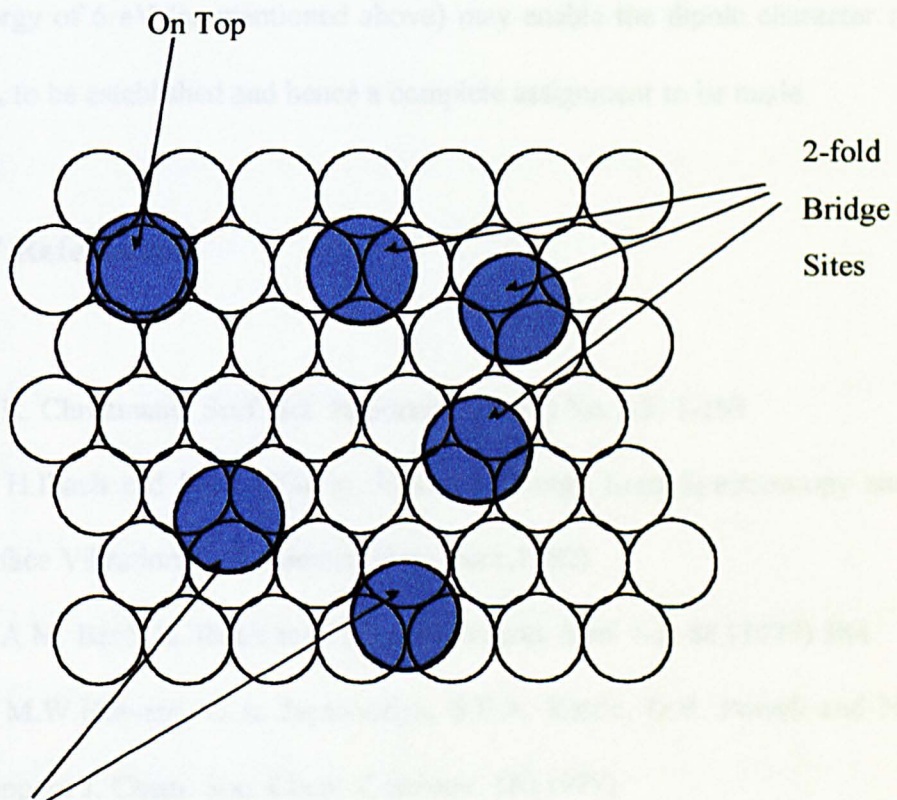
not shift in position but grows in intensity with increasing pressure of hydrogen above 0.1 Torr was observed. It has been attributed to hydrogen bound linearly to the Pt in an on-top position. This is shown in fig. 5.10 together with the 2-fold and 3-fold sites. This has yet to be observed in EELS, but the high pressures associated with this state (> 0.1 Torr) may mean that it is not applicable to electron spectroscopy. One method of trying to achieve this state would be to pre-dissociate the hydrogen on a hot tungsten filament. This experiment has yet to be tried.

In the low coverage experiments, a peak was observed at 285 cm^{-1} . It can not be assigned to a hydrogen mode as all the modes have been accounted for and the frequency is too low. It was at first thought to be due to a metal phonon on the hydrogen covered surface. Michely *et al* [21] have reported that the electronic structure of Pt (111) after hydrogen adsorption is more similar to the bulk electronic structure than that of the clean structure. The band reported here is above the top of this phonon band (*ca.* 194 cm^{-1}). Therefore the nature of this band remains unsolved.

5.6 Conclusions

The data achieved has been analysed in terms of a 3-fold and a 2-fold bridging site using the NNCF model. From simple geometric considerations based on the assignment of the symmetric and antisymmetric stretches the 2-fold site offers the more complete interpretation of the bands observed. This is in conflict with the assignment

Figure 5.10 A Schematic Diagram Showing some of the possible Occupied Sites on a (111) Surface



3-fold Hollow Sites
(FCC and HCP)

from previous experimental EELS and theoretical (LAPW calculations) work. Evidence from He scattering [7] and INS [8] also suggest a 3-fold site on the (111) surface, and there is general agreement that hydrogen adsorbs in the three-fold site on (111) surfaces of the face centered cubic group VIII metals. However, the EEL and IR spectra of the adsorption of hydrogen on Cu (111) has also indicated that the adsorbate sits at two-fold bridging sites [22]. A study of the Pt (111)-H system using a primary energy of 6 eV (as mentioned above) may enable the dipole character of ν_{sym} to be established and hence a complete assignment to be made.

5.7 References

- [1] K. Christmann, Surf. Sci. Reports 9, (1988) No.1-3, 1-163
- [2] H.Ibach and D.L. Mills in 'Electron Energy Loss Spectroscopy and Surface Vibrations', (Academic, New York,1982)
- [3] A.M. Baró, H. Ibach and H.D. Bruchmann, Surf. Sci. 88 (1979) 384
- [4] M.W.Howard, U.A. Jayasooriya, S.F.A. Kettle, D.B. Powell and N. Sheppard J. Chem. Soc. Chem. Commun. 18 (1979)
- [5] K. Christmann, G. Ertl and T. Pignet, Surf. Sci. 54 (1976) 365
- [6] P.J. Feibelman and D.R. Hamann, Surf. Sci. 182 (1987) 411 and references within
- [7] J. Lee, J.P. Cowin and L. Wharton Surf. Sci. 130 (1983) 1
- [8] D. Graham, J. Howard and T.C. Waddington J. Chem. Soc. Faraday trans. I 79 (1983) 1281

- [9] L.J. Richter and W. Ho, Phys. Rev. B 36 (1987) 9797
- [10] J.J. Rush, R.R. Cavanagh and R.D Kelley, J. Vac. Sci. Technol. A1 1245 (1983)
- [11] B. Poelsema, L.S Brown, K. Lenz, L.K. Verheij and G. Comsa, Surf. Sci., 171 (1986) L395
- [12] H. Conrad, R. Scala, W. Stenzel and R. Unwin, J. Chem. Phys. 81 (1984) 6371
- [13] H. Conrad, M.E. Kordesch, R. Scala and W. Stenzel, J. Electron Spectrosc. Relat. Phenom. 38 (1986) 289
- [14] U.A. Jayasooriya, M.A. Chesters, M.W.Howard, S.F.A. Kettle, D.B. Powell and N. Sheppard, Surf. Sci. 93 (1980) 526-534
- [15] B.A Sexton, Surf. Sci. 94 (1980) 435
- [16] W. Ho, R.F. Willis and E.W. Plummer, Phys. Rev. Letts. 40 (1978) 1463
- [17] E.M. McCash PhD Thesis UEA 1986
- [18] J.E. Reutt, Y.J. Chabal and S.B. Christman, J. Vac. Sci. Tecnol. A6 (3) (1988) 816
- [19] M. Primet, J.M. Basset and M.V. Mathieu, J.C.S. Faraday I, 70 (1974) 293
- [20] J.P. Candy, P. Fouilloux and M. Primet, Surf. Sci., 72 (1978) 167
- [21] T. Michely and G. Comsa, Phys. Rev. B, 44 (1991) 8411-8414
- [22] E.M. McCash, S.F. Parker, J. Pritchard and M.A. Chesters, Surf. Sci., 215 (1989) 363-377